Global Mode Analysis of Centrifugal and Curvature Driven Interchange Instabilities

Benjamin Joseph Levitt

SUBMITTED IN PARTIAL FULFILLMENT OF THE

REQUIREMENTS FOR THE DEGREE

OF DOCTOR OF PHILOSOPHY

IN THE GRADUATE SCHOOL OF ARTS AND SCIENCES

Columbia University

2004

ABSTRACT

Global Mode Analysis of Centrifugal and Curvature Driven Interchange Modes

Benjamin Joseph Levitt

The first study of the global mode structures of interchange modes driven by both pressure and centrifugal forces created in a laboratory magnetic dipole is presented. The mode structures are determined using a correlation analysis of movable high-impedance floating potential probes located at various positions within the plasma. These structures are reproduced by a fully self-consistent nonlinear particle simulation of interchange instabilities in dipole geometry.

Hot electron interchange (HEI) instabilities are driven by a population of energetic, deeply trapped particles with a steep outward pressure profile produced by electron cyclotron resonance (ECR) heating. The mode structures are determined primarily by low azimuthal mode number and boundary conditions and are broad in radial extent.

The centrifugally-driven interchanges are excited by the creation of radial electric fields which cause bulk azimuthal plasma $\mathbf{E} \times \mathbf{B}$ rotation. Electric fields are created using an equatorial hot-filament bias control system which alters the plasma's equilibrium electrostatic potential by biasing inner flux tubes with respect to the outer chamber wall. The mode structures for these instabilities are dominated by low azimuthal mode numbers and broad radial structures. These measurements constitute the first experimental observation of the centrifugal interchange instability.

Acknowledgments

I would like to thank my thesis adviser, Dr. Michael Mauel, for providing me with such a fascinating and stimulating project as well as the skill necessary to tackle it. He has taught and inspired me with his infectious enthusiasm and deep understanding. Dmitry Maslovsky has also been a source of invaluable knowledge and insight into my research, and deserves many thanks.

The Department of Applied Physics has provided a wonderful environment which has been a home these past years. I will sorely miss it and hope to return to visit those that made my stay here so special. In particular I would like to thank Marlene Arbo and Lydia Argote for the friendly environment they create as well as the invaluable support structure, both administrative and personal, they provide.

I also thank my father, Martin, and sisters Emily and Jennifer, for their endless support and patience, and my dear friends for having faith all along the way. I dedicate this work to my dear mother, Marilyn, may she rest in peace. I wish she were here to appreciate this milestone in my life.

Contents

List of Figures

List of Tables

Chapter 1

Introduction

Interchange, or "fluting", instabilities in magnetized plasmas are among the best known in plasma physics. [39, 5, 6, 60] Interchange motion mixes plasma contained by magnetic flux tubes while minimizing changes in the magnetic field. Instability results when this mixing reduces the plasma's potential or kinetic energy. This occurs for various reasons in the laboratory, the ionosphere, and in planetary magnetospheres. In laboratory plasmas, interchange instabilities are possible when the pressure gradient has components parallel to the magnetic curvature. Experiments have shown them to be stabilized by reversing the direction of curvature,[28, 24] by creating "average good curvature" either on toroidal flux surfaces[18] or on the plasma-vacuum boundary,[16] and by creating local regions with average magnetic shear.[35] In the ionosphere, gravity drives interchange instability, and its nonlinear evolution plays an essential role in the intense wave dynamics of the night-time equatorial F-region.[30] Interchange motion of plasma confined by the dipole-like field of planetary magnetospheres can be driven or "spontaneous" (*i.e.* unstable), and both have been extensively studied theoretically.[20, 62, 63] Because the magnetic field strength of a dipole decreases rapidly with radius, $B \sim R^{-3}$, interchange motion in a dipole is associated with significant plasma compression. Pressure gradients can drive interchange instability in a dipole only when the equatorial plasma pressure profile varies more rapidly than $p \sim R^{-4\gamma}$ (where $\gamma \approx 5/3$ is the appropriate magnetohydrodynamic (MHD) ratio of specific heat). Observations show the Earth's magnetosphere to be interchange stable, but steady plasma circulation and impulsive radial-diffusion[12] results from electric fields created

by the solar wind, and these can be considered examples of driven interchange motion. In Jupiter's magnetosphere, interchange instability is influenced by pressure gradients and by centrifugal forces caused by co-rotation.[61] Recently, the Galileo spacecraft measured a buoyant, inward-moving flux tube within Jupiter's Io plasma torus and also fluctuations in the bulk ion flow and density that provide evidence for unstable interchange motion of dipole-confined plasma in space.[65, 33, 17]

Although interchange instability is an important process for magnetized plasma, measurement of its global structure has been possible in only a few cases. Probably, the most detailed images of interchange instability have been made from radio-wave scattering from the F-layer of the ionosphere. (See Kelly's monograph.[30]) These spectacular images show towering "plumes" created by rising interchange "bubbles". Nonlinear simulation of the gravitational interchange has reproduced this plume structure.[74] Laboratory observations of the nonlinear structures of interchange instability have also been made using toroidal devices that have regions without magnetic shear. The electrostatic potential has been mapped using movable floating potential probes in a toroidal octupole[35, 49] and in current-free discharges created in a purely toroidal magnetic field.[52, 54] These electrostatic potential structures sometimes form closed equipotential contours that appear as slowly propagating and coherent $\mathbf{E} \times \mathbf{B}$ vortices, or "convective cells". They decay by viscous forces if not continuously driven. For plasma formed within a purely toroidal magnetic field, the electrostatic potential evolves into a highly nonlinear state dominated by a rotating dipole vortex superimposed on equilibrium poloidal flows that have been reproduced by self-consistent, nonlinear simulation.[58]

When interchange instabilities are excited by magnetically-trapped energetic electrons, the modes have a real frequency proportional to the fast ∇B drift of the hot electrons, ω_d. When the rotation frequency is less than the ion-cyclotron frequency, the instability is called the low-frequency hot electron interchange (HEI) instability.[34] Higher frequency modes have been described by Berk,[3] and both the low-frequency and high-frequency hot electron interchange mode have been identified experimentally.[2, 25, 37] Hot electron plasmas can remain stable even when pressure gradients exceed the usual MHD condition for flute instability because the real frequency of the mode generates stabilizing ion polarization currents. Although the global mode structure was not measured directly in these previous studies,

Spong and co-workers[64] showed that when realistic profiles are used during computation of the linear, radial eigenmode, then the predicted onset for instability was consistent with experimental observations. The first global mode structure measurements of the low frequency HEI instability were presented by Levitt et al [36] and are described in more detail in this thesis.

As mentioned, interchanges may also be driven by centrifugal forces. The possibility of centrifugally driven plasma convection has been studied in the Io plasma torus of Jupiter. With an 11 hour day and a largely co-rotating high β magnetosphere, rapid Jovian rotation produces an outwardly directed effective gravity. As described by Siscoe and co-workers [61], the outer edge of the Io plasma torus is likely unstable to rotationally-driven interchange instabilities. During the Galileo spacecraft's encounter with Io in December 1995, several wave phenomena were observed by the magnetometer instrument [32, 57]. Measurements of the radial profile of phase space density of energetic S^+ ions in the torus found an anomalous enhancement of phase space density at an inner location ($L = 6.03$) that corresponded to values native to the outer torus ($L \approx 6.3$) [46]. This has been interpreted as an inward moving plasma "bubble" caused by rotationally driven interchange motion. However, rotationally driven interchanges have not been observed experimentally to date. Such observations are also included in this thesis, along with the measured mode structures of the rotational instabilities and a comparison to the same non-linear simulation mentioned previously. Thus, this thesis constitutes observations and global descriptions of interchange modes driven by both pressure and centrifugal forces.

1.1 Experimental Observations

Within this thesis are presented the first measurements of the mode structure of the electrostatic, low-frequency interchange instability driven by energetic electrons trapped in an axisymmetric dipole magnetic field. The modes rotate rapidly in the drift direction of the trapped electrons, and they have a complex and time-varying frequency spectrum. Several modes co-exist. Experimentally, these modes are distinguished from each other using frequency-domain correlation between several movable probes and a fixed reference probe. The measurements show the flute-modes have a radial structure that depends only on the

azimuthal mode number, m, extends across the entire dipole-confined plasma, and does not evolve in time with the frequency. In this article, we also compare these measurements to a fully self-consistent, nonlinear simulation that has been described elsewhere.[44] This simulation reproduces both the large-amplitude mode structure of the interchange modes and their complex, time-varying frequency spectra.

We also present for the first time the observation of the rotationally driven interchange mode. Plasma is rotated to near sonic flows by imposing an external radial electric field with a tungsten electrode array, which causes an azimuthal $\mathbf{E} \times \mathbf{B}$ bulk plasma rotation. The resulting centrifugal force on the massive ions results in charge separation and instability drive. The observed instabilities are coherent modes with global radial mode structure and low azimuthal mode numbers. The frequency of the $m = 1$ mode in the lab frame is approximately 25 kHz, roughly equal to the $\mathbf{E} \times \mathbf{B}$ frequency of the plasma plus a smaller contribution from the drift resonant hot electrons. The ion density profile is seen to flatten in the presence of the instability. Results from the self-consistent non-linear particle simulation are compared to observations and reproduce key characteristics including the global mode structure from the experimental results.

1.2 Numerical Simulations

Observations of both the HEI and rotational interchange instability are compared to a self-consistent non-linear numerical simulation. Originally written to study the growth and saturation of the HEI mode, it reproduces both the global mode structure [36] and the frequency sweeping and phase-space structure formation of the HEI instability observed experimentally [42]. The radial and azimuthal mode structure is reproduced upon appropriate adjustment of the boundary conditions.

The same code produces the rotational mode by adjusting the hot electron and ion profiles and introducing rigid rotation due to either or both of gravitational and centrifugal forces. Short wavelength damping must also be adjusted for good agreement. Typically, the hot electron fraction is reduced from the HEI runs, while the ion profile is steepened, which, in combination with rotation, produces dramatic ion mixing. As with the HEI investigations, experimental mode structures are reproduced through adjustment of boundary conditions.

1.3 Organization

This thesis is organized according to the following manner. In Chapter 2 we introduce the basic physical concepts of dipole geometry and interchange instabilities. The Collisionless Terrella Experiment (CTX) and its diagnostics are described in Chapter 3. Chapter 4 covers the pressure driven HEI instabilities and the global mode structure analysis performed with a multi-probe cross-correlation method. These results are also compared to results from the non-linear particle simulation. Experimental excitation and observation of the rotationally driven interchange mode using the external bias array is described in Chapter 5. Here, we also give the results of the same global mode structure performed on the HEI mode for these rotational instabilities. Again, results are compared to simulation. In Chapter 6, the interchange instability dispersion relation driven by both pressure and centrifugal forces is derived using a non-linear two-fluid analysis in dipole flux co-ordinates. The resulting dispersion relation is used to interpret the experimental observations of the rotational mode. A summary of results is given in Chapter 7.

All mathematical formulas are presented in Gaussian (cgs) units, unless noted otherwise.

Chapter 2

Dipole and Interchange Physics

In this chapter we discuss the basic concepts of interchange instabilities, starting with the well-known Rayleigh-Taylor instability, and progressing to fluid interchanges driven by various forces, such as gravity, centrifugal, magnetic gradient and curvature forces as well as finite-temperature kinetic instabilities, such as the Hot Electron Interchange (HEI) instability, observed in the CTX device.

In addition, some basic concepts of plasma confinement in a magnetic dipole will be introduced, including adiabatic invariants and dipole flux co-ordinates, which will be used frequently throughout.

2.1 Interchange Instabilities

Interchange instabilities are probably the simplest and most important type of plasma instability. The well-known hydrodynamic version of an interchange is the Rayleigh-Taylor instability, in which a heavy fluid is supported against gravity by a light fluid. This equilibrium is unstable to small perturbations, so that the interface between the fluids becomes rippled, and the two fluids begin to mix (or interchange) and the heavy fluid falls through the light fluid. Figure 2.1 shows sequential sketches from photos of the hydrodynamic Rayleigh-Taylor instability [30]. The plasma analog of this situation is a plasma supported against gravity by a vacuum magnetic field. The planar, or slab, geometry of this unstable equilibrium is shown in Figure 2.2. We've introduced the situation using gravity, but we can

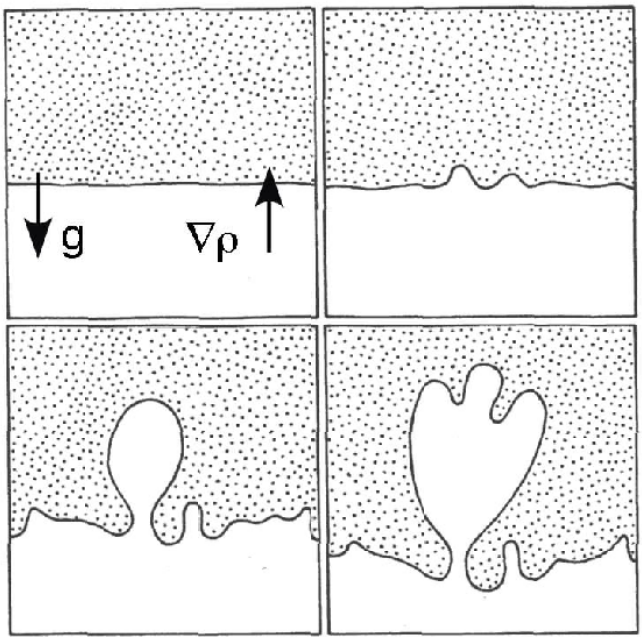

Figure 2.1: The gravitational Rayleigh-Taylor instability [Kelly (1989)].

substitute in the $\nabla\mathbf{B}$ force as well. Gravity is rarely of much importance in laboratory plasmas, so the real importance of the Rayleigh-Taylor instability is the close analogy it bears with the magnetic gradient and curvature forces that come into play when plasmas are confined by curved magnetic fields.

The figure shows a plasma supported against a downward force by a magnetic field out of the page. A perturbation at the surface causes charge separation via the plasma drifts which correspond to whichever force is at play. For a given force the plasma drift is, from the Lorentz force equation,

$$\mathbf{u} = \frac{1}{q}\frac{\mathbf{F}\times\mathbf{B}}{B^2}, \tag{2.1}$$

so that the gravitational drift is

$$\mathbf{u}_g = \frac{m}{q}\frac{\mathbf{g}\times\mathbf{B}}{B^2}, \tag{2.2}$$

and the $\nabla\mathbf{B}$ drift, whose force is $\mathbf{F}_{\nabla\mathbf{B}} = -\mu\nabla\mathbf{B} = -(mv_\perp^2/2B)\nabla\mathbf{B}$, where μ is the magnetic moment of a particle of mass m and charge q, is

$$\mathbf{u}_{\nabla\mathbf{B}} = \frac{\mu}{q}\frac{\mathbf{B}\times\nabla\mathbf{B}}{B^2}. \tag{2.3}$$

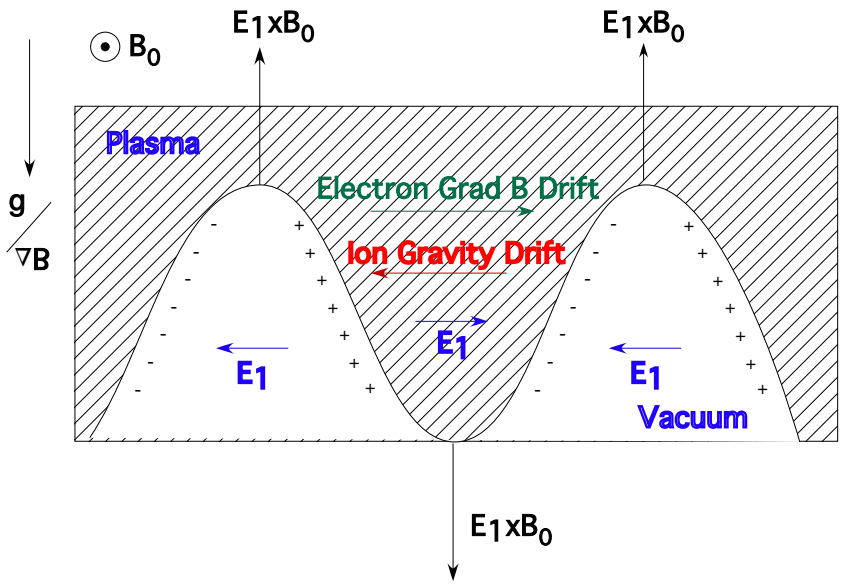

Figure 2.2: The interchange instability drive mechanism.

We note that both drifts are charge dependent, so that ions and electrons drift in opposite directions, creating charge separation and buildup on the plasma boundary, and electric fields which can drive instabilities. The gravitational drift is also mass dependent, so that electrons have a negligible drift compared to ions. The $\nabla \mathbf{B}$ drift, on the other hand, is independent of mass for a fixed energy, though electrons usually have higher energy due to their lesser inertia.

The ensuing drifts and electric fields are shown in Figure 2.2. The resulting fields, the $\mathbf{E}_1$'s, end up in the same direction for both forces, which cause a secondary drift from the electric force, the $\mathbf{E} \times \mathbf{B}$ drift,

$$\mathbf{u}_e = \frac{\mathbf{E} \times \mathbf{B}}{B^2}, \tag{2.4}$$

which is in the same direction as the original perturbation, thereby providing positive feedback for unstable motion.

A simple global normal mode analysis - which we will perform in full detail in dipole flux co-ordinates in Chapter 6 - results in the following slab geometry growth rate for the most

unstable interchange modes,

$$\gamma = (g/s)^{1/2}, \tag{2.5}$$

where s is the plasma density scale length. Thus, the steeper the gradient in density, the faster interchange motion sets in to flatten the gradient. The stability condition in the slab geometry is simply

$$\mathbf{g} \cdot \nabla\rho > 0, \tag{2.6}$$

where ρ is plasma density. That is, a density gradient opposing gravity results in instability.

Interchanges due to Field Curvature For the case of curved magnetic fields, we can borrow the results from the gravity case by making a few substitutions. Particles, in general, travel along field lines, so in a curved magnetic field, particles will experience a centrifugal force. If the radius of curvature of the field is $\mathbf{R}_c$, the centrifugal force on the particle is,

$$\mathbf{F}_{cf} = \frac{mv_\parallel^2}{R_c}\hat{\mathbf{r}}, \tag{2.7}$$

where $v_\parallel$ is the velocity along the field-line, with the resulting curvature drift given by

$$\mathbf{u}_{curv} = \frac{mv_\parallel^2}{qB^2}\frac{\mathbf{R}_c \times \mathbf{B}}{B^2}. \tag{2.8}$$

It is often helpful to combine the magnetic curvature and gradient drifts into a single expression, since a realistic magnetic field is characterized by both these attributes. For a zero-curl magnetic field - which is a field with no volume currents, a so-called vacuum field - the combined drift has a simple form [21]:

$$\mathbf{u}_B = \frac{m}{q}(v_\parallel^2 + v_\perp^2/2)\frac{\mathbf{R}_c \times \mathbf{B}}{R_c^2 B^2}. \tag{2.9}$$

Comparing this expression with the gravitational drift, Equation 2.2, shows that, provided gravity and the radius of curvature are aligned, we can adopt results from the gravitational case by substituting the appropriate expression for g. We average the velocities in Equation 2.9 over a thermal distribution and relate them to the temperature, and hence to the pressure and density. The proper substitution is $g = 2p/\rho R_c$. The comparable slab geometry stability criterion for pressure driven interchanges becomes

$$\mathbf{R}_c \cdot \nabla p > 0. \tag{2.10}$$

Thus instability arises when a plasma is confined by a curved magnetic field which is concave toward the plasma. In the fusion community this is often referred to as "bad curvature", and it has profound influences on design and operation of various fusion confinement devices. Figure 2.3, for instance, shows a plasma configuration commonly referred to as a "magnetic mirror", which possesses bad curvature. The magnetic field is axial, produced by the blue current-carrying coils, and increases in magnitude at either end of the mirror so as to axially confine the plasma. This configuration has an outwardly directed radius of curvature at the ends, where the field increases. The plasma is peaked on axis, and therefore has an inwardly directed pressure gradient. Thus, by the arguments we have just lain out, the configuration becomes unstable. Ripples at its surface grow larger in time.

The ripples are constant along field-lines because interchange motions do not bend magnetic field-lines. They do not, in general, alter magnetic field energy density, in contrast with other types of plasma instabilities seen in toroidal magnetic traps. Instead they release thermal energy from adiabatic expansion of plasmas across magnetic fields. If we consider the linear wave properties of interchange fluctuations it is true that

$$\mathbf{k} \cdot \mathbf{B} = 0, \tag{2.11}$$

or $k_{\|} = 0$, where $\mathbf{k}$ is the wave-vector of the instability. These instabilities are also called "flute" instabilities.

2.1.1 Interchange Instability in a Magnetic Dipole

Gravity and Rotation Driven Interchanges

Magnetic dipoles are another configuration that confine plasma with bad magnetic curvature. Dipole confined plasmas are found naturally in planetary magnetospheres, accretion disks and many other astrophysical environments. An important aspect of the dipole magnetic field is that the rapid radial variation of its field strength ($1/r^3$) leads to strong compressibility effects for the interchange mode [5, 31]. Strong pressure and density gradients may still be stable provided these gradients do not exceed thresholds set by the compressibility criterion. Long-lived equilibria exist such as Earth's radiation belts or Jupiter's Io torus. Such a configuration is depicted in Figure 2.4

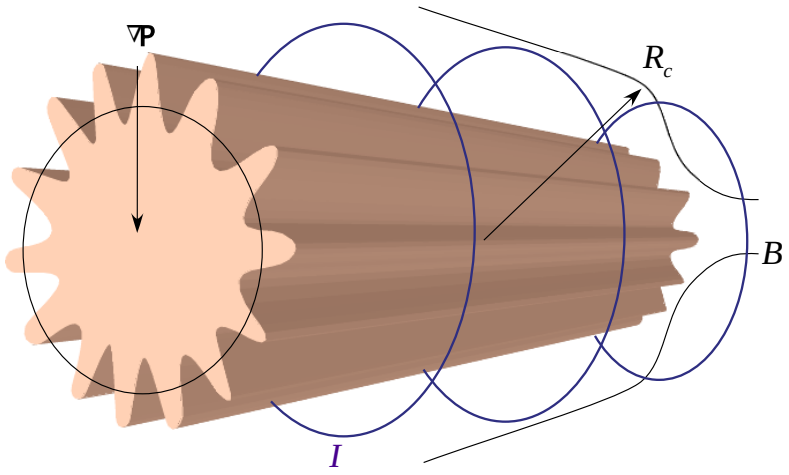

Figure 2.3: *Magnetic mirror* configuration, which possesses bad curvature.

Dipole magnetic field-lines are shown, as well as two flux tubes containing plasma, one at r_1 and one at r_2. A high pressure, deeply confined torus is also shown. The planet, as well as the magnetic field, spins at angular frequency Ω, and - in the so-called frozen-in field condition - so is the plasma. This condition of plasma spinning at the same angular frequency as the planetary magnetic field is called co-rotation, and is not always strictly true. In Earth's magnetosphere, for instance, co-rotation extends out to the plasmapause, beyond which the plasma flow circulation is driven by the solar-wind. In the Jovian magnetosphere the radius within which the plasma co-rotates with the planet extends much further due to its very strong magnetic field and the relatively weaker solar-wind flows.

The rotation of the plasma causes an outwardly directed centrifugal force on the plasma, given by,

$$\mathbf{F_{cf}} = -\rho\mathbf{\Omega} \times (\mathbf{\Omega} \times \mathbf{r}). \tag{2.12}$$

It is common practice to incorporate this force into an effective gravity, $\mathbf{g}_{eff} = \mathbf{g} - \mathbf{\Omega} \times (\mathbf{\Omega} \times \mathbf{r})$, in the plasma frame of reference. Such a substitution leaves the general equations used to derive the growth rates and stability criterion for the gravitational interchange instability

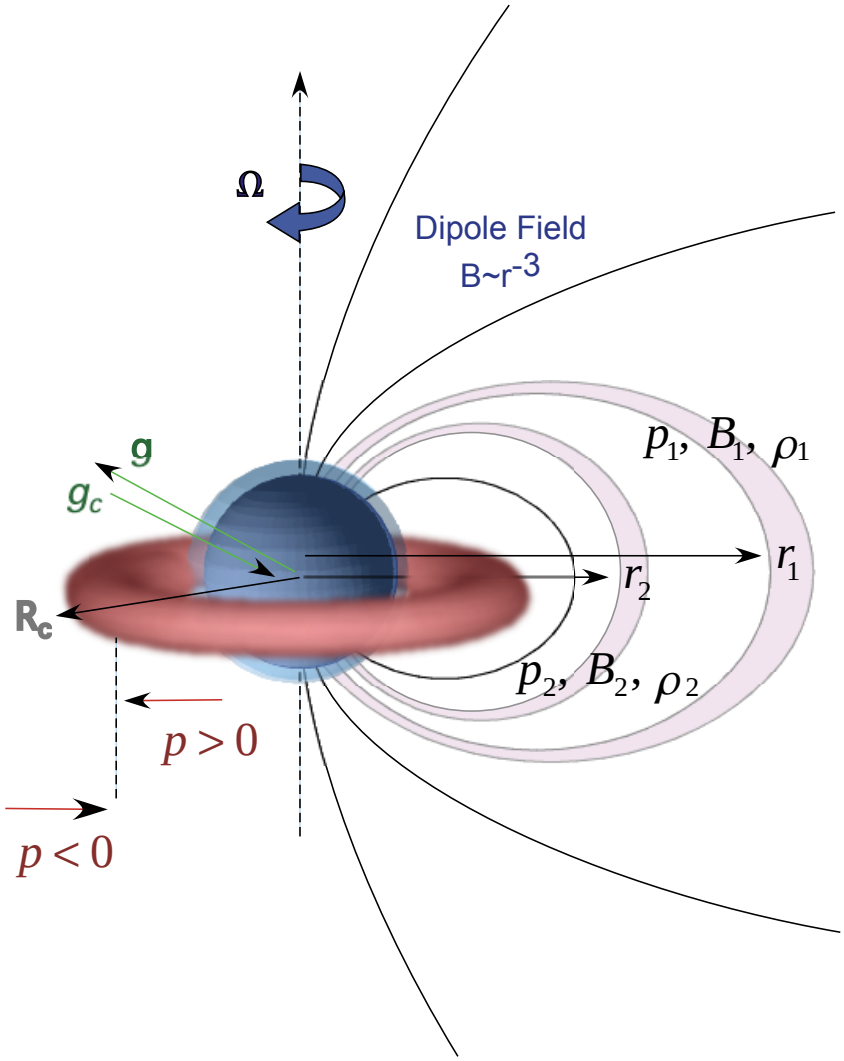

Figure 2.4: A schematic of a dipole confined plasma, specifically, a planetary magnetosphere.

unchanged, and therefore it is clear that centrifugal forces as well may cause interchange instabilities in rapidly rotating plasmas.

Since gravity goes as r^{-2} and the centrifugal force goes as r, close to the planet gravity may be dominant, while further out the centrifugal force becomes stronger [62]. For example, in Figure 2.4, close to the planet where the density gradient is outward, there is a region which is unstable to gravitationally driven interchanges. On the other hand, further out, where the density gradient is inward and where the centrifugal term dominates $\mathbf{g}_{eff}$, the plasma supports centrifugally driven interchange motion. That is, in the former region $g_{eff}\partial\rho/\partial\psi < 0$ is true, while in the latter $g_{eff}\partial\rho/\partial\psi > 0$ holds, where ψ is the magnetic flux and is inversely proportional to radius. Dipole flux co-ordinates will be discussed in the next section.

Observation of the gravitational mode occurs regularly, primarily in the evening, in the F-layer of the ionosphere [30]. Plume-like structures, or bubbles of upwelling plasma are interpreted as resulting from a convective instability driven by gravitational forces. These instabilities are called Equatorial Spread F (ESF). Little evidence exists, on the other hand, regarding observation of the centrifugally driven mode. As mentioned in Chapter 1, the possibility of centrifugally driven plasma convection has been studied in the Io plasma torus of Jupiter. In addition to the 1995 Galileo observations, much theoretical and numerical work has also been devoted to this problem (see [13, 14, 15, 38, 63, 62, 55, 7, 56, 50, 6, 20] for a history of the subject all the way back to Gold, who first proposed the possible existence of this class of motions in the Earth's magnetosphere). One example of a numerical simulation of torus-driven plasma transport is shown in Figure 2.5 [73]. Further observation of this phenomenon may come with the upcoming Cassini encounter with Saturn. However, none of these suggestive measurements have been supported by direct experimental observation of the centrifugal mode. The experiments that are described in this thesis constitute the first direct evidence of this instability.

Pressure Driven Interchanges

If a dipole confined plasma has a thermal component, the plasma pressure will be nonzero, and will thus introduce the possibility of becoming unstable to flute instabilities, *ie.*, having

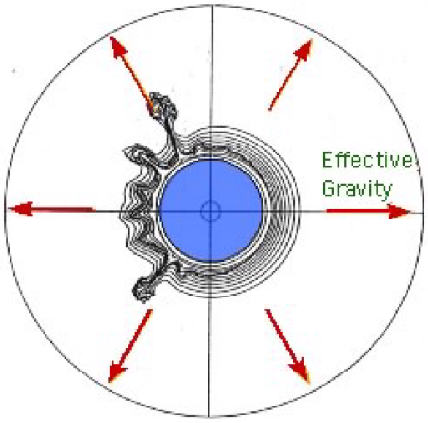

Figure 2.5: Computed cold plasma edges in the equatorial plane, showing so-called *fingers* of torus-driven plasma transport [Yang et al (1994)].

bad curvature. Returning to Figure 2.4, the pressure gradients associated with the thermal plasma torus are shown and indicate the stability regions that result: since the radius of curvature is outwardly directed, the plasma is stable to interchanges on the inside of the torus, while being unstable on the outside. This is the same region which is unstable to centrifugally driven modes. Thus interchanges driven by a combination of centrifugal and pressures drives are possible. A local nonlinear stability analysis of these modes is described in Chapter 6.

When we speak of interchange motion it is convenient to describe the motion of two flux tubes of plasma, as in Figure 2.4, which contain equal magnetic flux, $\Phi = A \cdot B$, where A is simply the area of the given flux tube, and B is the field at the location. If such were not the case, then the magnetic topology would necessarily be changed, which usually causes an increase in the total magnetic field energy. Other classes of motions called quasi-interchanges allow for small nonzero $k_{\|}$ and may be important in magnetospheres [13, 14, 15, 50] From this condition one can derive via a simple argument first given by Gold [20] what the marginally stable pressure profile is to interchanges. Given that the dipole field goes as r^{-3}, the constant flux condition for two flux tubes, 1 and 2, is $A_1 r_1^3 = A_2 r_2^3$. The area of an outward moving flux-tube, call it flux-tube 1, increases by $(r_2/r_1)^3$, while the volume increases by $(r_2/r_1)^4$, since the length of the flux-tube is proportional to r. For adiabatic expansion, we have $pV^{5/3} = constant$. Since $V \propto r^4$, we have $pr^{20/3} = constant$. And so, the pressure profile

that corresponds to this adiabatic motion in a magnetic dipole is $p \propto r^{-20/3}$. Any profile less steep than this is supportable by the magnetic field in spite of the bad curvature. Instabilities, then, can be controlled if one has control of the pressure profile.

Such pressure driven instabilities are commonly seen in experimental situations and have been the subject of research on the CTX device [72, 68, 69, 70, 44, 42, 36, 45, 41, 40].

Hot Electron Interchange Instability

The particular type of flute instability observed in the Collisionless Terrella Experiment is called the Hot Electron Interchange (HEI) Instability, first descibed by Krall [34]. It is distinct from a standard MHD flute instability in that the instability is driven entirely by electron pressure with cold neutralizing ions. Additionally, since the hot electrons have a distribution of energy there is a drift resonant interaction between the energetic particles that comprise the non-Maxwellian part of the distribution function and the azimuthally propagating instability that exists within the plasma. This instability is analogous to the so-called bump on tail instability. Physically speaking, when the wave and the particle have roughly equal velocities, $\omega \sim kv$ (where ω is the frequency of the wave, k is the wave number and v is the particle thermal velocity), resonant wave-particle interactions lead to energy exchange with the waves electrostatic potential. If the particle distribution, F, is characterized by more fast particles than slow ones near $v \sim \omega/k$, then $\partial F/\partial v|_{v=\omega/k} > 0$ will be true, and the wave will take energy from the particle, resulting in wave growth and instability. If there are more slow particles, on the other hand, $\partial F/\partial v|_{v=\omega/k} < 0$, and the wave will damp, giving its energy to the particles.

In CTX, a non-Maxwellian plasma exists since ECR heating is used for plasma production. Thus a deeply trapped energetic population is created which becomes unstable to HEI, when the pressure gradient exceeds the interchange criterion, $\partial\rho/\partial\psi > 0$. We will return to the topic of HEI in dipole geometry after discussing some basic dipole physics.

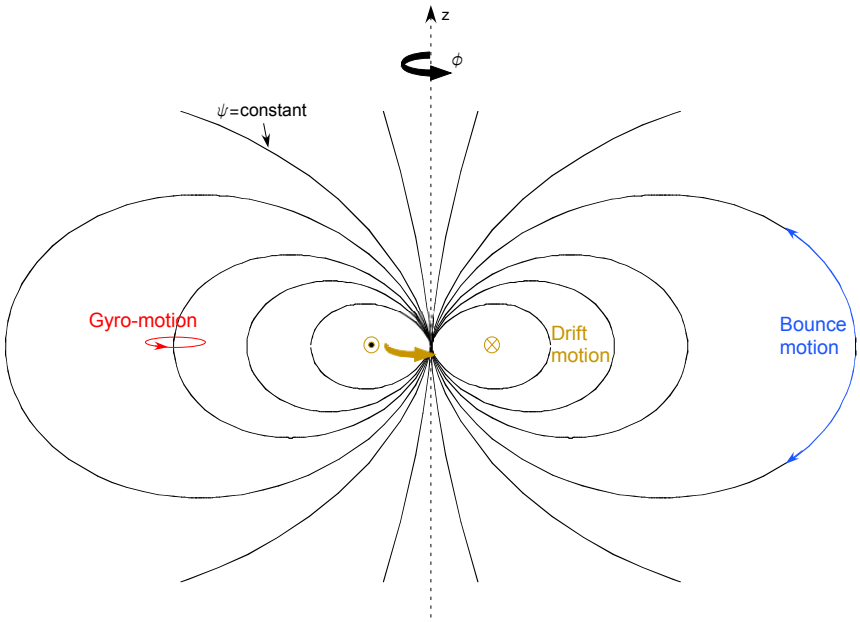

Figure 2.6: The ideal magnetic dipole, showing the three adiabatic particle motions.

2.2 Particle Motion in a Magnetic Dipole

A curl-free, axisymmetric ideal dipole magnetic field, Figure 2.6, is represented in magnetic (or Clebsch) coordinates as $\mathbf{B} = \nabla\varphi\times\nabla\psi = \nabla\chi$, where φ is the azimuthal angle of symmetry, ψ is the magnetic flux and χ is the magnetic scalar potential. The latter two quantities can be written in spherical coordinates as,

$$\psi = M\frac{\sin^2\theta}{r}, \tag{2.13}$$

$$\chi = \mathbf{M}\cdot\nabla\frac{1}{\mathbf{r}} = M\frac{\cos\theta}{r^2}, \tag{2.14}$$

where $\mathbf{r}$ and θ are spherical co-ordinates, and $\mathbf{M} = B_0L_0^3\hat{z}$ is the characteristic dipole moment. Field-lines are defined by (ψ,φ) while χ parametrizes the distance along a field line. It is often convenient to look at quantities only in the equatorial plane, since energetic particles will be deeply trapped in a high field dipole. The equatorial ($\theta = \pi/2$) radius is referred to as L [47], so that M is defined in terms of the field strength at a reference radius, L_0.

The magnitude of the dipole field has the familiar form:

$$B(r,\theta) = \frac{M}{r^3}\sqrt{(1+3\cos^2\theta)}. \tag{2.15}$$

2.2.1 Adiabatic Invariants

Charged particles in a dipole magnetic field have three nearly periodic motions, called adiabatic motions, which can be described by an action-angle description. The actions are called the adiabatic invariants and the angles are simply the frequency of the motion. The three motions are depicted in Figure 2.6 and are briefly explained here.

Cyclotron motion around magnetic field-lines is characterized by the cyclotron frequency $\omega_c = qB/m$ and the magnetic moment, or first adiabatic invariant, μ defined as

$$\mu \equiv \frac{mv_\perp^2}{2B}, \tag{2.16}$$

where m is the mass of the particle, q is the electron charge and $v_\perp$ is the velocity perpendicular to the magnetic field vector. The higher the energy of the particle, the larger μ is, the faster ω_c is and the smaller the orbit, given by $\rho_L \equiv v_\perp/\omega_c$, called the Larmor radius or gyro-radius. Provided no external perturbations are present that have $\omega \sim \omega_c$, the first adiabatic invariant of a particle is conserved during its motion.

The second adiabatic motion of charged particles in magnetic dipoles is the bounce motion, which requires that the first adiabatic invariant be constant in the following way. Particles are confined from moving across field lines by the cyclotron motion, yet they are able to move along these field-lines. As a particle follows a field-line into a region of stronger magnetic field (*eg.* moving toward the poles from the equator), $v_\perp$ increases to conserve μ at the expense of the parallel energy $E_\parallel = mv_\parallel^2/2$. Ultimately, a point where $E_\parallel = 0$ can be reached where all the particle energy is perpendicular energy. A restoring force called the *Grad-B* force, $\mathbf{F}_{\nabla B} = -\mu\nabla B$, causes the particle to reflect back along the field-line. This sets up a periodic motion of the particle between high field ends of a field-line. This is the bounce motion, which is the mechanism for plasma confinement in a dipole. The bounce motion is characterized by the second adiabatic invariant J, defined as

$$J \equiv \oint mv_\parallel ds, \tag{2.17}$$

where s is the distance along the field line and is related to the magnetic potential through $ds = d\chi/B$. For completeness we include the the frequency of the bounce motion, ω_b,

$$\omega_b = \frac{2\pi}{T_B} = 2\pi \left(\int \frac{ds}{v_\parallel} \right)^{-1}, \tag{2.18}$$

where T_B is the period of the bounce motion.

Note that particles with little perpendicular energy can escape the dipole field. Conversely, particles with large perpendicular energy are deeply trapped and bounce very near to the equatorial plane. These particles have $J \approx 0$. Again, this motion is conserved if no perturbations on the order of ω_B are present.

The final adiabatic motion is the drift motion. This results from the particle drift caused by the previously mentioned Grad B force. From Lorentz's equation, any force perpendicular to $\mathbf{B}$ will cause a particle velocity in the direction normal to both the new force and $\mathbf{B}$. In this case, we have,

$$\mathbf{u}_d = \frac{\mathbf{F} \times \mathbf{B}}{qB^2} = \frac{\mu}{q} \frac{\nabla B \times \mathbf{B}}{B^2}. \tag{2.19}$$

This drift is in the azimuthal direction, and causes positively and negatively charged particles to drift in opposite directions due to the q dependence, creating a current. The third adiabatic invariant, or action, that characterizes the drift motion around the dipole can be defined as [53]

$$\psi = \oint m E_\perp d\varphi \tag{2.20}$$

where $E_\perp = \mu B$ is the perpendicular energy, and φ is the azimuthal angle. This is also equal to the magnetic flux enclosed by the particle's precessional orbit, hence the label ψ.

In strongly-magnetized plasmas the three characteristic frequencies have very different time scales [51]. In CTX $\rho_L/L \ll 1$ and so $\omega_c \gg \omega_b \gg \omega_d$ and the corresponding actions, the magnetic moment, μ, the longitudinal adiabatic invariant, J, and the magnetic flux, ψ, are approximately constant.

2.2.2 HEI in Dipole Geometry

If the condition that the adiabatic motions be conserved is relaxed, instability and stochastic particle transport across the magnetic field lines can result. As mentioned, this requires a force that changes on a time-scale comparable to the periodicity of the given adiabatic motion [59, 1, 48]. When non-axisymmetric fluctuations of geomagnetic or electric fields resonate with the precessional drift of the particles, $\omega \sim m\omega_d$, where m is an interger, the time variation of the third adiabatic invariant ψ can become chaotic. This can lead to plasma instability.

In the Collisionless Terrella Experiment, electrostatic fluctuations are observed on the time scale of ω_d. These are drift-resonant fluctuations which break the conservation of ψ. Outward radial transport is observed which is the interchanging of inner flux tubes of dense plasma with less dense plasma contained by outer flux tubes. These pressure driven interchanges occur when the hot electron pressure gradient exceeds the critical profile. The population of energetic electrons are rapidly ∇B drifting at $\omega_d \sim 1$ MHz, which gives the instability a real frequency $\omega \leq \omega_d/2$ in addition to the purely unstable growth (discussed in Sec. 6.3).

Since these low-frequency interchange fluctuations break only the third adiabatic invariant, ψ, through resonant interaction with the rotating potential structures, μ and J remain constant even when the radial transport is chaotic [72]. In our simulations, invariance of (μ, J) serves as the "equation of state" for modeling adiabatic, collisionless heating or cooling during the radial flute motion of the energetic electrons induced by electrostatic fluctuations in a dipole.

This simulation will be employed in global mode structure comparisons of both the HEI instability in Chapter 4 and the centrifugally driven instability in Chapter 5.

Chapter 3

Collisionless Terrella Experiment

Measurements reported in this work were made using the Collisionless Terrella Experiment (CTX) located in Columbia's Plasma Physics Laboratory. The design goal of CTX is to study fundamental dynamical processes of plasmas confined by the field of the magnetic dipole. When an "artificial radiation belt" of energetic electrons is created with electron cyclotron resonant heating (ECRH), a variety of drift-resonant waves and fluctuations leading to stochastic radial particle transport and nonlinear frequency sweeping are observed. In addition, radial electric fields can be induced in the CTX device which cause $\mathbf{E} \times \mathbf{B}$ rotation and the study of rotationally induced instabilities. This chapter describes the specifics of the CTX device as well as the tools and diagnostics used to study and control plasma instabilities under investigation.

3.1 CTX

3.1.1 Vacuum System

In CTX, a dipole electromagnet is suspended mechanically inside an aluminum vacuum vessel 2 cm thick and 140 cm in diameter. Figure 3.1 shows the photograph and general layout of the CTX device. Figure 3.2 displays the schematic diagram of the internal dipole electromagnet assembly, various diagnostics as well as the magnetic field topology. A stainless steel enclosure electrically grounded to the vacuum chamber surrounds the magnet and

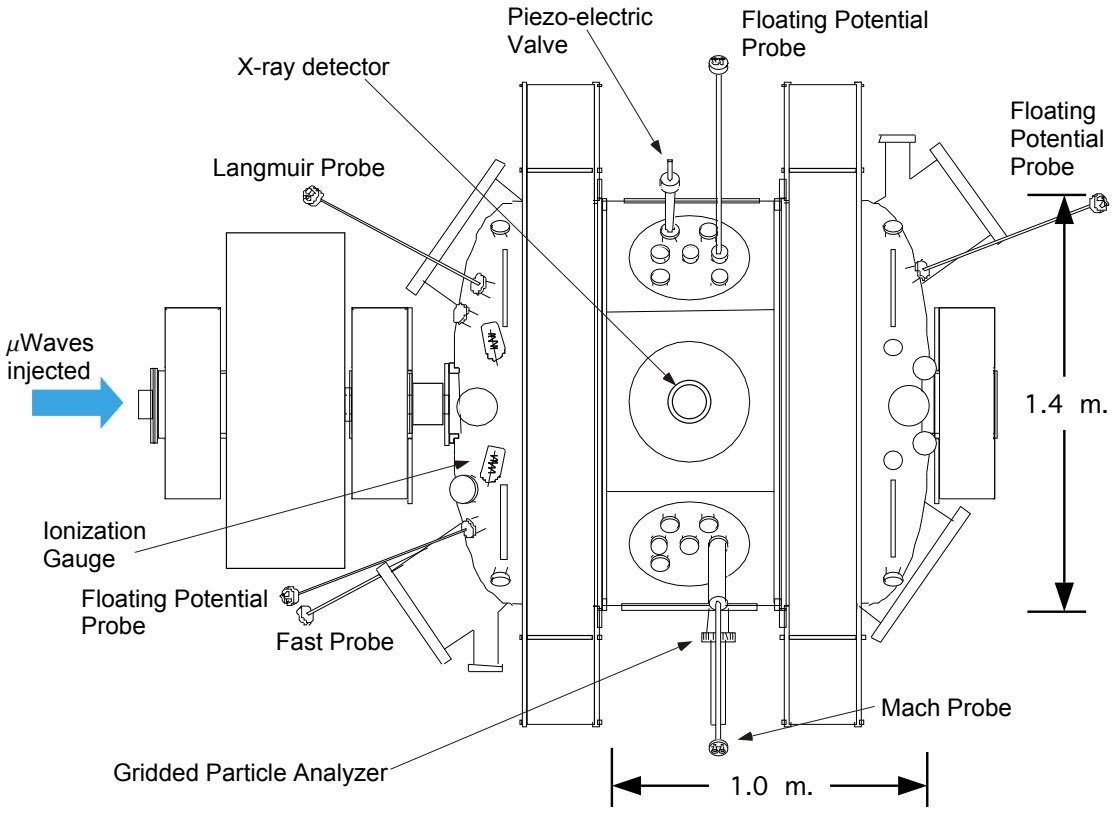

Figure 3.1: The Collisionless Terrella Experiment

houses the electrical and cooling leads.

An ultrahigh vacuum with an operating pressure of $p \sim 2 \times 10^{-7}$ Torr is created using a combination of pumps: a turbomolecular pump with the pumping speed of 1500 liters/sec is then used to lower the vacuum pressure below 10^{-6} torr; and finally a cryopump with the pumping speed of 2000 liters/sec is used to reach the operating vacuum pressure of $p \sim 2 \times 10^{-7}$ torr. Due to relatively low density of the plasmas created in CTX, the cryopump can operate anywhere between $3 - 6$ months without the need for a regeneration procedure depending on the plasma density regime studied and the rate of shots taken. Ionization gauges are used to monitor the pressure within the vacuum vessel.

During operation, hydrogen gas is puffed into the vacuum vessel through a high-voltage fast-switching piezo-electric valve. Depending on the length and number of gas puffs, different plasma density regimes can be achieved. Typically, single $3-5$ μsec gas puff is used to create plasmas with a particle density of about $n \simeq 10^9 - 10^{10}$ cm^{-3}.

3.1.2 ECRH

Electron cyclotron resonance heating (ECRH) is used to create and heat the plasma and to control the dynamics of the observed instabilities.

A continuous high-power wave magnetron with peak output of 1.6 kW of power at 2.45 GHz, is employed to ionize hydrogen gas. The microwaves propagate along a wave guide which connects the magnetron with the vacuum vessel and are plane polarized before being launched into the plasma above one of the polar regions. The vacuum chamber acts as an effective microwave cavity; waves make many passes through the plasma until they are finally absorbed by resonant electrons. A directional coupler in the wave guide measures forward and reflected microwave power.

The resulting plasma consists of a cold background plasma as well as an "artificial radiation belt" of energetic electrons with energies in the range of $1 - 60$ keV. Three subpopulations of electrons are distinguished: hot electrons with energies above 20 keV, warm electrons with energies between 1 and 20 keV, and cold electrons with energies below 1 keV. The dipole field has the strength of 15 kG at the face of the magnet and falls off to approximately 50 G at the wall of the vacuum chamber. Because the cyclotron frequency is

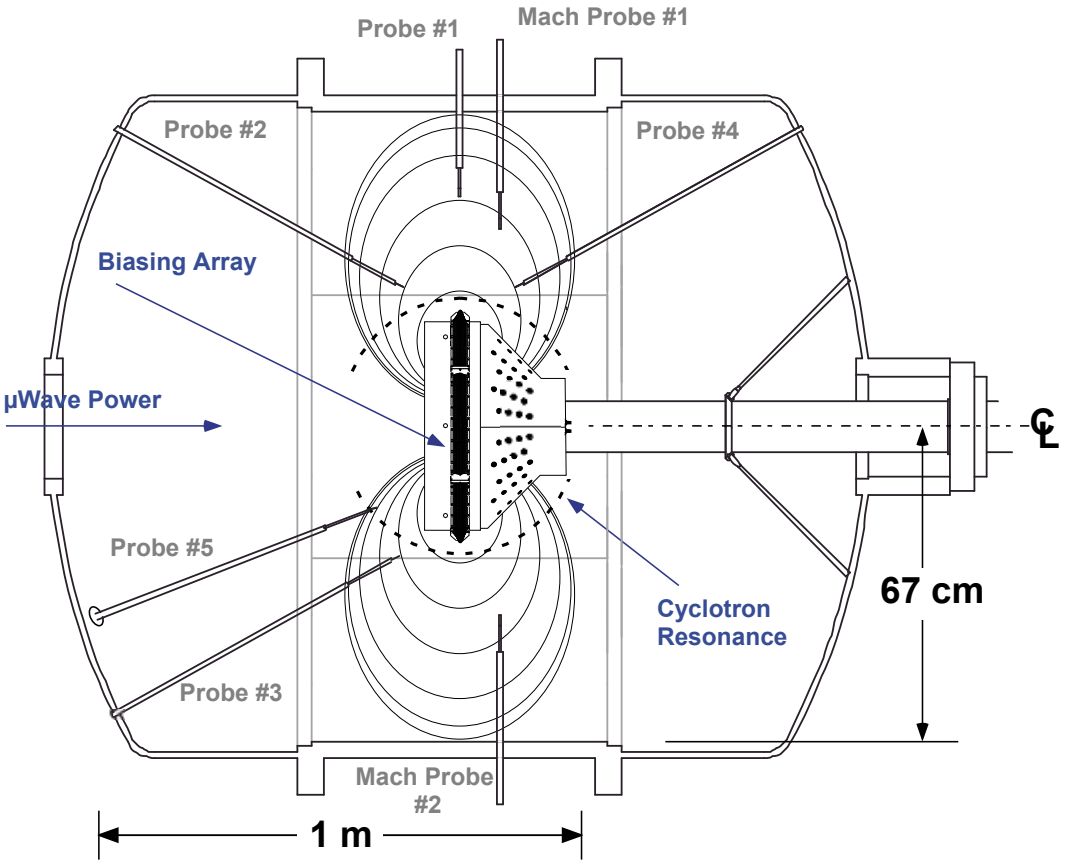

Figure 3.2: Schematic of CTX. A general layout shows The vacuum vessel, magnetic topology, microwave resonance location, diagnostics and new installations to the device to be discussed in Sec. 3.3.

directly proportional to the strength of the local magnetic field, $\omega_{ce} = qB/cm_e$, the fundamental microwave resonance, $\omega_{ce} = \omega_{ECRH}$, is defined by $B_0 \equiv 875$ G. This essentially defines a spherical surface, which intersects all field-lines that cross the equator with radii $L \geq L_0 \equiv 27$ cm. Since the rate of heating is proportional to the amount of time an electron is resonant with the wave, ECR heating is the strongest for deeply trapped particles ($\mu B \gg J\omega_b$) mirroring at the equatorial location of $L_0 = 27$ cm.

The cutoff density for propagation of electromagnetic waves in plasma is determined by the plasma frequency, $\omega_{pe}^2 = 4\pi e^2 n/m_e$. Thus, for the heating microwaves to be absorbed by the plasma, the CTX density must be below $n < 7$ x 10^{10} cm^{-3}.

3.1.3 Magnetic Field

As can be seen in Figure 3.2, several of the probes are not located within the equatorial plane of the dipole field. Often, however, it is desired to plot probe data as a function of the equatorial location the probe tip maps to along field lines. This can be done easily with knowledge of the magnetic field. The CTX field is produced by a current winding pack (12x14) housed inside the terrella. The latter is easily computed using a standard Green's function for the poloidal flux,

$$\Psi(x,z) = \sum_i I_i G(x,z,x_i,z_i), \qquad G = \mu_o \sqrt{\frac{x x_c}{k^2}} \left[(2-k^2)K(k^2 - 2E(k^2) \right],$$
$$k^2 = \frac{4 x x_c}{((x+x_c)^2 + (z-z_c)^2)},$$

where x and z are cartesian coordinates, x_i and z_i are the radius and height of the coils, and $E(k^2)$ and $K(k^2)$ are elliptic functions.

To map an arbitrary probe location back to the equatorial plane one calculates the flux at the given probe location and solves for the equatorial location that produces the same value of the flux. The calculated field is shown in Figure 3.3 (red), along with the field calculated assuming an ideal dipole (blue), showing, in fact, how useful the ideal dipole approximation is, warranting its use in many of the calculations discussed here.

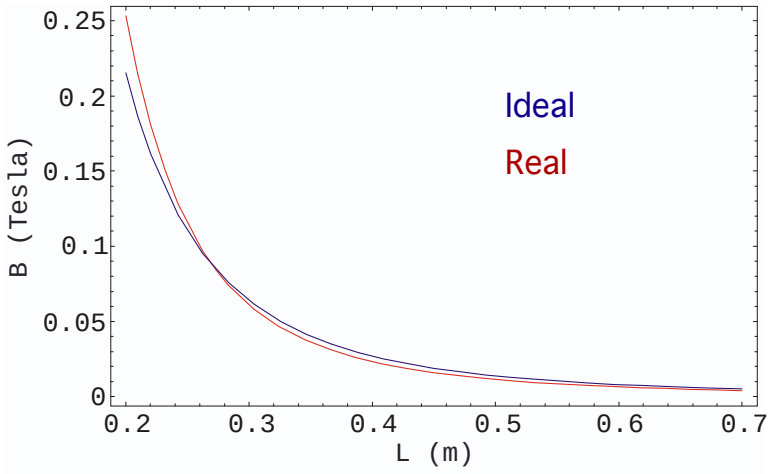

Figure 3.3: CTX dipole magnetic field, ideal (blue) and real (red).

3.2 Diagnostic Equipment

Relatively low plasma densities in CTX enable the use of intrusive diagnostics, such as Langmuir probes. The probes can be repositioned radially within the vacuum vessel to examine plasma properties at different field lines. Only when the diagnostics are placed within a few centimeters of the center of the energetic electron ring ($L_0 = 27$ cm), do they begin to perturb the plasma appreciably.

3.2.1 Electrostatic probes

A series of Langmuir and floating potential probes are situated throughout the CTX vacuum vessel (see Figs. 3.1 and 3.2) are used to measure plasma fluctuations and ion flow.

Langmuir Probe The CTX Langmuir probes consist of a copper co-axial cable enclosed in ceramic insulation. A stainless steel casing surrounds the assembly with a stainless steel square (1×1 cm^2) attached to the nickel wire to increase the collection area and, hence, the strength of the signal measured (Figure 3.4B). It is typically biased at -200 V to collect the ion saturation current (see diagram 2 in Figure 3.4). The plasma density can then be deduced according to Ref. [27]

$$I_{sat} \approx \frac{1}{4} q A n_i \bar{v}_i \tag{3.1}$$

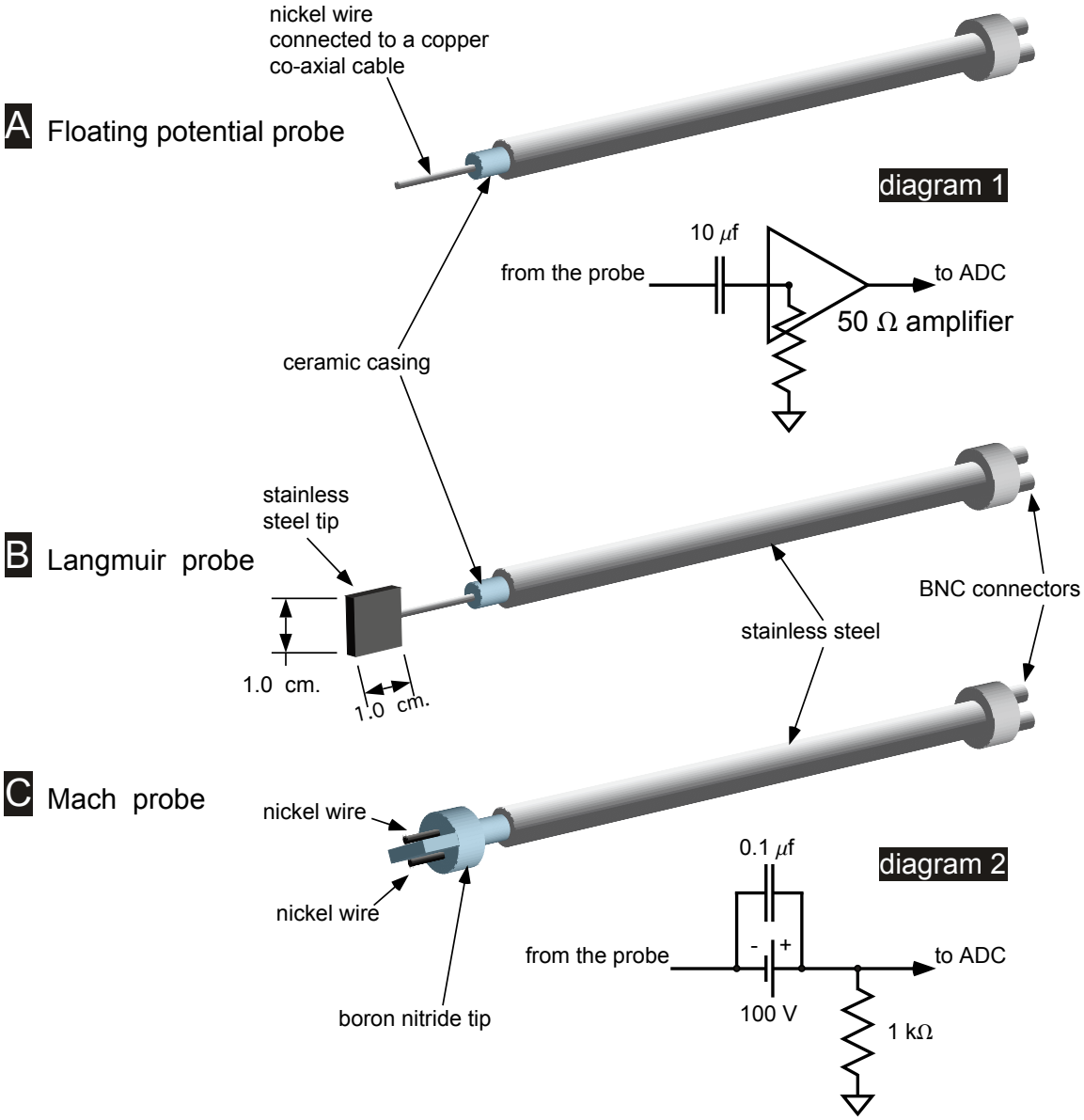

Figure 3.4: Electrostatic probes used in CTX. A) Floating potential probe. B) Langmuir probe, and C) Mach probe [Maslovsky (2003)].

where, I_{sat} is the saturation current measured by the probe through the termination resistor, q is an electron charge, A is the area of the probe, n_i local ion density, and $\bar{v}_i$ is the ion sheath velocity which is proportional to $(T_e/m_i)^{1/2}$. Here, m_i is the ion mass.

Floating Potential Probe A floating potential probe is a Langmuir probe that has a 100 kΩ resistor attached at the tip. The signal is amplified through a matched wide-band amplifier and then digitized (see diagram 1 in Figure 3.4). The floating potential fluctuations measured by the probe are related to the plasma potential fluctuations according to Hutchinson [27],

$$V_{float} \approx V_{plasma} - 2.83\frac{T_e}{q} \tag{3.2}$$

where T_e is an electron temperature in eV, and q is an electron charge.

Mach Probe A Mach probe consists of two Langmuir type probes biased in the ion saturation regime and separated by an insulated tip as shown in Figure 3.4C. This enables measurement of the differential plasma flow velocity by positioning the tip of the probe so that one electrode is collecting an upstream current and the other one the downstream current. The Mach number of the plasma flow, which is the ratio of the ion velocity to the plasma sound speed, can then be determined according to [26, 27, 22]:

$$M = \frac{1}{2}\ln\left(\frac{I_{sat\ upstream}}{I_{sat\ downstream}}\right) \tag{3.3}$$

The upstream electrode views a Maxwellian distribution of velocity shifted in the positive velocity direction, allowing the upstream probe to collect more current relative to the stationary plasma. The opposite situation occurs for the downstream electrode. This electrode sees the plasma moving away from it with a Maxwellian distribution shifted in the negative velocity direction. Thus, the downstream electrode collects less current. A comparison of the upstream and downstream currents allows the determination of the plasma velocity.

All of the described electrostatic probes can be repositioned radially to examine fluctuations at different field lines. Signals from the probes are typically digitized with a LeCroy 8212A data logger for slow-varying signals, and with LeCroy TR6841 transient recorder for fast-varying signals.

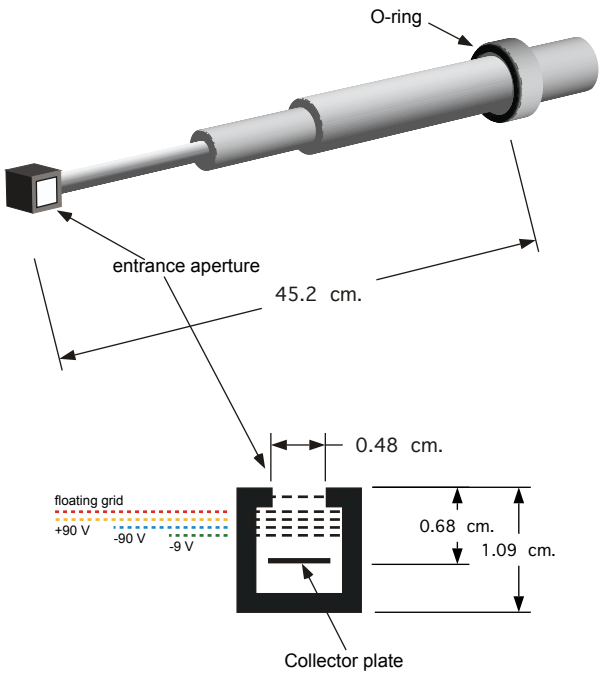

Figure 3.5: Gridded particle analyzer [Maslovsky (2003)].

3.2.2 Gridded particle analyzer

To study the transport of energetic electrons, a movable gridded particle analyzer is employed, Figure 3.5. It is located 13 cm above the equatorial mid-plane, and consists of a series of grids approximately 1.5 mm apart inside a stainless steel box which has an opening centered on one side. The grids are biased to repel ions and electrons with energies less than 90 eV. The first two grids of the particle analyzer are left floating, the third grid is biased at +90 V to repel ions, the fourth grid is biased at −90 V to repel electrons, and, finally, the grid closest to the collector plate is biased at −9 V to repel secondary electrons from the collector plate. Current is collected on a metal plate 0.23 cm^2 and is carried along a 50 Ω co-axial cable which is typically terminated into a 10 kΩ load. By changing the value of the termination resistor, different time-response values can be achieved. The signal is then amplified with an AM 502 differential amplifier and digitized with a LeCroy TR6841 8-bit transient recorder.

The entrance aperture of the probe can be rotated with respect to the local magnetic field vector. During the experiments described here, it was positioned perpendicular to the

magnetic field, and a time-averaged energetic electron flux was computed.

3.2.3 X-rays

In CTX, x-ray emission is used to infer the amount and energy of energetic electrons. When $1-60$ keV electrons produced during a CTX discharge are decelerated via cold ion and neutral atom collisions, hard x-ray radiation is produced. The amount of x-rays is proportional to $n_e \cdot n_n \cdot n_i$, where n_e is the hot electron density, n_n is the density of the neutral atoms, and n_i is the ion density. The x-ray radiation is detected with a krypton proportional counter located on top of the vacuum vessel (Figure 3.1) through a quartz window. The x-ray detector was calibrated to account for the window and port cover absorption using samples of radioactive Co-57 and Fe-55 and can be configured to provide pulse count or continuous output of collected x-rays.

In addition to the hard x-ray measurements, an array of three soft x-ray diodes focused on the inner, central and outer plasma regions respectively, measure line-of-site averaged plasma density at these three regions. These offer a method to estimate the electron pressure profile.

3.3 Installations to the CTX Device

New installations to the CTX device have been designed to extend the versatility of the experiment. To extend the understanding of interchange modes to those induced by plasma rotation, a new diagnostic and plasma control system has been installed to alter the plasmas electrostatic potential and to diagnose polar currents and particle fluxes.

A schematic of the new installations is shown in Figure 3.6 along with the magnetic field lines and magnetic field strength of the CTX experiment.

3.3.1 Equatorial Tungsten Mesh Biasing Array

An array of six individually biased tungsten meshes have been installed in the CTX device, distributed equatorially onto an insulating shell mounted onto the terrella. This equatorial array is designed to alter the electrostatic potential of the plasma by biasing inner fieldlines with respect to the vacuum chamber wall. The resulting electric field causes the plasma to

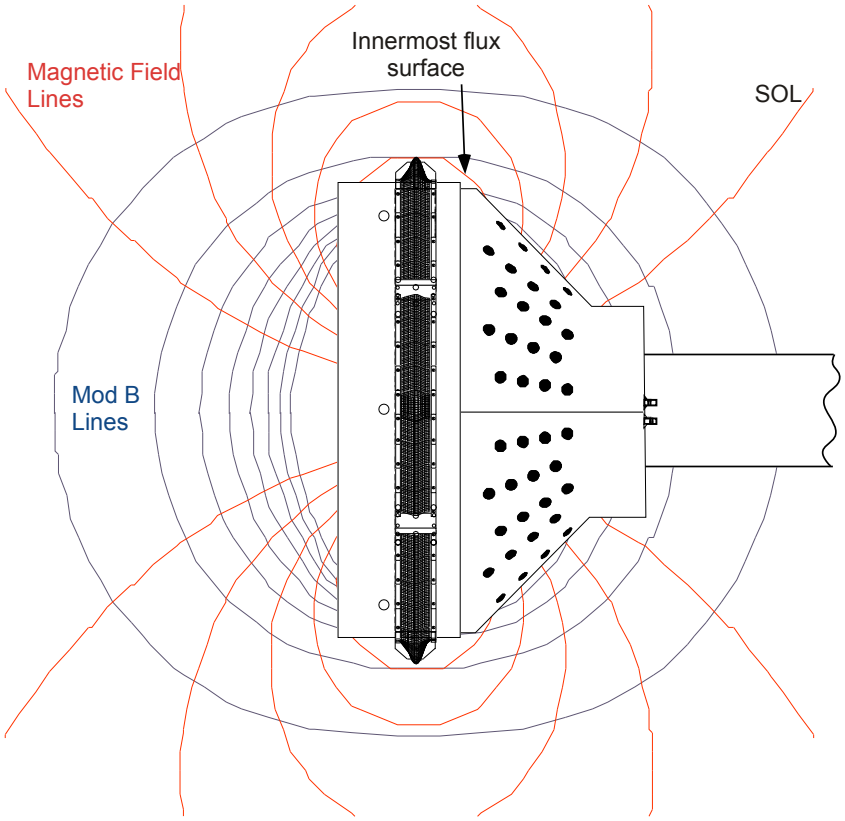

Figure 3.6: A schematic of the tungsten filament bias cap and gridded particle detector array in relation to the terrella electromagnet and magnetic field lines (red) and field strength (blue) of CTX. The locations of the particle detectors can be seen, as well as the equatorial tungsten mesh assembly.

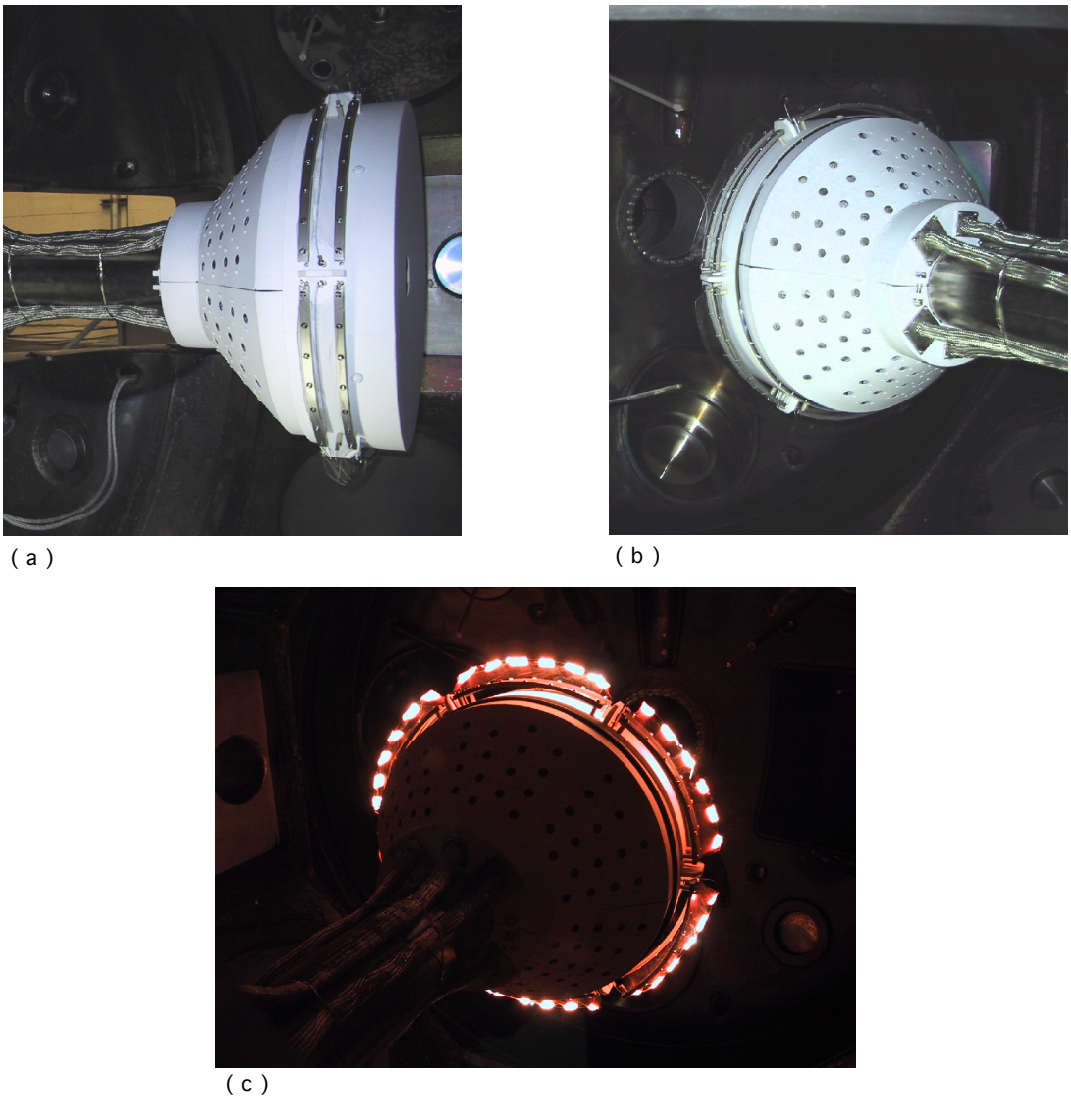

Figure 3.7: Photograph of the installations: (a) the tungsten meshes can be seen along the circumference of the cap; (b) the polar imaging diagnostic array, and; (c) the tungsten filament array in operation.

rotate azimuthally via the $\mathbf{E} \times \mathbf{B}$ drift. When the filament potentials are adjusted within the range 100V-1kV, significant modifications to the plasma's electrostatic potential occur. Peak radial electric fields of ~ 20 V/cm and plasma mass flows corresponding to orbit frequencies more than 100 kHz are seen. A significant part of this investigation involves the study of the effect of plasma rotation on the dynamics of intense interchange instabilities in a magnetic dipole, including the excitation of the rotational Rayleigh Taylor instability.

A photograph of the biasing system is shown in Figure 3.7(a). The bias cap itself is built from a spun stainless steel dish plasma-spray coated with 12 mil thickness of alumina. Such a coating insulates to roughly 4-5 kV, and is compatible with ultra-high vacuum operation. In Figure 3.7(c) the mesh array is shown in steady state operation, employing a DC power supply with a current of 25 A and a voltage of 35 V, while the emission current was several mA, corresponding to about 0.5 W of power. In addition, a capacitively pulsed power supply has been built and discharges up to 200V in 0.1-0.2 seconds, which heats up the filaments to approximately 1500-2000 K. The biasing power supply is a Bertan Associates Inc. (BA) Model 210-05R high voltage power supply, with peak output of 5 kV and 40 mA. A schematic of the biasing system is shown in Figure 3.8(a), with a circuit diagram of the filament pulser shown in Figure 3.8(b). The voltage divider is used to monitor the bias on the meshes directly, while the bias power supply voltage and current monitors are also digitized and monitored during experiments.

The individual tungsten filaments are 22x15 cm^2, with a wire thickness of 0.001" and mesh density of 100x100 wires/cm^2. Picture of the mesh and the stainless steel clamps used to connect it to the insulated bias cap are shown in Figure 3.9.

The independence of the meshes allows application of axisymmetric as well as nonaxisymmetric potentials. Potentials with a symmetry up to $m = 3$ are possible. This allows the study of driven, non-axisymmetric plasma convection, and synchronous application of potentials to the plasma. For the investigations discussed here, however, the meshes were run almost entirely in series, as an axisymmetric $m = 0$ potential.

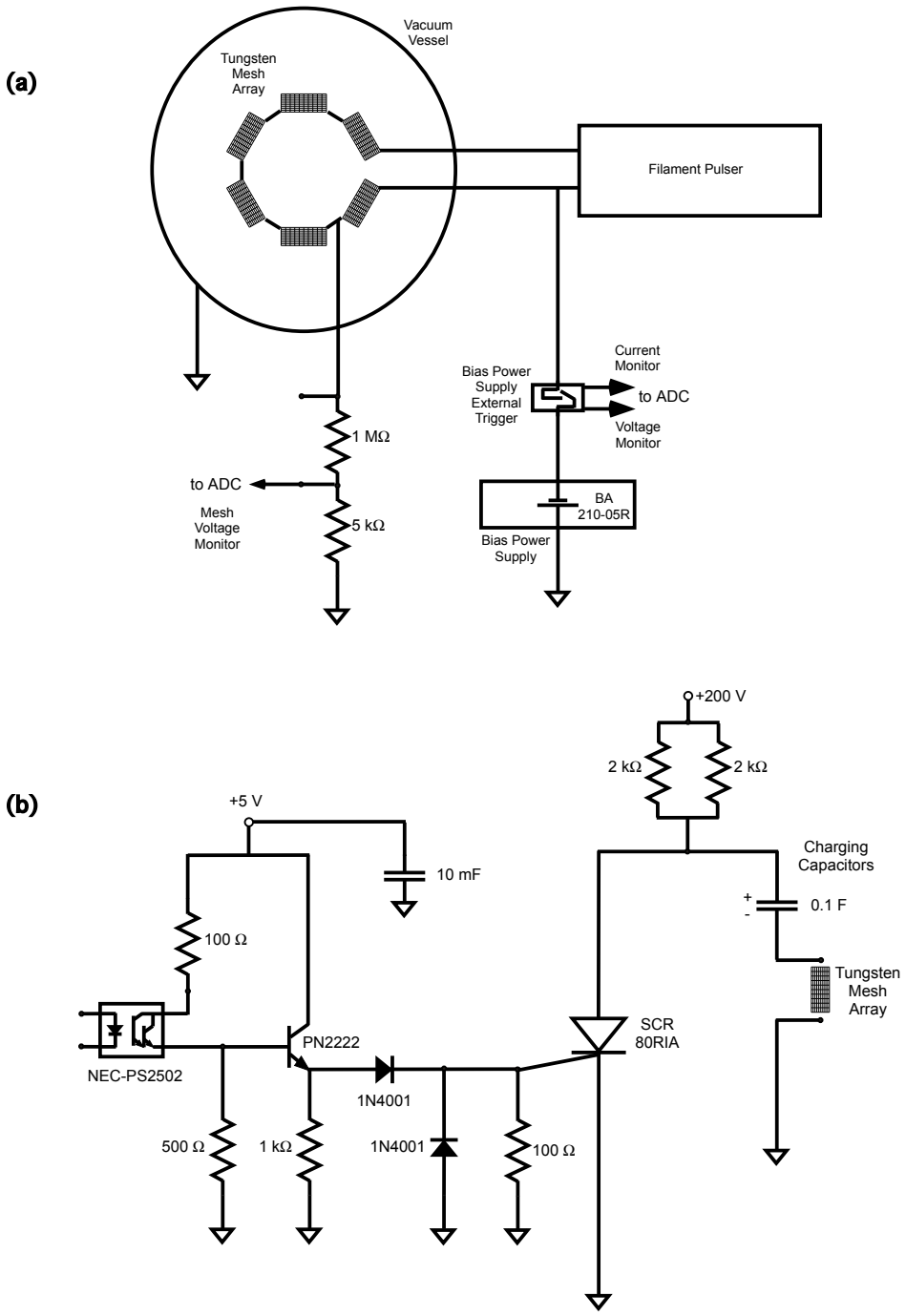

Figure 3.8: (a) Schematic of the biasing system of the tungsten mesh array and, (b) circuit diagram of the filament pulser power supply.

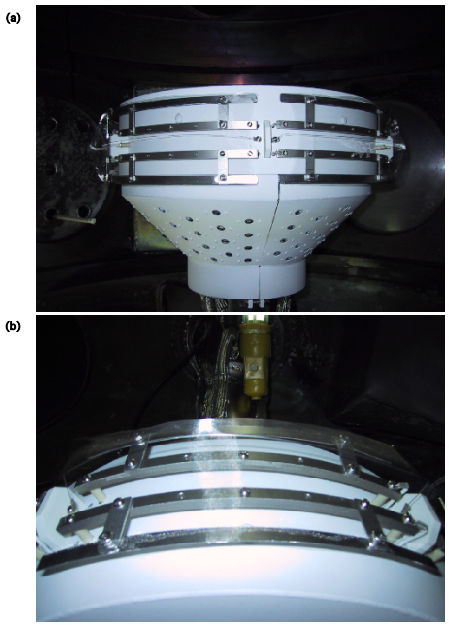

Figure 3.9: Pictures of a tungsten mesh and the clamp assembly.

3.3.2 Polar Gridded Energy Analyzer Imaging Diagnostic

On the opposite side of the terrella to the filament cap, another insulated polar cap is mounted, shown in Figure 3.7(b), housing an array of 96 polar particle detectors. The apertures for these detectors are 1 cm^2. The particle detectors are distributed uniformly on a rectangular grid in the natural, magnetic flux coordinates (φ,ψ). Due to past research support, we have on-hand 72 channels of high-speed, high-bandwidth transient recorders (1 MHz, 14 bit, 128 ks/record), multi-pin vacuum feed-throughs, and transimpedance amplifiers. The detector provides a good approximation to the bounce-averaged phase-space distribution, F, by measuring the flux of energetic electrons scattered to the poles as a result of electron-neutral collisions. The detectors have three biasing grids as well as a current collector plate. The grids are typically biased at +500 V to repel ions, −2 kV for electrons and −9 V for secondary electrons, respectively. An individual detector schematic is shown in Figure 3.10.

The detectors collect polar particle flux integrated along fluxtubes, as shown in Figure 3.6. The grid of detectors consists of eight radial locations by 24 azimuthal locations. The radial

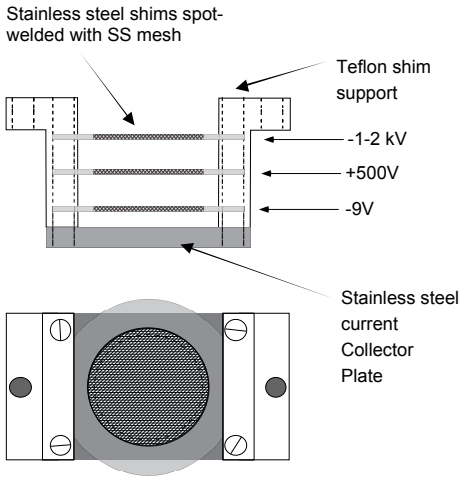

Figure 3.10: Photograph of the tungsten filament array in operation.

extent of the volume collected by the imaging diagnostic ranges from the innermost flux surface to the scrap off layer (SOL), which corresponds to the last closed fieldline.

Chapter 4

Curvature Driven Instabilities in CTX

This chapter describes the type of magnetic curvature driven instabilities seen in the CTX device, namely, the Hot Electron Interchange (HEI) instabilities. After giving a physical description of the modes we then introduce the multi-probe correlation analysis and the global mode structure it is used to determine. This mode structure is then compared with a self-consistent nonlinear simulation which shows marked agreement with experiment. These results constitute the first measurement of the global mode structure of the low frequency HEI instability, and were first reported in Ref. [36]

4.1 Observation of HEI

In the presence of an intense hot electron population, drift-resonant ($\omega \sim m\omega_d$) fluctuations are observed, both during and after the microwave heating pulse. Some characteristics of the fluctuations in these two time periods are different. With the heating on, the fluctuations appear as repetitive short bursts, 300-500 μs, while during the afterglow they may last as long as several msec. In addition, the afterglow fluctuations have a higher frequency, with coherent modes rising in time up to 20 MHz. During the heating regime, the fluctuations are generally observed to have $f \leq 5$ MHz and have a more dynamic, rapidly-changing spectral content. In both intervals, the frequency spectrum is complex and time-varying, exhibiting rising tones in time.

Figure 4.1 shows the floating potential fluctuations on various relative time scales. The

first figure shows a long time scale, and instabilities are present both during heating and during the afterglow. The mode amplitude typically saturates at a level between 100-200 V. On a faster time scale, the fluctuations are seen to be non-sinusoidal and slowly change in time. This change represents the presence of multiple azimuthal modes with frequencies that evolve at different rates. When the same fluctuations are observed by two probes that are azimuthally separated by 90°, the phase difference indicates a low-order mode structure that rotates in the direction of the electron ∇B drift.

The differing nature of the instability during and after the microwave heating phase can be explained as follows. Instability bursts eject plasma radially, flattening the pressure profile that drove it unstable. Since the microwave is still producing plasma, the pressure gradient builds up again, driving the instability in this periodic fashion. In the afterglow, plasma production has ceased, and the colder stabilizing plasma recombines first, leaving the unstable hot electrons to persist, until they themselves eventually recombine.

4.2 Correlation Analysis

Five movable high impedance floating potential probes (with 100 kΩ tips) are located at various positions in the plasma. These probes are used to reconstruct the mode structure using cross-correlation analyses of combinations of probe pairs and a fixed "reference" probe. Although the movable probes can access regions extending from the dipole magnet to the vacuum chamber wall, measurements are possible only when the probe's location does not interfer with the bulk of the energetic trapped electrons. Referring again to Figure 3.2, four of the five probes are inserted at a ±30° angle with respect to the dipole's axis. These probes can be inserted very near the electron cyclotron resonance ($R \sim 27$ cm) since the most deeply trapped electrons have insufficent parallel velocity to strike the probe. In contrast, the probe inserted at the equator can be inserted only to approximately $R \geq 45$ cm.

Since the magnetic field line geometry is known, the probe positions can be expressed with a geometric labeling of the magnetic coordinates in analogy with McIlwian.[47] The radial coordinate for a field line is its equatorial distance, R. Distance along a field line is labeled by s, and the azimuthal coordinate is φ. The measured probe position is mapped to its equivalent magnetic coordinate, (R, φ, s), by numerical computation. Because the

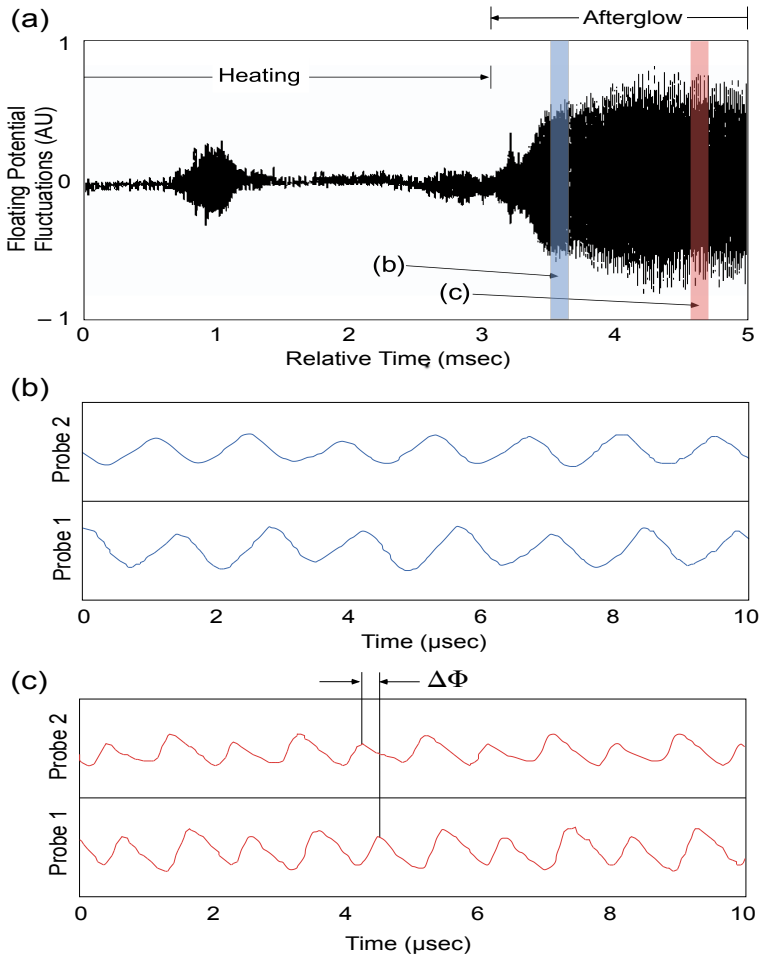

Figure 4.1: Floating potential probe signals of the drift-resonant instability on different time scales. (a) A long time scale shows an instability burst during heating and a saturated mode during the afterglow. On a faster time scale, (b) and (c), show the non-sinusoidal waveforms from two spatially-separated high-impedance probes that illustrate the phase difference between probes.

plasma pressure is low and because most of the plasma volume is sufficiently far from the dipole electromagnet, the field-lines follow approximately the trajectories from a point-dipole in vacuum. The CTX dipole moment is $M_0 = B_0 R_0^3 = 1.7 \times 10^7$ G cm^3, and an approximate relation exists between $(R,\, \varphi,\, s)$ and the usual magnetic coordinates for a point dipole, $(\psi,\, \varphi,\, \chi)$, defined by $\mathbf{B} = \nabla\varphi \times \nabla\psi = \nabla\chi$, where χ is the magnetic scalar potential. This relationship is simply, $(R,\, \varphi,\, s) \approx (M_0/\psi,\, \varphi,\, \int d\chi/B)$.

Measurement of the mode structure is complicated by the simultaneous presence of several modes, but it is simplified because the phase of the potential is constant along the field line. The quantities to be measured are expressed in terms of a modal prescription for the voltage measured by a probe located at $(R,\, \varphi,\, s)$,

$$\Phi(R,\, \varphi,\, s,\, t) \equiv \sum_{n,m} \Re\left\{\Phi_{n,m}(R,\, t) \exp\left[i(m\varphi + k_\parallel s + k_R R - \omega_n t)\right]\right\} \ , \tag{4.1}$$

where n is the mode index, and $k_\parallel$, k_R, and ω_n may be slow functions of time. The amplitude, $\Phi_{n,m}$ changes slowly in time, but we find it does not change in spatial structure. We also find the $|\Phi|$ does not change significantly with s over the region accessible with the probes. These observations justify the modal prescription *a posteriori*.

When the digitized signals from two probes are Fourier transformed, the transform of the correlation between two probes, $C(1,\, 2)$, is expressed as the product of one probe signal with the complex-conjugate of the second. In terms of the modal prescription, this correlation is

$$C_{n,m}(1,\, 2) \approx \Phi_{n,m}(R_1)\Phi^*_{n,m}(R_2) \exp\left[i(m\Delta\varphi + k_\parallel \Delta s + k_R \Delta R)\right] \ . \tag{4.2}$$

Since $\Delta s = s_1 - s_2$ and $\Delta R = R_1 - R_2$ are known, the phase of the correlation can be used to determine m, $k_\parallel$, and k_R. Our ability to use Equation 4.2 for mode analysis improves as the time rate of change of the mode frequency vanishes, $\partial\omega/\partial t \equiv \dot{\omega}_n \to 0$, or as the frequency separation between nearby modes becomes large. This is because we must Fourier transform the digitized waveforms with finite time-windows. Because the mode frequency is not constant, a simple fast Fourier transform can not be used to transform the probe signals. Instead, the slow-time evolution of the mode spectrum is computed using short-time Fourier transforms with a continuously moving triangular (or "Parzen") window, referred to as a spectrogram or a time-frequency-domain (TFD) signal representation.[69] The TFD of $C(1,\, 2)$ is computed from the product of the short-time fast Fourier transforms of two probes

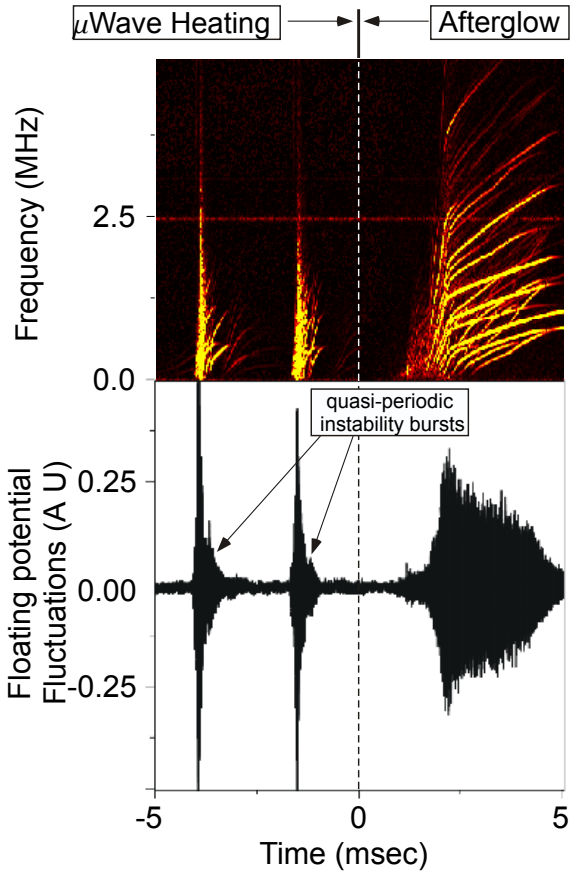

Figure 4.2: Floating potential signal and TFD showing HEI instabilities during heating and afterglow regimes [Maslovsky (2003)].

using identical, moving time-windows. Because the mode frequency evolves more quickly during microwave heating than during the afterglow, the time windows can be longer and the mode frequencies better identified during the afterglow. The short-time Fourier transform (STFT) [8], is given by

$$|STFT(t,f)|^2 = \left| \int_{-\inf}^{+\inf} x(u)w(u-t)exp(-i2\pi fu)du \right|^2 \tag{4.3}$$

where $x(u)$ represents the signal and $w(u-t)$ is some suitably chosen windowing function [71].

An example of a TFD showing both heating and afterglow instabilities is shown in Figure 4.2.

4.3 Measurement of Global Mode Structure

The overall procedure for measurement of the global mode structure can now be described. First, three probes are placed at the same azimuth, φ, and adjusted radially to be located on the same field line, R. The relative amplitude of the Fourier transform of the correlation of any two of these probes is used to determine the variation of $|\Phi_{n,m}|$ along the field, and the variation of the phase is used to measure $k_\parallel \Delta s$. This measurement is important since it establishes the flute-like nature of the electrostatic fluctuations and simplifies the analysis of the following measurements. We find $k_\parallel \approx 0$ for all modes, and the amplitude varies by less than 10% between the three probes. The second part of the procedure uses three probes to determine k_R and m from the phases of the correlations of two separated probes with a fixed reference probe located at $R = 49$ cm. Since these probes are located at different R, the phase information is meaningful only if the magnitudes of the correlations between all probes is large. Since the mode structures are broad, we find significant correlation for all modes and for all probes separations. The final step determines the radial variation of the mode amplitude by correlation analysis of a probe that is moved in increments approximately $\delta R \sim 2$ cm for successive plasma discharges. The ratio of (1) the correlation between this moving probe and the fixed reference probe and (2) the self-correlation of the reference probe results in the normalized radial mode structure for any given mode. This is defined as $\Phi_{n,m}(R_2)/\Phi_{n,m}(R_1) \equiv |C(1,\,2)|/|C(1,\,1)|$, and the profile is obtained as the position of the second probe, R_2, is moved relative to the fixed position of the first probe, R_1.

In order to illustrate the complexity of the frequency spectrum, the time-frequency domain of the magnitude of the correlation between two probes separated only in azimuthal angle is shown in Figure 4.3. In this example, $\Delta R \sim \Delta s \sim 0$, and $\Delta\varphi = 90°$. The figure shows the slow evolution of the potential oscillations during the afterglow, $\dot{\omega}_n/\omega_n^2 \sim 2\times 10^{-4}$. The modes with larger amplitudes are labeled by their azimuthal mode numbers, m. Note several modes exist simultaneously with the same azimuthal mode number but with different frequencies. For example, three modes with $m = 1$, $m = 2$, and $m = 3$ are identified. The frequencies of harmonic modes evolve in time at rates different from the fundamental, and this corresponds to the time-evolution of the non-sinusoidal waveform of the potential. An example of this harmonic structure are the modes at approximately 2.4, 4.7, 7.0, and

9.4 MHz. Many modes with different m number do not appear to be harmonically related (*i.e.* the ratio of frequencies are not rational numbers.) For example, several $m = 1$ modes co-exists near 1 MHz. The low frequency, $m = 1$, modes usually have the largest magnitude, but this is not always the case. The amplitudes of harmonic modes usually decrease with increasing frequency.

The relative amplitudes of the modes change appreciably in time, as can be seen from the TFD of the correlation magnitude. Often, the higher m modes begin to increase in magnitude as the mode evolves while the amplitude of the prominent $m = 1$ mode gradually decays. Sometimes the $m = 1$ and $m = 2$ modes have equal amplitude, and, occasionally, the $m = 2$ dominates. This observation necessitates our measurement of the normalized structure for each azimuthal mode using correlation analysis with the fixed reference probe. The radial mode structure must be reconstructed from many similarly-prepared discharges, but the relative amplitudes of the modes as well as their frequencies at any instant are never the same from discharge to discharge. However, we find the amplitude for any given mode at any given position relative to the amplitude at the fixed reference probe to be essentially time-invariant.

While two probes azimuthally separated were used to determine m, other probes positioned on the same field line were used to determine the field-aligned mode variation. For example, Figure 4.4 illustrates the phase difference between two probes with $\Delta R = \Delta\varphi = 0$, $R = 49$ cm, and $\Delta s \approx 35$ cm. These measurements were made for the same discharge as illustrated in Figure 4.3, and Figure 4.4 shows the phase difference, $k_{\|}\Delta s$, for the largest amplitude, $m = 1$ mode as a function of time. Similar analyses were made for other modes, and all modes show a constant phase structure along a field line. Since the equatorial probe was used for these measurements, only field lines having $R > 45$ cm could be accessed without perturbing the energetic trapped particles. The probe positions were approximately $s \sim 0$ and $s = \pm 35$ cm, and, for these positions, we find the relative mode amplitudes are comparable to within $\pm 10\%$. These measurements indicate the potential fluctuations are flute-like.

The final step in mode measurement procedure is to analyze the relative phase and amplitude of the correlation of two probes with increasing radial separation. Probes located off the equatorial midplane were used (probes #4 and #5 in Figure 3.2) since these probes

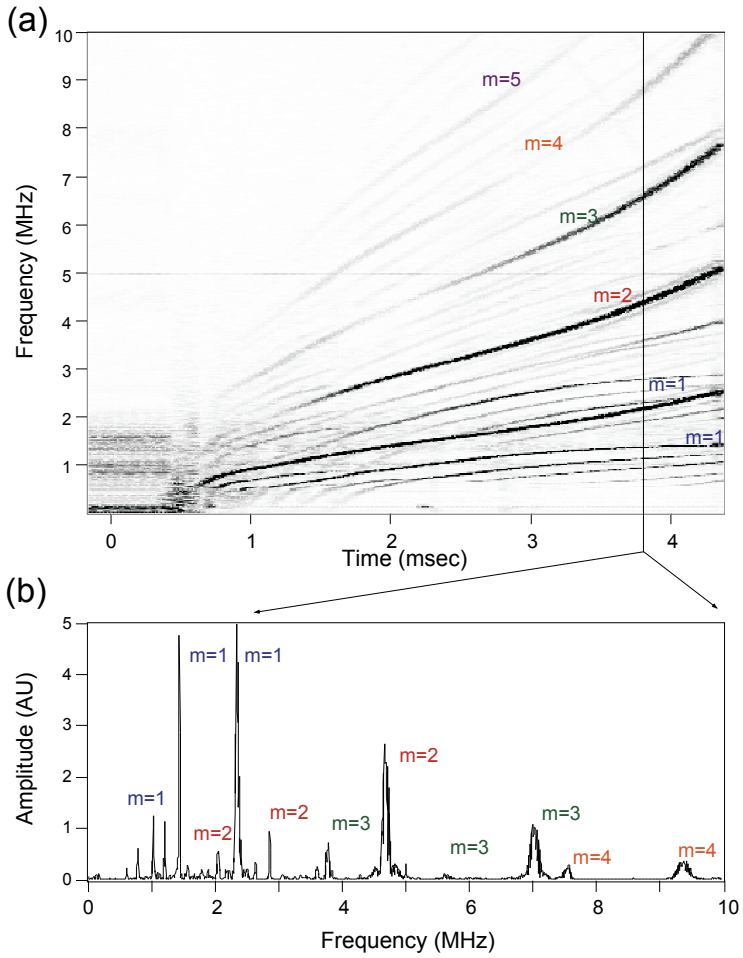

Figure 4.3: TFD of the magnitude of the correlation function of two floating potential probes with $\Delta R = \Delta s = 0$ and $\Delta\varphi = 90°$ graphed with a linear grey-scale. Shown below is the short-time frequency spectrum of the correlation at an instant during fully-developed and saturated oscillations. The azimuthal mode numbers are shown.

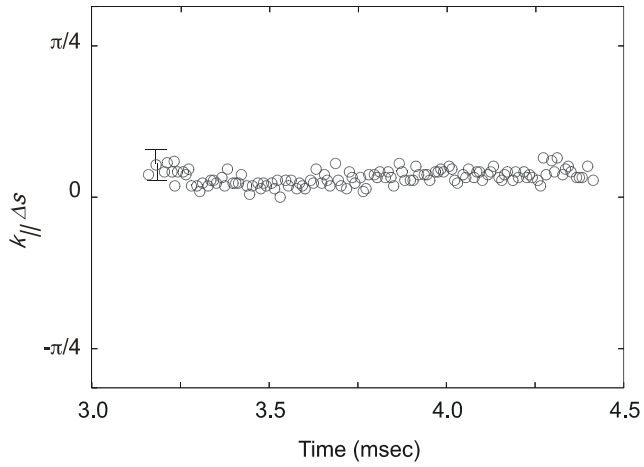

Figure 4.4: The field-line phase difference of the correlation function for two probes positioned at two locations along the same field line, $\Delta R = \Delta\varphi = 0$ and $\Delta s \approx 35$ cm, showing $k_{\|} \approx 0$ for several modes during the afterglow.

could be inserted deep into the plasma and near to the dipole magnet without disturbing the energetic electrons or the potential fluctuations observed by the reference probe. By using multiple probes, correlation analysis of the TFD identified both the azimuthal mode and the radial variations. Since $k_{\|} \sim 0$ and since m is known, probes located at any position within the plasma can be used to compute the radial correlations.

Figure 4.5 and Figure 4.6 show the results of these measurements. In Figure 4.5, the three lowest m numbers were examined at three different times in a single discharge but with each radial location representing averages of several shots having the movable probe at different positions. We observe no apparent time dependence in the phase, and there is no change in the phase with radius. Since $k_R \sim 0$, the mode structures rotate as rigid structures, with no phase lag. In Figure 4.6, the radial profile of the normalized magnitude of the two-probe correlation shows the radial structure to be broad and to depend weakly on the azimuthal mode. Higher m modes are seen to be more localized toward the core, as might be expected. In all cases, the mode structure extends from the edge to the inner hot electron region, and they are not localized to particular flux surfaces. In addition, no

time dependence is observed in these normalized profiles, as seen in Figure 4.7, although the relative amplitudes of one mode with the other are observed to vary in time. In making these observations, we find it noteworthy that the global mode structures are time-independent despite the complex and time-variation of the fluctuation's frequency spectrum.

4.3.1 Mode Structure in the Heating Regime

In addition to measuring the global mode structure of the HEI instability during the afterglow, equivalent measurements were made of the bursting interchange instabilities observed during microwave heating. As described by Warren,[69] clearly identified modes with well-separated frequencies are observed during the second half of every burst. The rate of change of the mode frequencies are approximately $\dot{\omega}_n/\omega_n^2 \sim 0.2$, considerably faster than during the afterglow. Nevertheless, modes with $m = 1$ and $m = 2$ were identified. We found the radial structure for these modes to be the same as shown in Figure 4.6; however, averaging over discharges showed a larger variance especially for the radial variation of the phase, $k_R \Delta R$.

The phase and normalized amplitude of the correlation function as a function of radius during the microwave heating are shown in Figure 4.8 and 4.9 respectively. Note that the azimuthal phase is not subtracted off from the total correlation phases plotted in Figure 4.8 for the lowest three m numbers, yet it is still clear that $k_r \sim 0$ for the heating modes. In Fig 4.9 the close comparison between the normalized correlation amplitude profiles during the heating and the afterglow regimes is marked, though the heating modes appear marginally steeper than their afterglow counterparts. However, recall that the actual magnitude of the modes during the afterglow is significantly larger.

4.4 Modeling the Nonlinear Evolution of the HEI Instability

This section describes the nonlinear, self-consistent simulation of the time evolution of the hot electron interchange (HEI) instability used to interpret measurements of the global mode structure. Previously, Ref. [44] described this simulation together with the linear dispersion relation for HEI instability in a dipole-confined plasma. For completeness, we review again

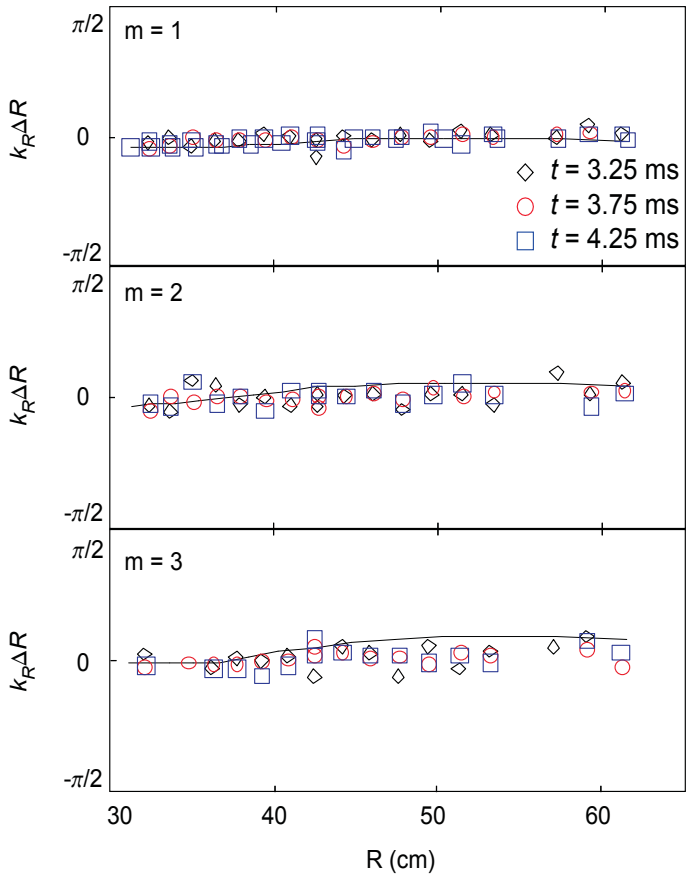

Figure 4.5: The phase of the correlation between two probes as the radial separation increased for the lowest three azimuthal modes. Results show $k_R \approx 0$ for all modes during the afterglow. Solid lines are the relative phase difference of global modes computed from the nonlinear simulation.

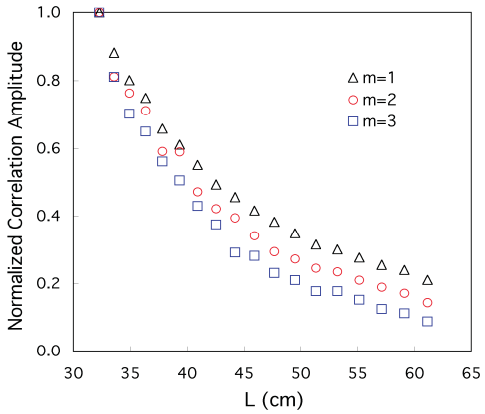

Figure 4.6: Comparison of radial mode structure of the normalized correlation amplitudes for $m = 1$, 2, and 3.

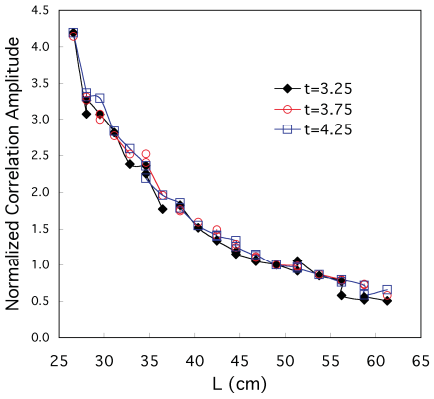

Figure 4.7: The normalized correlation amplitude for a $m = 2$ mode during three different times in a shot, showing no significant time dependence to the profiles.

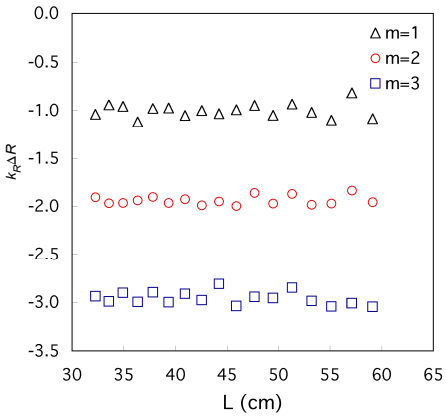

Figure 4.8: The phase of the correlation between two probes as the radial separation increased during the microwave heating for the lowest three m numbers.

the basic model equations and, then describe more fully the numerical procedure used to compare simulation with measurement.

The simulation solves finite-difference approximations to the coupled, nonlinear model equations for the evolution of the electrostatic potential and the field-line integrated number densities of ions and energetic electrons. The simulation is similar to those described by Refs. [74] and [58]. The electrostatic potential is advanced by solving the equation for charge continuity subject to reasonable boundary conditions. However, unlike these other nonlinear simulations, multiple groups of particles must be evolved simultaneously in order to capture the drift-resonance between the energetic electrons and the azimuthal propagation of the interchange instability. Refs. [74] and [58] required only a single equation for the mass density; whereas, simulation of the HEI instability additionally requires evolving the phase-space density of several groups of energetic electrons, each having different values of the magnetic moment, μ. Finite-difference approximations to the model equations are integrated using the numerical methods introduced by Zalesak[75, 76] and following an implementation demonstrated by Guzdar and co-authors.[23]

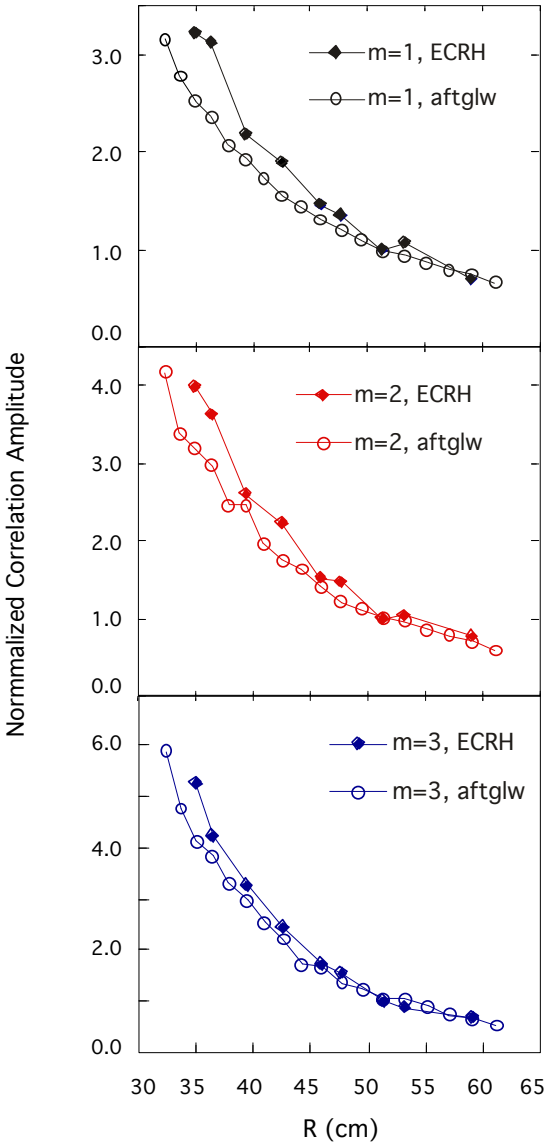

Figure 4.9: Normalized correlation amplitudes for the lowest three m numbers during the microwave heating compared with those during the afterglow.

4.4.1 Model Equations

The model equations are described in the coordinates of an ideal, axisymmetric dipole magnetic field. The potential, $\Phi(\psi, \varphi, t)$, is assumed constant along a field line, consistent with measurements and our understanding of interchange instability. The potential evolves in time due to the divergence of net perpendicular current integrated over magnetic flux tubes and subject to fixed boundary conditions. The divergence of perpendicular current either charges or discharges flux-tubes. Energetic electrons contribute to this current through the ∇B drift, and ions contribute through the polarization or inertial drift. In order to simplify the computation of energetic electron dynamics, the energetic electrons are assumed to be deeply-trapped with negligible motion along field lines, $J \sim 0$. A neutralizing population of cold electrons exists that is more uniformly distributed along the field line. Finally, to facilitate an efficient spectral solution for the potential, we define an axisymmetric dielectric, $\overline{\varepsilon}(\psi, t)$, proportional to the azimuthally-averaged ion number per flux tube, $\overline{N}_i(\psi, t) = \int d\varphi N_i / 2\pi$.

Using the notation in Ref. [44], the flux-tube average is defined as $\langle A \rangle \equiv \delta V^{-1} \int d\chi A / B^2$, where $\delta V(\psi) = \int d\chi / B^2$ is the volume of a flux-tube of given flux, $d\psi d\varphi$. The model equations describe only the dynamics of the total particles on a tube of unit flux, $N \equiv \langle n \rangle \delta V$, but the particle density, n, can vary along a field line. Since the magnetic field of the point-dipole is relatively simple to characterize, expressions for the field-line integrals can be computed after making reasonable assumptions of the field-line density profile.

Effectively, there are three coupled, nonlinear equations to be solved in the simulation. These are: the time evolution of the potential, $\delta V \langle \nabla \cdot \nabla \dot{\Phi} \rangle = -4\pi e \left(\dot{N}_i - \dot{N}_e \right) \equiv -4\pi e \Delta\rho$, the evolution of the ion number, $\dot{N}_i = -\delta V \langle \nabla \cdot n_i \mathbf{V}_i \rangle$, and the evolution of several populations of energetic electrons having different magnetic moments, $\langle \dot{n}_e \rangle \delta V \equiv \dot{N}_e = \sum_\mu \dot{F}_\mu(\psi, \varphi, t)$. To denote the time derivative, we use $\dot{A} \equiv \partial A / \partial t$. The rate of change of net charge on a flux tube due to the integrated divergence of the perpendicular current is $\Delta\rho$. In the expression for the electrons, F_μ is the number of electrons with a given μ on a given flux-tube. $F_\mu(\psi, \varphi, t)$ is a bounce-averaged phase-space density that evolves according to the guiding center drift Hamiltonian.[69]

The field-line integral of the ion current depends upon the density profile along the field-line. We call this integral the density-weighted average, defined as $\|A\| \equiv \langle An \rangle / \langle n \rangle =$

$N^{-1}\int d\chi n(\chi)A/B^2$. In this notation, the ion continuity equation is

$$\frac{\partial N_i}{\partial t}+\frac{\partial}{\partial\varphi}\left(N_i\|\nabla\varphi\cdot\mathbf{V}_i\|\right)+\frac{\partial}{\partial\psi}\left(N_i\|\nabla\psi\cdot\mathbf{V}_i\|\right)=0. \tag{4.4}$$

For cold ions and for low-frequency interchanges with $\omega\ll\omega_{ci}$, $\mathbf{V}_i$ is the sum of the $\mathbf{E}\times\mathbf{B}$ and polarization drifts. This substitution gives

$$\frac{\partial N_i}{\partial t}+\frac{\partial}{\partial\varphi}\left[cN_i\left(-\frac{\partial\Phi}{\partial\psi}-\left\|\frac{|\nabla\varphi|^2}{\omega_{ci}B}\right\|\frac{\partial\dot{\Phi}}{\partial\varphi}\right)\right]+\frac{\partial}{\partial\psi}\left[cN_i\left(\frac{\partial\Phi}{\partial\varphi}-\left\|\frac{|\nabla\psi|^2}{\omega_{ci}B}\right\|\frac{\partial\dot{\Phi}}{\partial\psi}\right)\right]=0. \tag{4.5}$$

The first term in parentheses is the $\mathbf{E}\times\mathbf{B}$ drift, and the second term is the polarization drift. This second term represents the plasma dielectric response, and the azimuthal average of this term will serve as the dielectric, $\bar{\varepsilon}$, when solving for $\dot{\Phi}$.

Since the field-line profile of the plasma density is not known, we invoke an important simplification in order to compute the density-weighted integrals. The density profile is assumed to be relatively broad and vary on all field lines as $n\propto\sin\theta$, where θ is the polar angle from the dipole's axis. For a point-dipole, the magnetic coordinate, χ, is related to the polar angle as $\chi=(\psi^2/M_0)\cos\theta/\sin^4\theta$. With this density profile, the density-weighted averages are $\||\nabla\varphi|^2/\omega_{ci}B\|\approx 0.66M_0^2B_0/\psi^4\omega_{ci0}$ and $\||\nabla\psi|^2/\omega_{ci}B\|\approx 0.77M_0^2B_0/\psi^2\omega_{ci0}$, where ω_{ci0} is the ion cyclotron frequency at $B=B_0$.

The field-line integrals of the Laplacian in the equation for the potential take a particularly simple form in dipole magnetic coordinates. The linear Poisson's equation becomes

$$h_\varphi\frac{\partial^2\Phi}{\partial\varphi^2}+h_\psi\frac{\partial^2\Phi}{\partial\psi^2}=-4\pi e\left(N_i-N_e\right)\equiv-4\pi e\rho, \tag{4.6}$$

where $\rho(\psi,\varphi,t)$ is the net charge on a field line. Two geometric terms define the transformation of the Laplacian operator into field-line averaged flux-coordinates: $h_\varphi\equiv\int d\chi/|\nabla\psi|^2=2M_0/\psi^2$ and $h_\psi\equiv\int d\chi/|\nabla\varphi|^2=4M_0$.

The electrons are grouped by magnetic moment, or effective energy μB_0, and separate evolution equations are needed for each energetic electron group. The collisionless guiding-center evolution of electrons with constant moment μ is governed by the following equation

$$\frac{\partial F_\mu}{\partial t}+\frac{\partial}{\partial\varphi}\left[\left(\omega_d(\mu,\psi)-c\frac{\partial\Phi}{\partial\psi}\right)F_\mu\right]+\frac{\partial}{\partial\psi}\left[c\frac{\partial\Phi}{\partial\varphi}F_\mu\right]=0. \tag{4.7}$$

Equations 4.5 and 4.7 and the time derivative of Equation 4.6 can be combined to form the equation used to evolve the electrostatic potential. This requires proper treatment of

the ion polarization currents. For our simulation, we desire to preserve the form of the Laplacian operator since this form can be inverted easily. We achieve this by defining an "axisymmetric" dielectric constant, $\overline{\varepsilon}$, in terms of the azimuthal average of the ion number, $\overline{N}_i$. The remaining non-axisymmetric part is defined as $\tilde{N}_i \equiv N_i - \overline{N}_i$. Using these definitions, the equation for the evolution of the potential used in the numerical simulation is:

$$h_\varphi \overline{\varepsilon}_\varphi(\psi,t)\frac{\partial^2 \dot{\Phi}}{\partial \varphi^2} + h_\psi \frac{\partial}{\partial \psi}\overline{\varepsilon}_\psi(\psi,t)\frac{\partial \dot{\Phi}}{\partial \psi} = -4\pi e \Delta\rho, \tag{4.8}$$

where divergence of the integrated perpendicular current is

$$\begin{aligned}\Delta\rho(\psi,\varphi,t) \equiv \frac{\partial}{\partial\varphi}\left(c\rho\frac{\partial\Phi}{\partial\psi} + c\tilde{N}_i\left\|\frac{|\nabla\varphi|^2}{\omega_{ci}B}\right\|\frac{\partial\dot{\Phi}}{\partial\varphi} + \sum_\mu \omega_d(\mu,\psi)F_\mu\right) \\ -\frac{\partial}{\partial\psi}\left(c\rho\frac{\partial\Phi}{\partial\varphi} - c\tilde{N}_i\left\|\frac{|\nabla\psi|^2}{\omega_{ci}B}\right\|\frac{\partial\dot{\Phi}}{\partial\psi}\right),\end{aligned} \tag{4.9}$$

and the time-dependent, axisymmetric dielectric functions are

$$\overline{\varepsilon}_\varphi(\psi,t) = 1 + 4\pi e c\frac{\overline{N}_i}{h_\varphi}\left\|\frac{|\nabla\varphi|^2}{\omega_{ci}B}\right\| \approx 0.3\frac{\langle\overline{\omega_{pi}^2}\rangle}{\omega_{ci}^2} \tag{4.10}$$

$$\overline{\varepsilon}_\psi(\psi,t) = 1 + 4\pi e c\frac{\overline{N}_i}{h_\psi}\left\|\frac{|\nabla\psi|^2}{\omega_{ci}B}\right\| \approx 0.18\frac{\langle\overline{\omega_{pi}^2}\rangle}{\omega_{ci}^2}. \tag{4.11}$$

In CTX, $\langle\overline{\omega_{pi}^2}\rangle/\omega_{ci}^2 \sim 10^3$ and scales with radius as $\propto \overline{N}_i/\psi^2$. Equation 4.8 requires the most computation to solve since, at each time-step, we iteratively invert the Laplacian operator on the left-hand-side (LHS) to arrive at improved approximations to $\dot{\Phi}$ which also appears on the right-hand-side (RHS).

Nonresonant dissipation of the electrostatic potential fluctuations is required for numerical stability, since little numerical dissipation results from the transport of ions and electrons. Explicit damping of the potential is added. Once a solution for $\dot{\Phi}$ has been found, the potential is advanced in time from t to $t + \Delta t$ according to,

$$\Phi(t+\Delta t) = \Phi(t) + \Delta t\dot{\Phi} - (-1)^k \Delta t \nu \nabla^{2k}\Phi(t), \tag{4.12}$$

where ν is a specified constant and $k = 0, 1, 2, ...$ sets the length scale for dissipation. For the simulation comparisons to be discussed in this chapter $k = 1$, though, as will be discussed in the next chapter, $k = 2$ damping was used to reproduce the rotationally driven mode structure.

4.4.2 Global Mode Structure Comparison

The numerical solutions exhibit many characteristics observed in the experiment.[44] For example, the HEI instability is destabilized only for a sufficiently large fraction of energetic electrons. The simulation also shows frequency chirping, multiple azimuthal modes, and strong modulation of energetic electron flux during nonlinear saturation. Figure 4.10 illustrates the time evolution of the electrostatic potential as computed by the simulation from initial conditions consistent with the experiment. The instability grows quickly to large amplitude, $e|\Phi| \sim 0.1\mu_0 B_0$, and develops a relatively complex, time-evolving frequency spectrum with $\dot{\omega}/\omega^2 \approx 0.09$. Azimuthal modes with $m = 1$, 2, and 3 can be detected easily, and the global structure of these modes can be "measured" by computing the Fourier transform of the simulated potential. In this subsection, the initial conditions for this solution are described, and the computed global mode structure is compared with measurements.

The initial potential fluctuations are set to randomly-phased, low-amplitude oscillations that vary sinusoidally in both the ψ and φ directions. The initial profiles of the ions and the energetic electrons are axisymmetric with an initial radial variation of the form $f(\psi, t = 0) \propto (\psi_{max} - \psi)^b (\psi - \psi_{min})^c$, where the parameter b is chosen to to insure $\partial f/\partial\psi = 0$ at $\psi = \psi_0$ and c is adjusted to change the steepness of the profile. For the energetic electrons, $c = 4$ and $b = 2.46$. For the ion number density, the initial profile was the sum of two equal parts: a constant and a gradual radial variation with $c = 1$ and $b = 0.62$. At the density peak, $R = R_0$, half of the electrons were energetic and half were cold.

The distribution of energetic electrons are modeled with five energy groups, $F(\mu, \psi, \varphi) = \alpha(\psi) \sum_{i=1}^{5} \beta(\mu = \mu_i)$, with $\mu_i/\mu_0 = 0.5$, 0.75, 1.0, 1.25, and 1.5. The initial radial profile, $\alpha(\psi)$ has the form described above, and the initial profile for each electron group is identical. The function $\beta(\mu) \propto (2\mu/\mu_0) \exp(-2\mu/mu_0)$ determines the relative number density of each of the five groups of energetic electrons. As the instability develops, resonant electrons are strongly mixed in radius; however, the total number of electrons with each value of magnetic moment is constant.

In Figure 4.10, the normalized dissipation rate was $\nu = 0.005$. For global modes, this causes a non-resonant damping of the order, $\partial \log \Phi/\partial t \sim 10^{-5}\omega_{d0} \ll \omega$. For broad, long-wavelength modes, this is a very small dissipation rate, but it nevertheless influences the

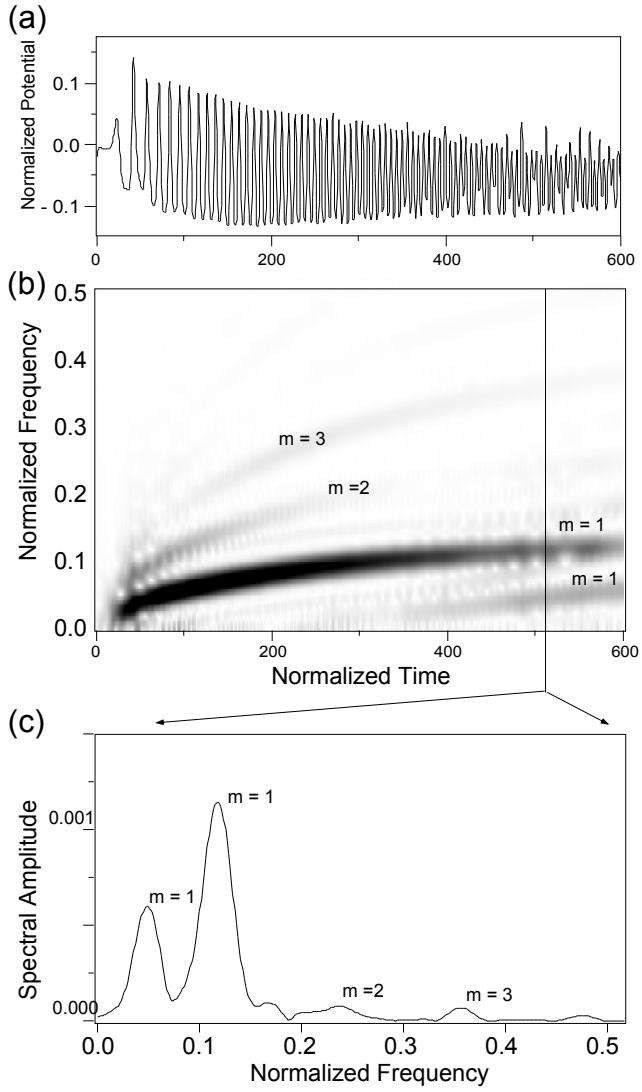

Figure 4.10: Self-consistent time evolution of the electrostatic potential computed using the nonlinear simulation. The TFD of the potential oscillations computed by the simulation show multiple modes and frequencies rising in time that resemble Figures 4.1 and 4.3. Time is normalized to ω_{dh0}^{-1}, and the potential is normalized to $\mu_0 B_0/e$.

solution significantly. If ν is decreased to 0.003, the frequency changes more slowly in time, $\dot{\omega}/\omega^2 \approx 0.07$. If ν is increased to 0.01, the frequency "chirps" more rapidly, $\dot{\omega}/\omega^2 \approx 0.2$.

The global structures of the modes simulated numerically are viewed by performing Fourier transforms of the computed potential, $\Phi(\psi, \varphi)$. The relative radial variations of the amplitude and phase of an azimuthal mode, $\Phi_m(\psi)$, can be compared directly with experimental measurements.

When this comparison was first made, we noticed a sensitivity to the location of the outer boundary, $\psi = \psi_{min}$, where Φ is forced to vanish. When ψ_{min} was set to correspond to inner radius of the vacuum vessel, $R = 67$ cm and $\psi_{min}/\psi_0 = 0.4$, the computed mode structures were more peaked than seen experimentally. As the outer boundary was moved to larger radii, the global modes in the simulation broadened. Several simulations were computed as the outer boundary gradually increased to $R = 98$ cm, or $\psi_{min}/\psi_0 = 0.27$. From these we were able to identify the outer location that minimized the magnitude of the difference between the simulated and measured mode structures for the lowest three modes, $m = 1$, 2, and 3. This occurred when $R_{max} = 77$ cm, or $\psi_{min}/\psi_0 = 0.35$. If only one mode (instead of three) was compared, the optimal location for the outer boundary was different. The $m = 1$ mode optimized at larger R_{max} while $m = 3$ optimized at slightly smaller R_{max}.

While we are not certain of the reason why a larger diameter for the outer boundary is required for the simulation to match the experiment's mode structures, we believe it results from the large geometric difference between the cylindrical vacuum vessel and the dipole's field lines. As shown in Figure 3.2, the field-lines are tangent to the vacuum vessel at $R = 67$ cm. This limits the extent of energetic electrons, but not the colder plasma. As a Langmuir probe is moved outward, beyond the last flux tube not obstructed by the vessel, the plasma density drops abruptly by more than a factor of two, but this does not eliminate HEI potential fluctuations. Obviously, the experimental boundaries are much more complex than simulated, and it is perhaps not surprising that some adjustment is required to match these conditions.

The computed nonlinear global mode structures are shown in Figures 4.5 and 4.11 when the outer boundary was set to $R_{max} = 77$ cm. Radial profiles of the radial phase difference, $k_R \Delta R$, generated from the simulation for $m = 1$, 2, and 3 are shown as solid lines in Figure 4.5 (and superimposed onto the experimental data.) The computed phase difference with radius

is small. As in the experiment $k_R \sim 0$. Figure 4.11 compares the radial variation of the mode amplitudes with the observed normalized correlation amplitudes (which are also shown in Figure 4.6). As seen experimentally, the ratios of the mode amplitudes evolve in time, but the form of radial structures are essentially constant once the amplitude saturates. In Figure 4.11, the computed mode amplitudes were normalized to minimize the least squares difference between simulation and experiment. The profiles are peaked near the peak of the energetic electron density at $R_0 = 27$ cm. Modes with higher m are more centrally peaked than modes with lower m.

Poisson Equation

The model equations give insight into the electrostatic potential structures of different azimuthal modes. If the net oscillating charge on the flux tubes, ρ, were non-zero only near the peak density of the energetic electrons (*eg.* $R \approx 27$ cm), then Equation 4.8 can be used to solve for the radial mode structure by separation of variables. Let $\Delta\rho \to 0$ except for a narrow region near $\psi \approx \psi_0$, and let the potential have the form $\Phi(\psi, \varphi, t) = g(\psi)\ \exp[-i(\omega t - m\varphi)]$. If we further take $\overline{N}_i$ to be a constant in order to simplify the form of the plasma dielectric (Equations 4.10 and 4.11), then the radial structure function, $g(\psi)$, must satisfy the equation

$$\psi^4 \frac{\partial}{\partial \psi}\left(\frac{1}{\psi^2}\frac{\partial g_m}{\partial \psi}\right) - 0.83 m^2 g_m = 0. \tag{4.13}$$

With the vacuum vessel wall at infinity, the outer solutions have a simple form $g_m \sim \psi^a \sim 1/R^a$ where $a = 3/2 + \sqrt{9/4 + 0.833m^2}$. The lowest three azimuthal modes are $g_1 \sim 1/R^{3.3}$, $g_2 \sim 1/R^{3.9}$, and $g_3 \sim 1/R^{4.6}$. These expressions are reasonably close to the radial dependencies shown in Figures 4.6 and 4.11, although the actual mode structures are less peaked. The profiles given by Equation 4.13 are plotted in Figure 4.11 as the solid blue lines. Equation 4.13 also offers a simple and perhaps general explanation of our key results. Indeed, during the simulation, $\rho(\psi, \varphi, t)$ is monitored, and the largest oscillations of ρ do occur near the peak of the energetic electrons.

The inner structures of the global modes could not be measured. As probes moved inward, the intensity of the artificial radiation belt was significantly perturbed. For this reason, we are unable to make any conclusions pertaining to the inner boundary condition

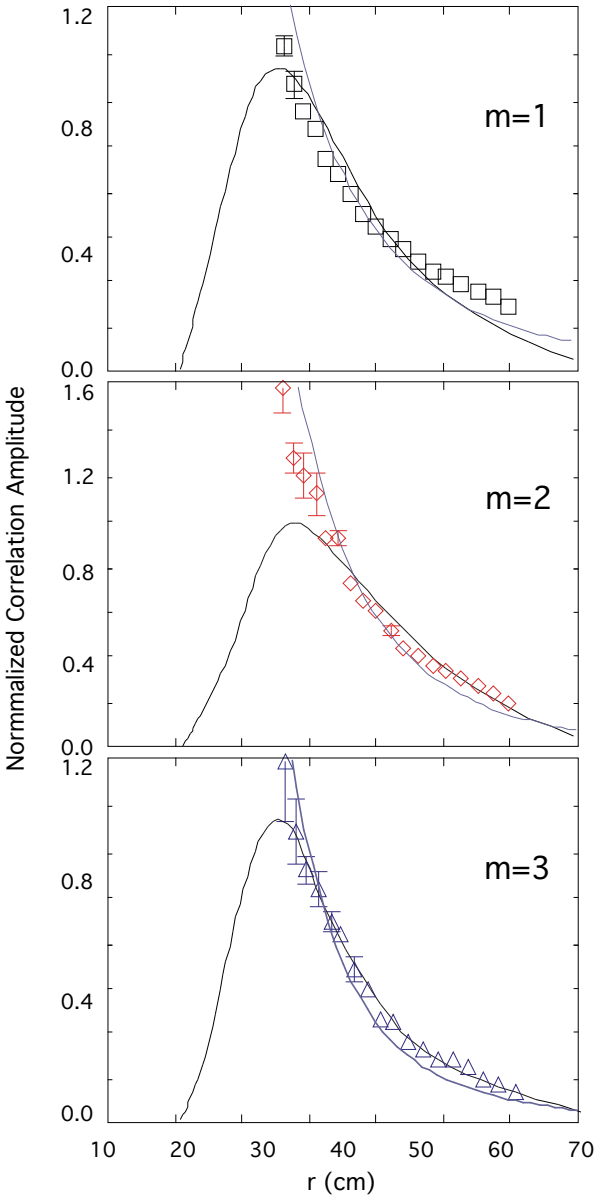

Figure 4.11: Comparison of radial mode structure computed from the nonlinear simulation (solid lines) with the observed profiles of the normalized correlation amplitudes for $m = 1$, 2, and 3 as well as the solutions to Equation 4.13.

at the surface of the dipole magnetic nor the mode structures near and within the radius of peak energetic electron density.

4.5 Summary

The global mode structure of low frequency interchange instabilities driven by energetic electrons was measured using time-frequency-domain analysis of the correlations between multiple high-impedance probes. A modal prescription was used to simplify the correlation analysis of movable high impedance floating potential probes. By positioning the probes appropriately, the HEI instability was seen to be flute-like with $k_{\|} \sim 0$ with multiple azimuthal modes peaked in amplitude near the peak density of energetic electrons. The modes have a time-evolving frequency spectrum, but the form of the global mode structure does not change significantly in time. The radial mode structures are relatively broad, and they rotate rigidly with $k_R \approx 0$.

A nonlinear, self-consistent numerical simulation of the growth and saturation of the HEI instability reproduces many observations from the experiment including the radial structures of the lowest azimuthal modes. The agreement between the modes computed by the simulation and the experimental measurements supports the underlying assumptions of the model equations and the resonant phase-space dynamics reported previously.[44]

Although general characteristics of the numerical solutions to the model equation resemble experimental measurements, several observations of the HEI instability in the experiment are not modeled nor do we fully understand how to do so. During microwave heating, the quasiperiodic bursts of instability have a more complex frequency spectrum than seen computationally. Experimentally, a period of rising coherent modes occurs after a short period when the frequency spectrum is relatively broad-band and turbulent. Broad-band fluctuations have not been seen computationally. Perhaps, most significantly, the mode structure of the HEI is sensitive to the experimental boundary conditions, and observations of the fluctuations near and within the region of energetic electrons has been so far impossible.

Chapter 5

Centrifugally Driven Instabilities in CTX

This chapter presents observational evidence of the rotationally driven interchange mode, excited in the CTX device using external radial electric fields to set up azimuthal $\mathbf{E}\times\mathbf{B}$ flows within the plasma. In the process, the bulk plasma response to the applied fields is discussed, as well as a basic model explaining the mechanism of how the electric field is established and the flows that result from it. The mode itself is described through an identical correlation analysis as was carried out for the HEI instability in Chapter 4, and is also compared with results from the same nonlinear code.

5.1 E × B Flows in CTX

5.1.1 Plasma Response to External Bias

In this section we describe the response of the equilibrium plasma to the external bias of the equatorial tungsten mesh array. The main diagnostics employed are local probe measurements, both biased and floating, as well as the voltage and current monitors of the bias power supply itself.

Parameters as a function of bias In Figure 5.1 we show a comparison of two typical shots, one without the external bias (shown in black) and one with the bias (red). The

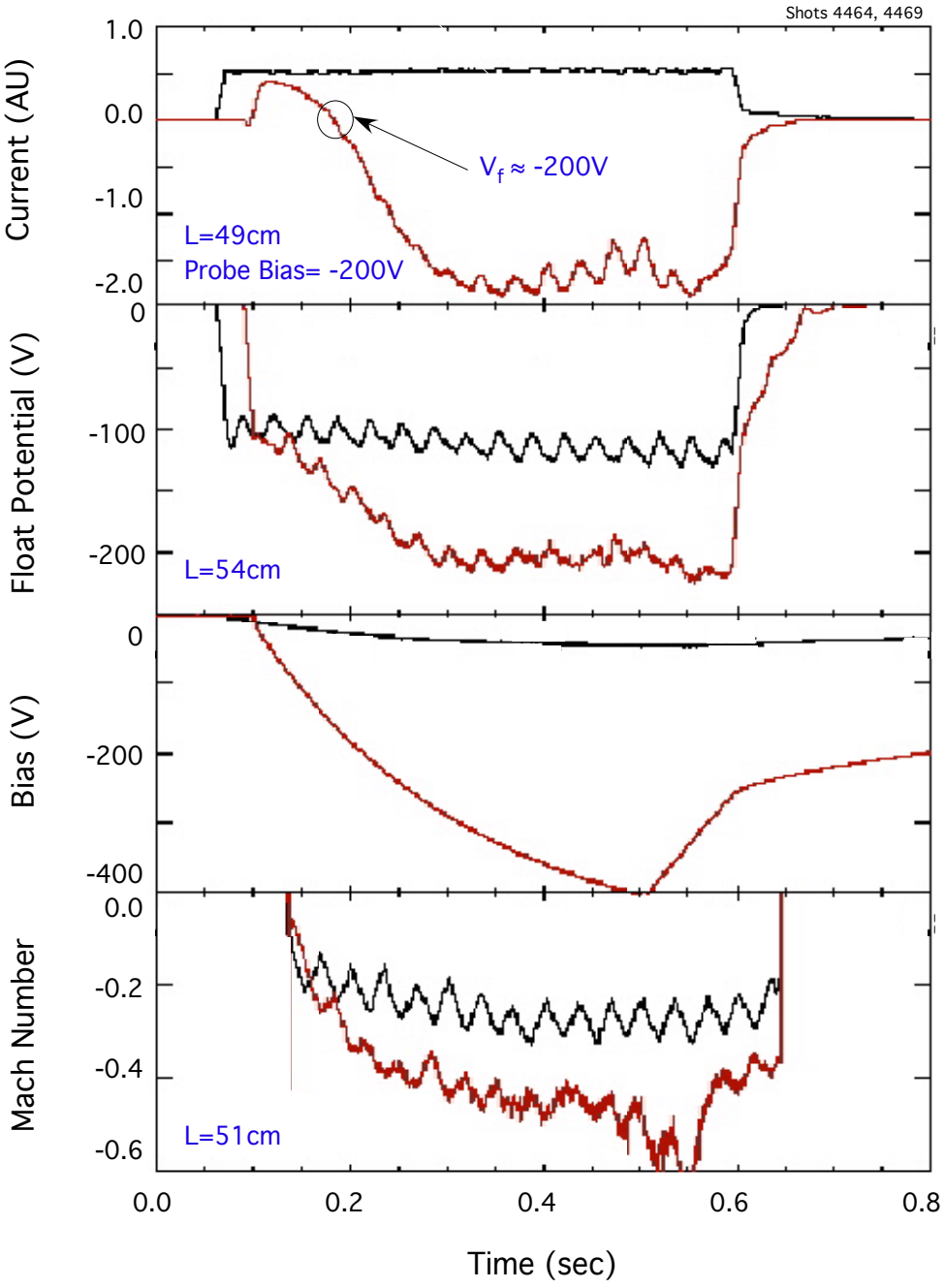

Figure 5.1: An example of the effect of the external bias on various plasma parameters. Black is without bias and red is with bias.

plot shows, from top to bottom, the current from a Langmuir probe biased at −200 V, a floating potential probe, the actual bias on the filaments, and the Mach number from the Mach probe. The equatorial radius of each probe is noted. Without the bias, we see roughly constant plasma density, potential and flow. In contrast, as the bias is ramped up, the floating potential of the plasma strongly increases negatively, coincident with an increase in flow. In the case shown, a peak floating potential of −200V is observed. It is not as immediately clear what the effect is on density, since the increase in floating potential causes the current of the Langmuir probe to change signs, taking it out of ion saturation regime. We point out that since the Langmuir probe is biased at −200 V, the plasma has a floating potential of this value at the point when the probe signal goes through zero(this is pointed out in the Figure), and then as the Langmuir signal continues to grow negatively, the floating potential as well increases below −200V at the location of this probe. Thus, the Langmuir probe ceases to become an accurate measure of density in this regime. The Mach probe indicates a strong flow induced by the bias; with application of external biases up to −500 and −600 V, higher flows of $M \sim 1$ are typical.

The slow regular oscillations seen in most probe measurements is in fact a 30 Hz oscillation from the main electromagnet power supply, which causes a current ripple and is not related to any plasma instability.

Parameters as a function of position Since all our measurements are local, radial probe scans are necessary to look at global effects of the bias. Most important is the radial scan of the floating potential, since it gives the induced electric field via, $\mathbf{E} = -\nabla V_f$. Figure 5.2 presents the floating potential profile with and without the application of the external bias. The large increase of the floating potential due to the external bias is evident, although near 50cm the presence of the material probe begins to limit the plasma, and the floating potential measurement tops out near −200V. Near 25cm, the inner boundary condition of the bias on the tungsten meshes is plotted and a dotted line interpolates the continuation of the increase in floating potential up to that value, which is unaccessible to the probes. Similarly, for the unbiased case the grounded inner boundary condition is plotted with its own interpolated profile.

The radial electric field, rotation velocity and rotation frequency interpolated from Fig-

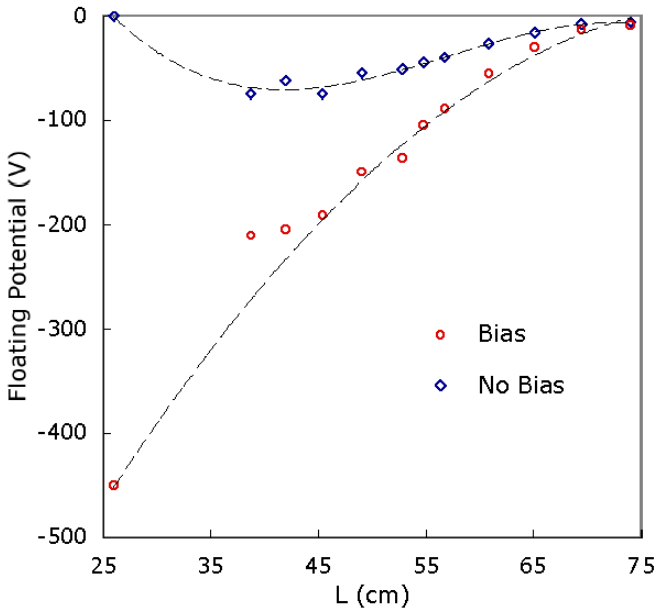

Figure 5.2: Radial scan of the floating potential with and without the presence of the external bias.

ure 5.2 are presented in Figure 5.3. We use only the non-limited points from Figure 5.2 in these calculations. The potential fits a $1/r$ profile, giving a $1/r^2$ electric field, a linear velocity profile and a constant frequency, ie. rigid body rotation. These results will be matched closely with both experimental observation from fluctuations propagating in the $\mathbf{E}\times\mathbf{B}$ frame in the next section and from equilibrium calculations in Section 5.3.

Figure 5.4 shows the Langmuir probe profile measured on the equatorial plane. Although the bias does cause the sign of the current drawn by the Langmuir probe to switch sign, as seen in Figure 5.1, it is possible to still measure ion saturation current at certain outer locations within the plasma. Ion saturation current is shown normalized between one moving Langmuir probe and one stationary probe. Ion saturation current is related linearly to density through the relation $I_{isat} \approx 0.61 e N_0 A \sqrt{T_e/m_i}$, where A is the surface area of the probe, N_0 is the unperturbed plasma density, T_e is the electron temperature, m_i is the ion mass and e is the elementary charge. Profiles of I_{isat} are compared in the presence of the external bias and without, and show overlapping profiles. We also plot the marginally stable density profile for interchange instabilities in a dipole geometry, which will be discussed in the next chapter,

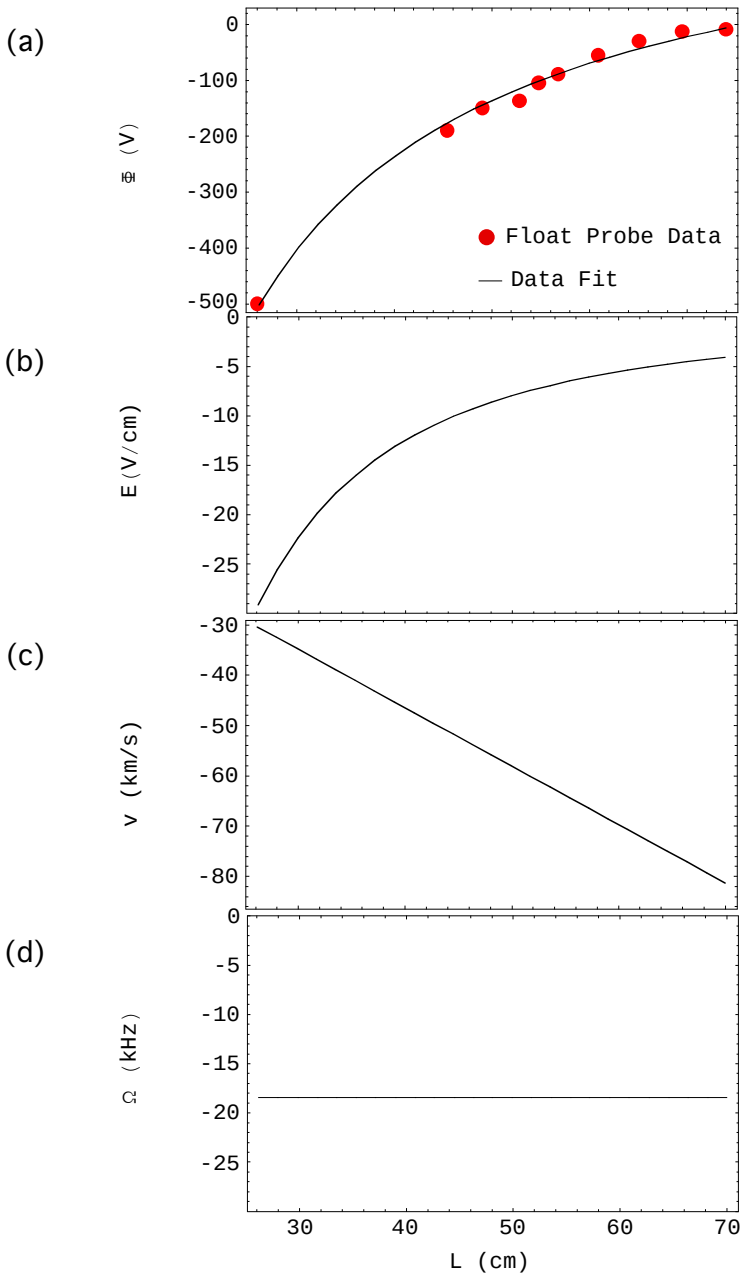

Figure 5.3: (a) Interpolated floating potential from the red data points; (b) radial electric field calculated from (a); (c) the azimuthal rotation velocity, and (d) the $\mathbf{E} \times \mathbf{B}$ frequency.

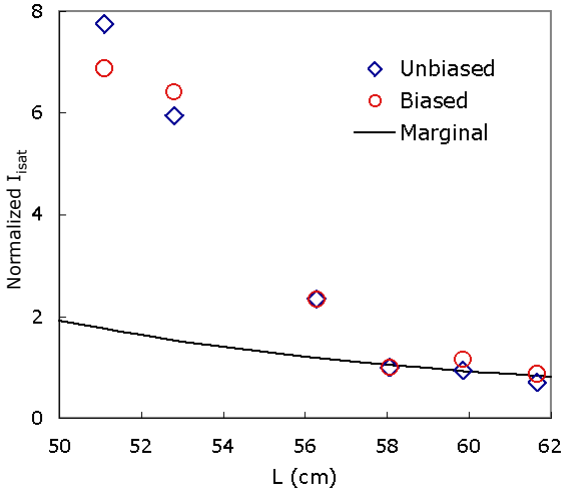

Figure 5.4: Normalized ion saturation radial profile between one movable Langmuir probe and one stationary probe for the biased and unbiased case. The solid black lines show the marginally stable profile from interchange linear theory, $n \propto r^{-4}$.

simply to demonstrate that the measured profiles are sufficiently steep to drive interchanges. In fact, the profile appears much steeper at this location. Due to the T_e dependence it is impossible to know the profile exactly without doing full Langmuir characteristics at each probe location.

To monitor the density profile closer to the core of the plasma, soft x-ray measurements were taken, since material probes destructively interfere with the plasma. An array of three diodes focused on the inner, central and outer plasma regions respectively, measure a flattening of the density profile at the inner plasma region in the presence of the bias relative to the case without the bias. This observation is shown in Figure 5.5, and is also consistent with interchange motion, which should cause diffusion of hot inner plasma and, therefore, density profile flattening. The probe measurements in Figure 5.4 don't show this since they are near the plasma edge, where the soft x-ray signal also shows no change in the density with bias.

The power provided in spinning up the plasma is measured from the voltage and current monitors on the DC bias power supply. The dependence of supplied power on external bias

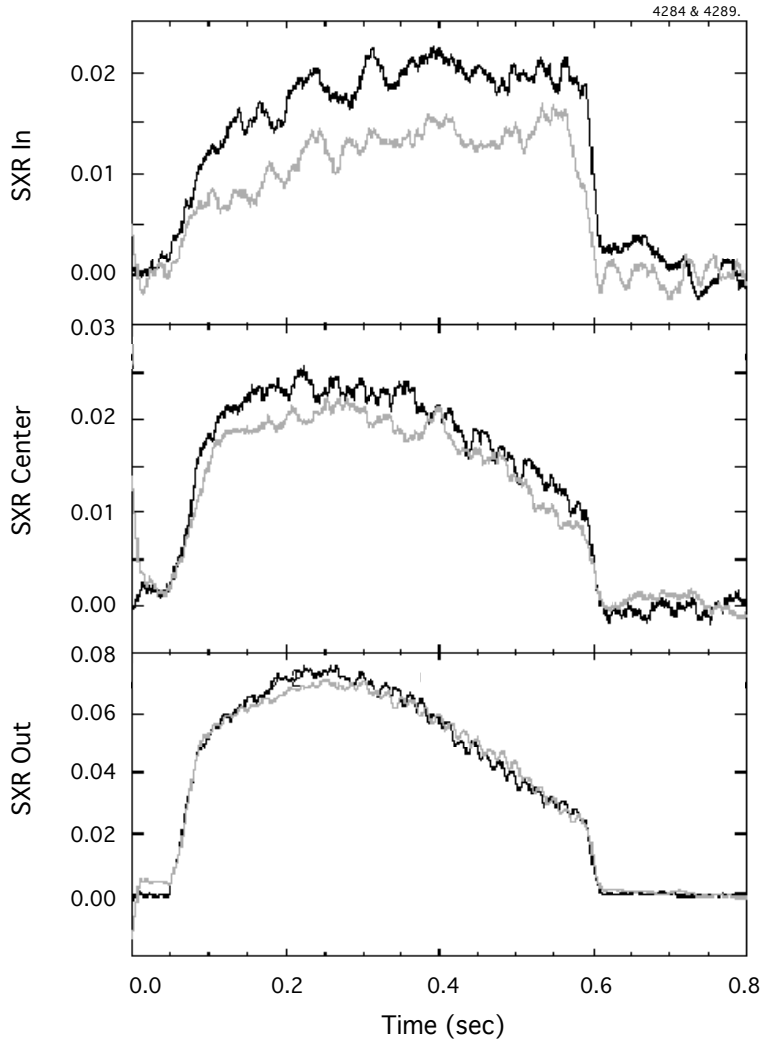

Figure 5.5: Soft x-ray measurements from inner, central and outer plasma regions, with (grey) and without (black) the external bias.

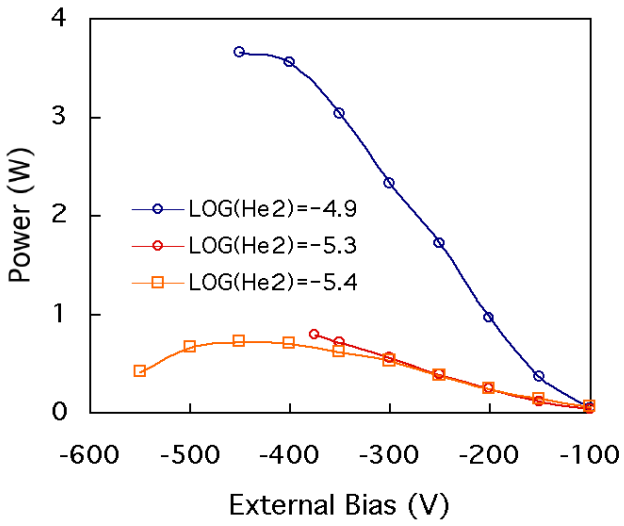

..

Figure 5.6: Power provided by the bias power supply as a function of external bias for different values of background neutral fill pressure.

is shown in Figure 5.6. Plots for several different values of background neutral fill pressure are given as well. Clearly, higher power is required to spin up a denser plasma. Also of note is the observation that the power peaks at a given value of bias, and then drops thereafter. This is at a point in a shot when the plasma is already spinning rapidly and, presumably, less current is required to drive the rotation.

5.2 Observation of Centrifugally Driven Interchange Instability

After having described the effect of the external bias on equilibrium plasma parameters, including the observation of a large radial electric field and rapid azimuthal plasma rotation, we now discuss the effect on plasma fluctuations, and identity the centrifugally driven interchange instability.

The time-frequency domain (TFD), or spectrogram, of the fluctuations, are plotted, as measured by a fast, floating potential probe with a sampling rate of 200 kHz in Figure 5.7. Coincident with the application of the bias, the increase in the DC floating potential of the

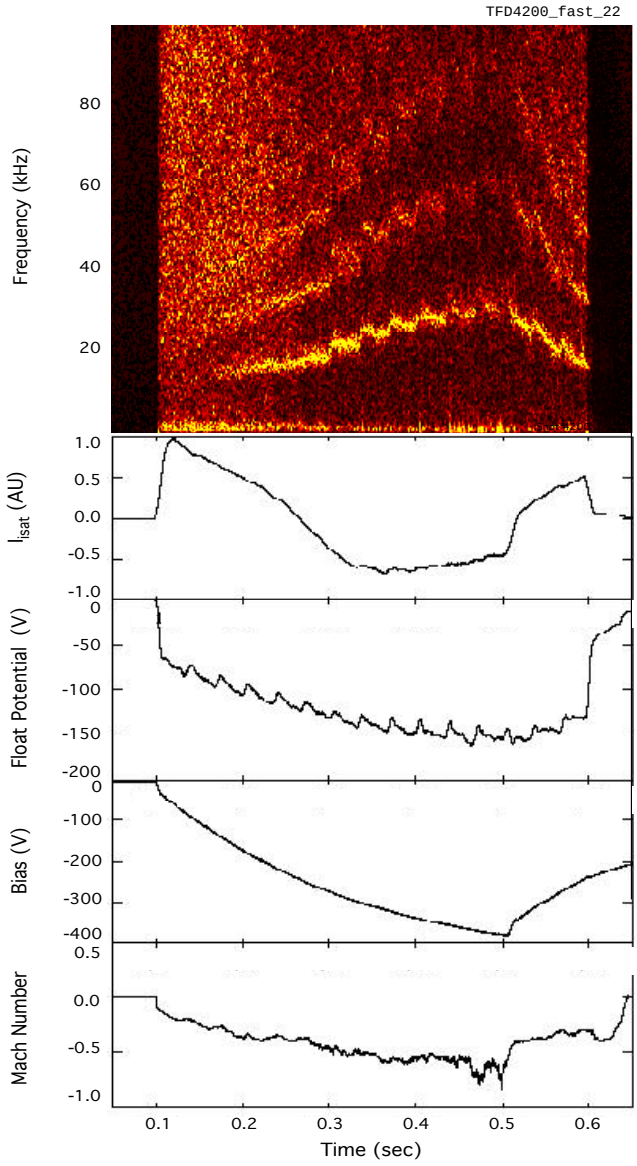

..

Figure 5.7: Effect of external bias on bulk plasma parameters and excitation of electrostatic fluctuations .

plasma and the spinning up of the plasma, are seen fluctuations whose frequency increases with the bias on the tungsten array. At the particular location of the floating potential probe ($L \sim 60$cm on Figure 5.2), the potential increases threefold, from -50V to -150V. The lowest frequency mode, at roughly 25kHz, is the largest amplitude mode, with smaller modes existing at frequencies of integer multiples of the fundamental. Thus, a single non-sinusoidal mode is observed with smaller amplitude higher harmonics. These frequencies are consistent with the $\mathbf{E} \times \mathbf{B}$ frequency calculated from the measured electric field and the supplied dipole field given in Figure 5.3. Probe scans across the plasma volume also indicate that the mode is rigidly rotating with a constant angular frequency, also consistent with Figure 5.3.

Figure 5.8 shows a similar but more detailed plot, but of a shot where the power to the magnetic field is at 70% of its peak value. Here, the floating potential fluctuations have been sampled at 1MHz and the waveform in the time-domain in shown. One can differentiate between two different regions in the TFD: an early low-bias region where the low frequency mode is dominant, and a later higher bias region where a higher frequency - roughly 100 kHz - mode becomes dominant. The waveform of the fluctuations is blown up in these regions in Figures 5.8(b) and (c). The slightly triangular non-sinusoidal waveforms from two probes separated by 90° azimuthally are shown for each case. The direction of propagation can be obtained from the phase difference between the probes and confirms that the mode moves in the $\mathbf{E} \times \mathbf{B}$ direction. The correlation analysis, which is described below, identifies the azimuthal mode structure and identifies the low bias (early) region as being $m = 1$ dominated and the higher bias (later) region as being $m = 2$ dominated. This result is shown in the amplitude spectra - also shown in the Figure - and will be explained by linear theory of interchange instabilities driven by both pressure and centrifugal forces, also discussed below.

The amplitude of the $m = 1$ and 2 modes in the two different regions is plotted in Figure 5.9 versus bias, and clearly shows the dominant domains for the lowest two azimuthal modes.

We also note that the mode amplitude grows with higher background fill pressure. This is consistent if the instability is mass-driven (as discussed below, HEI, on the other hand, is stabilized in high density plasmas). This dependence is shown in Figure 5.10 for two different values of external bias. We note that the amplitude decreases from the lower bias case to the

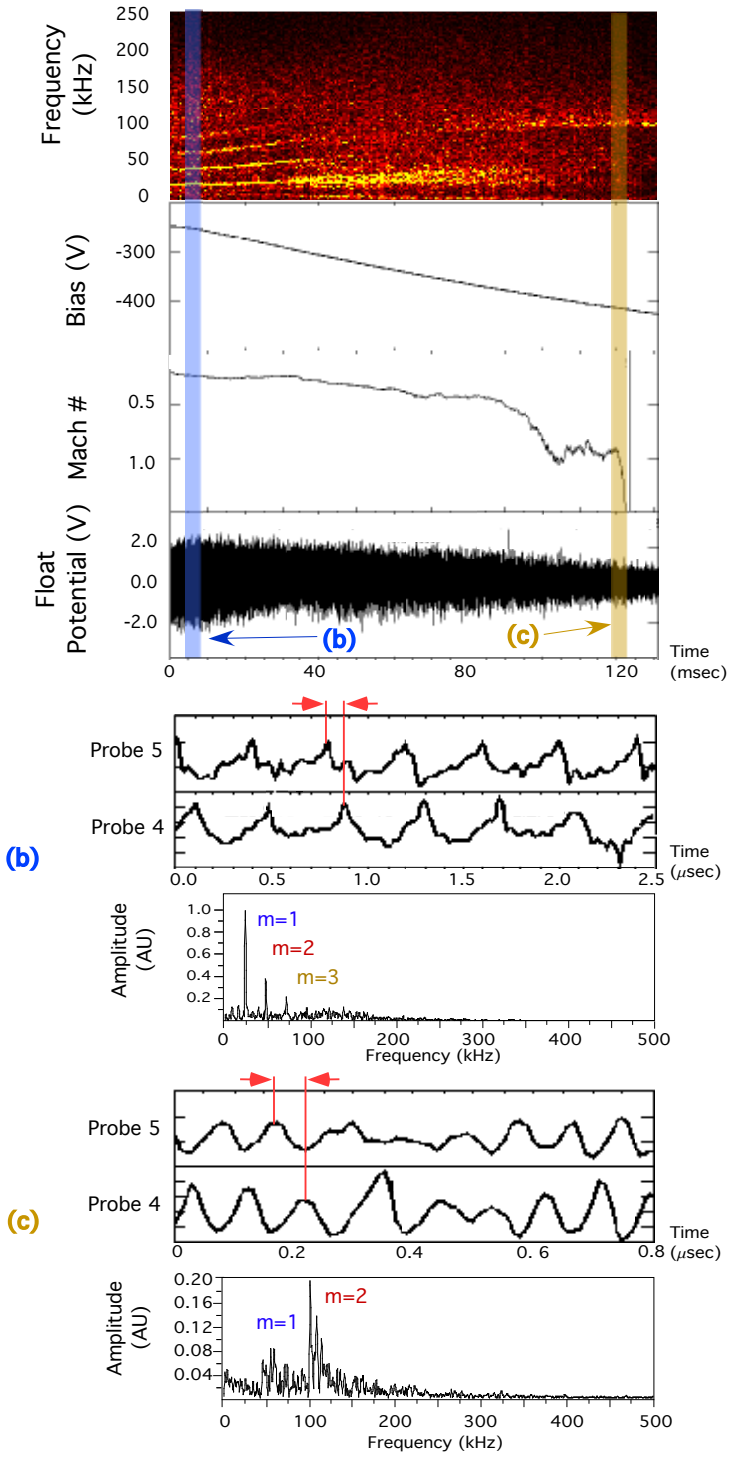

..

Figure 5.8: (a) The effect of a reduced B field on bulk plasma parameters and electrostatic fluctuations: increased rotation speed and the excitation of an $m = 2$ mode is observed. (b) The amplitude spectra of the fluctuations are dominated by $m = 1$ in the slower regime, and (c) by a $m = 2$ in the faster regime.

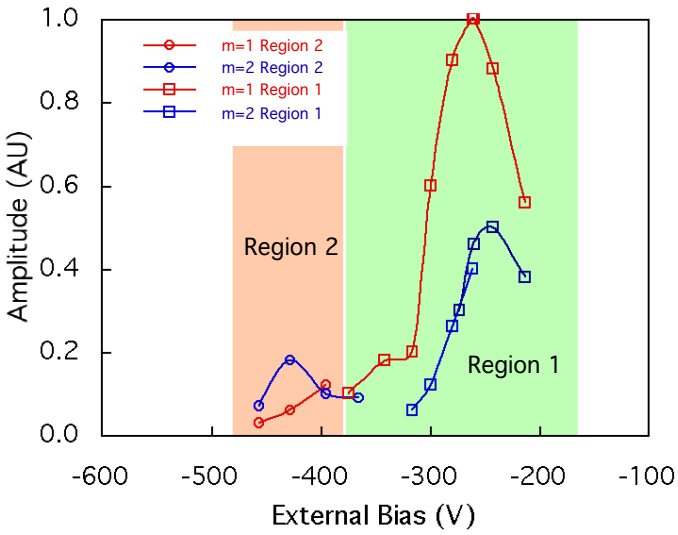

..

Figure 5.9: $m = 1$ and 2 mode amplitude as a function of external bias. We call the region where $m = 1$ dominates Region 1 and where $m = 2$ dominates Region 2.

higher bias case for the same value of fill pressure simply because these biases are located on the high bias side of Figure 5.9, where higher bias corresponds to lower amplitude.

We also plot the $m = 1$ mode frequency as a function of external bias in Figure 5.11. In general the mode frequency increases with bias, as is clear from the TFD in Figure 5.7 or 5.8. In addition, the frequency is plotted for two different values of the magnetic field (keeping the bias fixed), and shows an increase in frequency when the B field is lowered. This is consistent with the $\mathbf{E} \times \mathbf{B}$ frequency, which goes as E/rB, where r is the radius. The case where the mode shifts into the second region which is $m = 2$ dominated is also plotted.

Distinctions from HEI

At this point it is worth reiterating the differences between the spectrograms shown in Figures 5.7 and 5.8 of the rotation induced mode and Figure 4.3 in Chapter 4 showing the HEI instabilities. The frequencies of the fluctuations are on vastly different time-scales: HEI is drift-resonant, $f_{HEI} \sim m\omega_d/2\pi \approx 1 - 5$MHz, while the rotation induced mode is two orders of magnitude slower, at $f_{rot} \sim m\omega_{\mathbf{E}\times\mathbf{B}}/2\pi \approx 25 - 100$kHz.

Another point of comparison is the physical mechanism leading to the observed increases

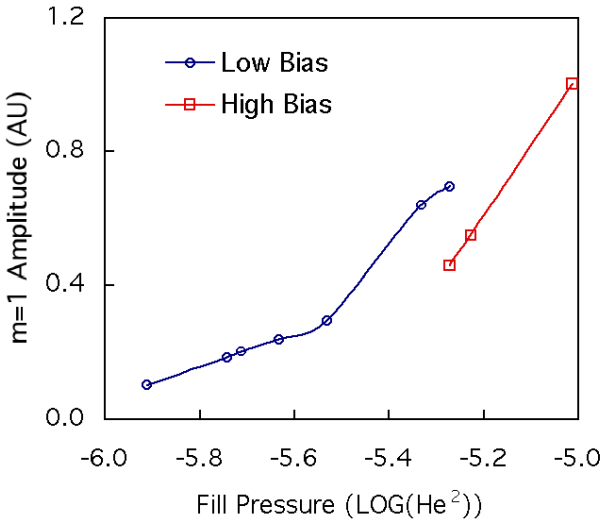

..

Figure 5.10: $m = 1$ mode amplitude as a function of background neutral helium gas fill pressure for two different external bias settings.

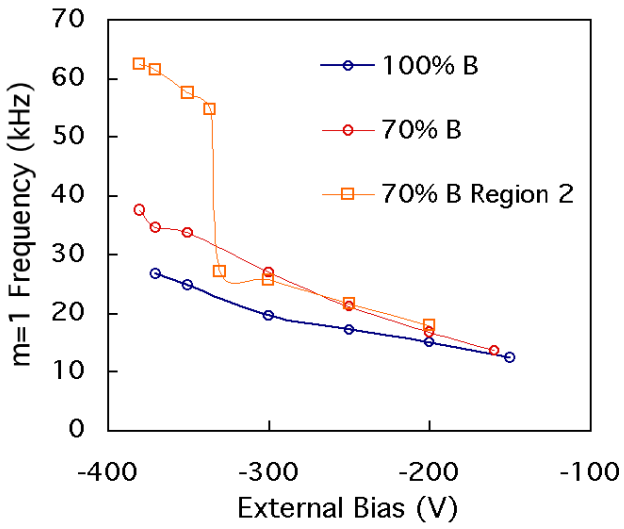

..

Figure 5.11: $m = 1$ mode frequency as a function of external bias for two different values of magnetic field.

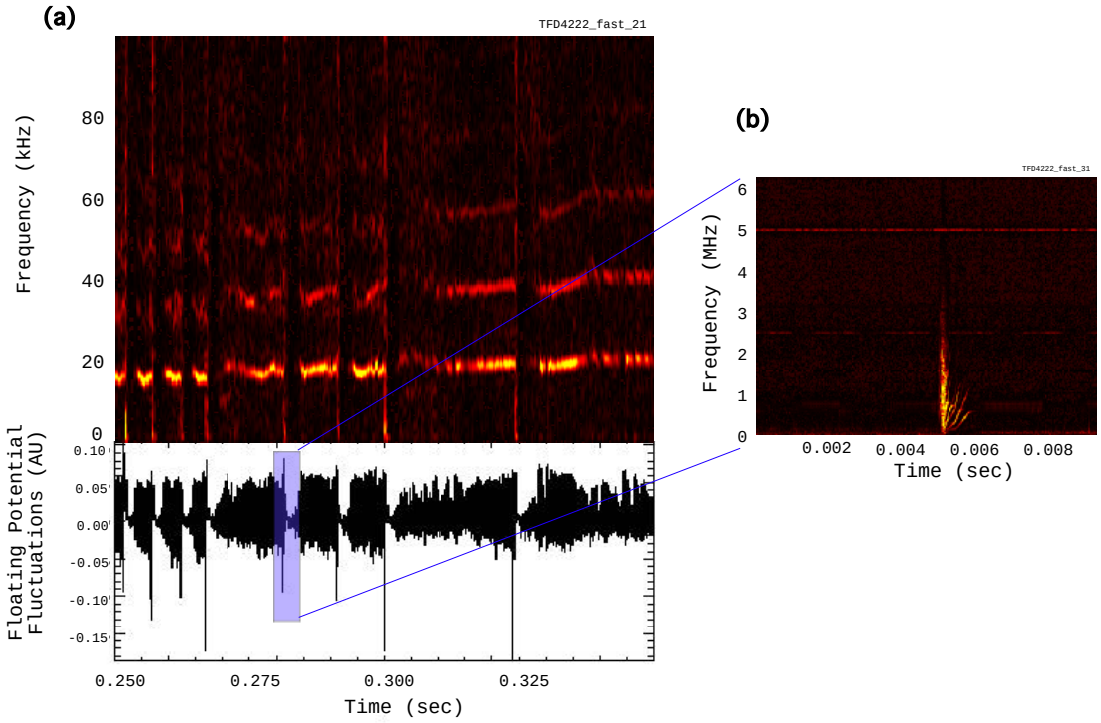

..

Figure 5.12: Simultaneous observation of HEI and rotational mode during a low density shot. (a) The floating potential fluctuations and their TFD are shown from one probe digitized at 200 kHz and, (b) another probe sampling at 1 MHz picks up the characteristic HEI fluctuations.

in frequency. For the rotational mode the increase is simply due to the increase of the bias on the tungsten mesh array, and therefore the electric field and the rotation. The HEI instability, on the other hand, displays nonlinear frequency sweeping, which results from the inward movement of phase-space holes being exchanged with outward moving hot, dense plasma [41, 40, 4]. In short, the former phenomena is driven, while the latter is spontaneous.

Having made the distinction clearer, we mention that both modes are observed in the same discharges. Figure 5.12 shows floating potential fluctuations for a low density shot (approximately an order of magnitude lower density than Figure 5.7 or 5.8) which display the effects of both modes. The rotational modes fluctuations are shown on the kHz time

scale in Figure 5.12(a), but appear to be arrested with a decreasing frequency coincident with spikes in the potential. The signal from another probe digitized in the MHz range with a low frequency filter is shown in Figure 5.12(b) and clearly shows these rapid modulations to be due to the HEI instability.

This regime has not been studied exhaustively, but the following interpretation is consistent with observations and our understanding of interchange dynamics, which we derive in detail in the next chapter. Both modes require steep gradients: HEI depending on hot electron gradients and the rotational instability on ion gradients. HEI bursts cause rapid interchange motion and flattening of density profiles. They are periodic since ECRH plasma production builds the density profile back up to its marginally unstable value in a characteristic time, driving HEI unstable again. In the presence of the rotational mode, a rapid flattening of the density due to HEI induced motion removes the rotational instability drive as well as that of the HEI. Thus we see no fluctuations at all in Figure 5.12(a) immediately following an HEI burst, followed by a slow buildup of the rotational mode fluctuations as plasma production steepens the density profile again, and then ultimately an HEI burst when its critical value is reached.

This interplay also goes in the other direction, ie. the rotational mode prevents the HEI from going unstable as well. This is manifested in the decreasing periodicity of the HEI bursts. Since the bias on the mesh array is increasing, the drive for the rotational mode is also increasing. In the presence of a more unstable rotational instability it requires longer for the hot electron profile to reach the critical gradient for HEI instability, since the former mode is also interchanging plasma, though in a constant, less dramatic fashion, shown in the soft x-ray measurements, Figure 5.5.

This complex interaction of plasma instabilities isn't seen at higher densities since the HEI saturates into broad-band incoherent fluctuations in this regime, where the plasma is denser and colder and less hot electrons exist. Most observations of the rotational mode were done in the high density regime since it has higher amplitude there as well as the fact that HEI bursts and energetic electrons make probe measurements extremely difficult on other bulk plasma phenomena.

5.2.1 Correlation Analysis

The same correlation analysis that was performed for the HEI instability is also presented here for the bias-induced fluctuations. In addition, modifications to the nonlinear particle simulation that was employed in comparisons to the HEI mode structure is used here as well to make comparison with the rotational instability mode structure.

When $\Delta\varphi = \Delta R = 0$ between two probes, only field-line information is retained. Correlation phases for such a measurement confirm the flute-like nature of the observed mode. That is, we confirm $k_{\|} \sim 0$.

The azimuthal mode number frequency spectrum shown in Figure 5.8(b) and (c) is obtained from the phase of the correlation function of two probes separated only in azimuthal angle, ie $\Delta R \sim \Delta s \sim 0$, and $\Delta\varphi = 90°$. As mentioned, the lowest frequency, largest amplitude mode in the low bias region is identified as the $m = 1$ mode, with higher harmonics of gradually decreasing amplitude, while the higher bias region is characterized by a large $m = 2$ mode.

The radial phase and amplitude for the three lowest azimuthal modes are shown in Figures 5.13 and 5.14. In Figure 5.13, the three lowest m numbers were examined at three different times in a single discharge but with each radial location representing averages of several shots having the movable probe at different positions. In Figure 5.13 (a) the m number is plotted versus radius. There is a nonzero radial phase, $k_r \neq 0$, for all modes, markedly different than the HEI modes. At roughly 55cm both probes are at the same location where there is zero radial phase difference. Thus, purely azimuthal structure is measured at this location. As one probe is moved off this location, the radial phase can be observed. A full $\pi/2$ radial phase shift is seen between 55cm and roughly 36cm for all three modes. We observe no apparent time dependence in the phase, as is shown in Figure 5.13 (b) for the $m = 1$ mode. This is true for all modes.

In Figure 5.14, the radial profile of the normalized magnitude of the two-probe correlation function shows the radial structure to be broad and to depend on the azimuthal mode number, with lower m modes being broader generally. In all cases, the mode structure extends from the edge to the inner hot electron region, and they are not localized to particular flux surfaces (probes can only go in as far as the ECRH resonance location, whereupon their

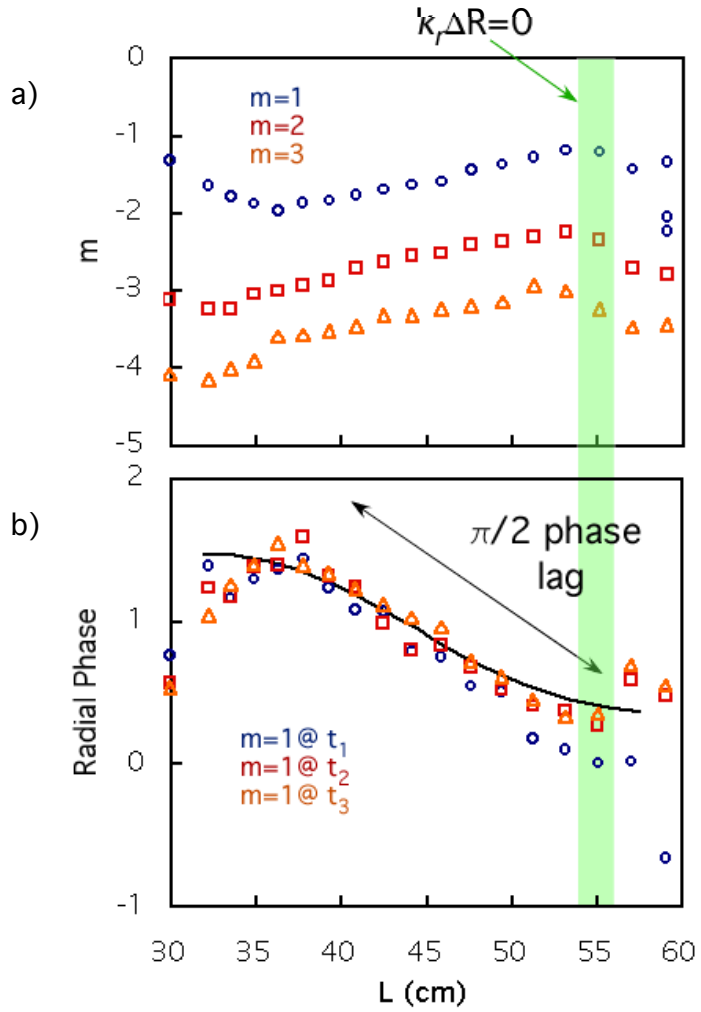

Figure 5.13: a) Phase of the correlation function between two probes as a function of the radial position of one probe for the three lowest m numbers. b) Radial phase of the $m = 1$ mode at three different times during a shot. Solid line is the simulation result for $m = 1$.

presence prevents plasma production). In addition, little time dependence is observed in these normalized profiles, although the relative amplitudes of one mode with another are observed to vary in time.

5.2.2 Comparison with Nonlinear Simulation

We have modified the nonlinear, self-consistent numerical simulation used to describe the HEI mode in order to interpret the observed rotational instabilities. To accomplish this, bulk rigid rotation was imposed, as is seen experimentally. Compared with the runs used to study the HEI instability, these runs were characterized by lower hot electron populations and higher plasma densities to stabilize the pressure driven modes to a degree, and steeper ion profiles, since that provides drive to the mass-driven rotational mode. In addition, a numerical damping of smaller wavelength modes was implemented: in Equation 4.12 we set $k = 2$. With these amendments, the simulation reproduces the observed modes.

The simulation produces a global mode dominated by low m numbers, characterized by dramatic ion mixing (Figure 5.16(b)) and a flattening of the ion density profile (Figure 5.16(a)), similar to Figure 5.5. The mixing starts off stationary with respect to the rotating frame of reference, but develops complex patterns, sometimes with the inner region rotating counter to the outer regions. With lower instability drive (lower rotation frequency) the electrostatic potential is dominated by an $m = 1$ structure (Figure 5.16(c)), but higher modes become dominant with increasing rotation frequency or steeper ion density gradient. However, even when a relatively strong drive is applied, the long-time saturated state of the instability often relaxes to an $m = 1$ structure, reflecting distinct behaviors in the linear and nonlinear saturated phases.

The saturated mode structure reproduces key characteristics of experimental observation; the radial profile of the normalized magnitude of the three lowest m modes is compared to measured results in Figure 5.14; comparison of the radial phase profile for $m = 1$ is shown in Figure 5.13 (b). In general, the simulation exhibits more time dependence in its solutions than experimental observations, which are of instabilities in a nonlinearly saturated state. To account for this, the mode structure comparisons were made with long-time runs of the simulation which were, themselves, saturated. As time proceeds the ion density profile

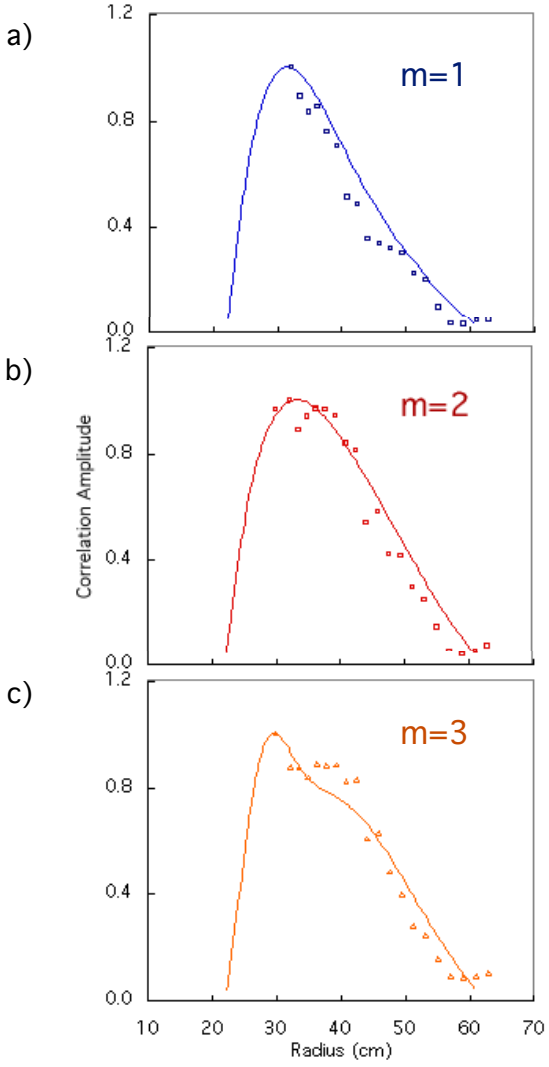

..

Figure 5.14: Normalized magnitude of the correlation function between two probes as a function of the radial position of one probe for the three lowest m numbers. Solid lines are simulation results.

flattens and the mixing slows. The corresponding electrostatic potential mode amplitude peaks at some intermediate time, beyond which it begins to decay very slowly.

With very small hot electron fractions the mode is purely growing in the rotating frame of reference. However, with the addition of larger energetic populations - which is the realistic case - HEI modes begin to go unstable and impart a real frequency to the modes within the $\mathbf{E} \times \mathbf{B}$ frame. This additional rotation is in the same direction as the original rotation since the electron ∇B drift is in the same direction as the $\mathbf{E} \times \mathbf{B}$ drift, thereby increasing the rotation. Very slow chirping can be seen, as in the pure HEI case. For one representative case, we estimate the additional frequency to be $\sim$ 7 kHz. Of course, experimentally it is difficult to differentiate between the sources of rotation, but this estimate is consistent with the frequency inferred from the measured electric field in Figure 5.3: we calculate approximately 19 kHz due to $\mathbf{E} \times \mathbf{B}$ rotation; if in fact the additional ∇B contribution is about 7 kHz, then the total of 26 kHz is consistent with the experimental observations.

This point is important to note, since the real frequency of the HEI instability induces polarization currents which are stabilizing. In Chapter 6 the linear dispersion analysis of the combined interchange mode will show that these stabilizing currents are necessary in order to reproduce the observation of unstable low m modes, since the polarization term is larger for higher m's. In this way, the addition of hot electrons to both the simulation and the linear stability analysis is critical, and is consistent with our observations, notably Figure 5.12. Specifically, we plot the mode amplitude for the four lowest m numbers for two values of hot electron fraction in Figure 5.15. For the 5% hot electron fraction case, the $m = 2$ mode is dominant in the linear growth phase of the simulated instability, while the $m = 1$ mode is always dominant in the 20% case. These results corroborate the experimental findings that a reduced hot electron fraction (the reduced B field case in Figure 5.8) allows the growth of an $m = 2$ mode.

5.2.3 Summary of Experimental and Simulation Results

We summarize the experimental observations relating to the biased experiments thus far, including equilibrium changes and fluctuation measurements.

- Floating potential measurements indicate that half of the potential difference between

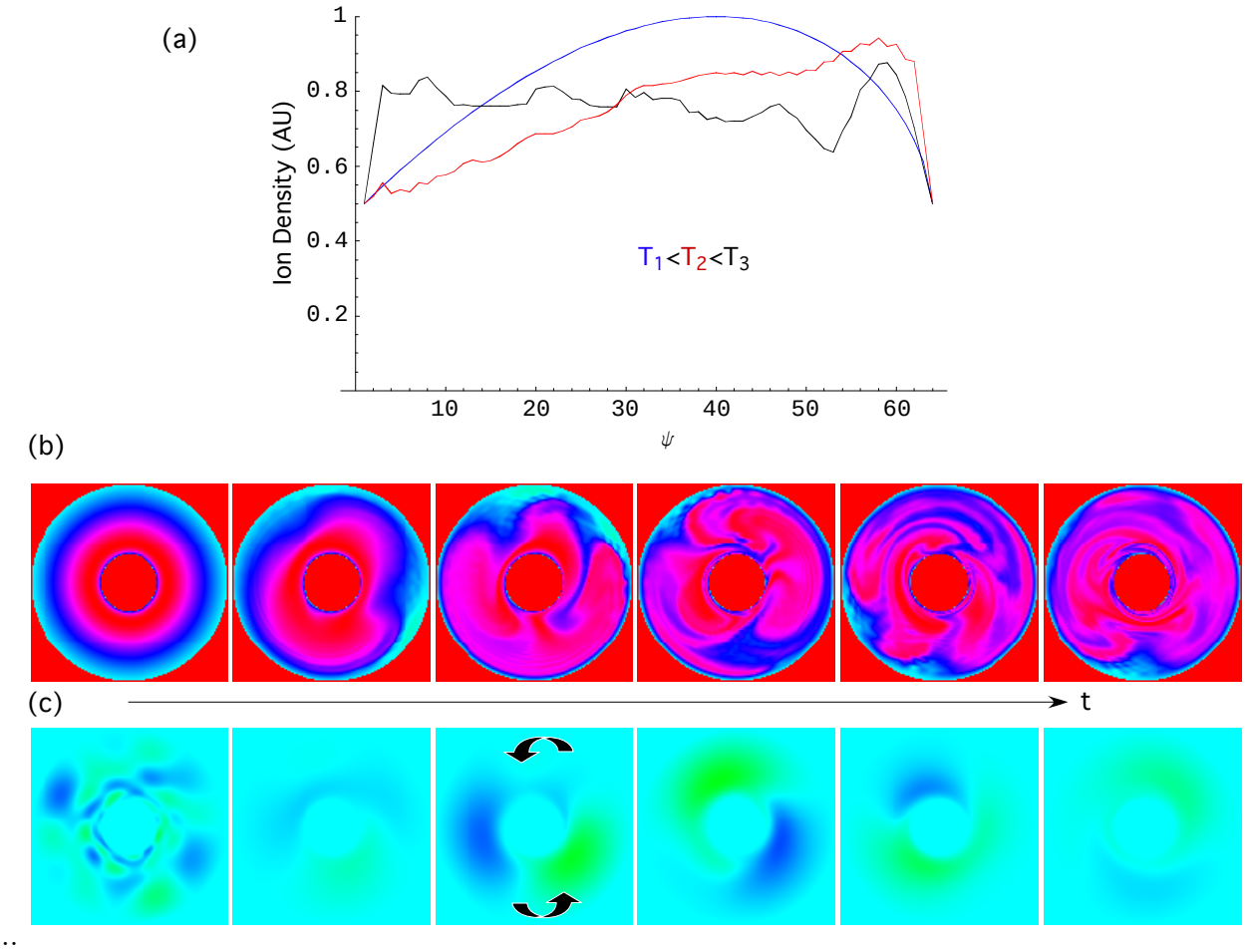

Figure 5.15: (a)The ion density profile as a function of flux ($\psi \propto 1/r$), for three different times. A flattening of the initial profile is apparent. (b) Equatorial contour plots of ion density. Time proceeds to the right. (c) Equatorial contour plots of electrostatic potential.

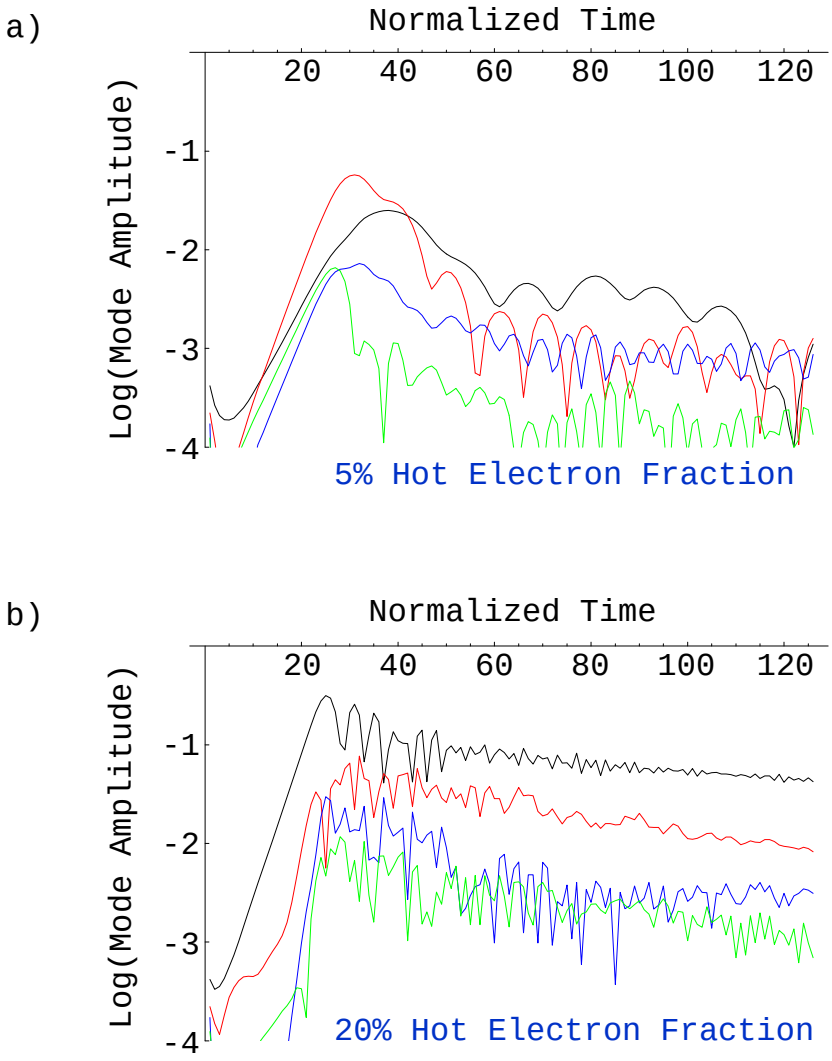

..

Figure 5.16: (a)The log of the mode amplitude for the four lowest m numbers for a hot electron fraction of 5%, and (b) 20 %.

the inner tungsten mesh array and the grounded outer chamber wall is dropped across the plasma volume which can be probed. We infer that the remaining potential difference is dropped across the region inaccessible by the floating potential probes.

- Electric fields of $10 - 30$ V/cm are induced across the volume.
- Subsequent $\mathbf{E} \times \mathbf{B}$ rotation of the plasma is observed with a Mach probe. Flows of $M \sim 1$ are typical. Flow increases with external bias.
- Langmuir probe measurements show density profiles which are steeper than L^{-4}, which is the marginal profile for interchange motion in a dipole.
- Soft x-ray measurements indicate a flattening of the density profile at the inner plasma when the bias is applied.
- Floating potential probe fluctuations indicate a non-sinusoidal oscillation whose frequency increases with the external bias, and is absent when the bias is not applied. The frequency is in the range of the $\mathbf{E} \times \mathbf{B}$ frequency. The mode is rigidly rotating, with constant angular frequency of roughly 25 kHz across the plasma volume.
- Comparisons from two probes indicate that the oscillation propagates in the $\mathbf{E} \times \mathbf{B}$ direction.
- Correlation analysis shows the fluctuation to be a flute mode, with $k_{\|} \sim 0$,
- The fluctuation mode amplitude increases with plasma density, suggesting that it is mass driven.
- Decreasing the magnetic field increases the frequency of the fluctuations, further suggesting that the mode is propagating in the $\mathbf{E} \times \mathbf{B}$ frame of reference.
- The global mode structure is measured and is reproduced by the self consistent nonlinear simulation driven by rigid body rotation, including the observation of higher m modes become more unstable with higher instability drive, given by faster rotation or steeper ion density profile.

- The simulation indicates that resonant hot electrons impart a real frequency to the rotational mode in the rotating frame of reference. The estimated magnitude of that contribution is consistent with the difference between the measured mode frequencies and the calculated frequency from electric field measurements.

5.3 Calculation of Radial Electric Field

In this section the equilibrium electric field induced by the external biasing of the mesh array is discussed. Since plasmas tend to shield electric fields in narrow sheath layers, it is difficult to generate a large scale field across a plasma volume. In this analytical model, collisions between ions and neutrals as the ions are accelerated by the external bias is the mechanism that sets up a radial volume current and, therefore, a radial electric field.

To determine the electric field, two methods are investigated. We first derive a bounce-averaged O.D.E. for the potential in flux co-ordinates. This method elucidates the physics nicely, analytically solving for the equilibrium using the ideal Ohm's law and the continuity equation, though at the expense of mathematical ease. Alternatively, we derive an expression for the current required to rotate the plasma based on conservation of charge, and use it to constrain the solution for the potential. The latter method is more direct, but we start with the former for completeness.

5.3.1 Potential Calculation

We start with the relation,

$$\mathbf{J} = \sigma \cdot \mathbf{E} = \sigma_p \mathbf{E}_\perp - \sigma_H (\mathbf{E}_\perp \times \hat{b}) + \sigma_o \mathbf{E}_\parallel, \tag{5.1}$$

where the various conductivities are the Hall, Pedersen, and specific conductivities[30], respectively, which are

$$\sigma_H = (ne/B)[{\kappa^2}_e/(1+{\kappa^2}_e) - {\kappa^2}_i/(1+{\kappa^2}_i)] \tag{5.2}$$

$$\sigma_p = \sigma_i/[1+{\kappa^2}_i] - \sigma_e/[1+{\kappa^2}_e] \tag{5.3}$$

$$\sigma_o = \sigma_i - \sigma_e, \tag{5.4}$$

where the σ_j are the electron and ion conductivies, $n_j q^2/m_j\nu_j$, and the κ_j are the ratios between the cyclotron frequencies and the collision frequencies, ω_{cj}/ν_j.

The field-aligned current is ignored in this case and the Hall current will be found to be *a posteriori* insignificant compared to the Pedersen term. With that in mind, we have,

$$\nabla \cdot \mathbf{J} = \nabla \cdot (\sigma_p \mathbf{E}_\perp) = (\nabla \sigma_p) \cdot \mathbf{E}_\perp + \sigma_p (\nabla \cdot \mathbf{E}_\perp) = 0. \tag{5.5}$$

We can put Equation 5.5 in dipole flux coordinates with the help of the following identity:

$$\nabla \cdot A = B^2 \frac{\partial}{\partial \chi}\left(\frac{\nabla\chi \cdot A}{B^2}\right) + B^2 \frac{\partial}{\partial \varphi}\left(\frac{\nabla\varphi \cdot A}{B^2}\right) + B^2 \frac{\partial}{\partial \psi}\left(\frac{\nabla\psi \cdot A}{B^2}\right) \tag{5.6}$$

where the flux coordinates are defined by the ideal dipole magnetic field, $\mathbf{B} = \nabla\varphi \times \nabla\psi = \nabla\chi$. In spherical coordinates, they are defined by $\psi = M\sin^2\theta/r$, $\chi = M\cos\theta/r^2$ and $B = (M/r^3)\sqrt{1+3\cos^2\theta}$.

In flux coordinates, we then have for the electric field,

$$\nabla \cdot \mathbf{E} = -B^2 \frac{\partial}{\partial \psi}\left(\frac{1}{B^2}|\nabla\psi|^2 \frac{\partial \Phi}{\partial \psi}\right). \tag{5.7}$$

Finally, putting Equation 5.7 into Equation 5.5, we get the following differential equation for the electric potential:

$$\frac{\partial \sigma_p}{\partial \psi}\frac{\partial \Phi}{\partial \psi}|\nabla\psi|^2 + \sigma_p B^2 \frac{\partial}{\partial \psi}\left(\frac{1}{B^2}|\nabla\psi|^2 \frac{\partial \Phi}{\partial \psi}\right) = 0. \tag{5.8}$$

Bounce Averaging

We solve for the electrostatic potentials in the equatorial plane. Averaging over field-lines is required for this. To bounce average Equation 5.8 integrals of the type,

$$\|A\| \equiv \int_0^1 \frac{d\chi}{B^2} A$$

must be computed. Applying bounce averaging to Equation 5.8, we get

$$\begin{aligned}
\int_0^1 \frac{d\chi}{B^2}(\nabla \cdot \mathbf{J}) \quad &= \frac{\partial \Phi}{\partial \psi}\int_0^1 \frac{d\chi}{B^2}|\nabla\psi|^2 \frac{\partial \sigma_p}{\partial \psi} + \int_0^1 d\chi \left[\sigma_p \frac{\partial}{\partial \psi}\left(\frac{|\nabla\psi|^2}{B^2}\frac{\partial \Phi}{\partial \psi}\right)\right] = 0 \\
&= \frac{\partial \Phi}{\partial \psi}\left[\int_0^1 \frac{d\chi}{B^2}\left(|\nabla\psi|^2 \frac{\partial \sigma_p}{\partial \psi}\right) + \int_0^1 d\chi \sigma_p \left(\frac{\partial}{\partial \psi}\frac{|\nabla\psi|^2}{B^2}\right)\right] \\
&+ \frac{\partial^2 \Phi}{\partial \psi^2}\int_0^1 d\chi \sigma_p \frac{|\nabla\psi|^2}{B^2} = 0
\end{aligned} \tag{5.9}$$

All quantities must be put into flux coordinates to carry out these integrals. Transforming the variable of integration to $\xi = \sin^2\theta$ and using the following relations facilitates this task:

$$r = \frac{M\xi}{\psi}, \qquad \chi = \frac{\psi^2}{M}\sqrt{\frac{1-\xi}{\xi^4}}, \qquad \frac{d\chi}{d\xi} = \frac{\psi^2}{M}\frac{3\xi-4}{2\xi^3\sqrt{1-\xi}}.$$

For example, B^2 in flux coordinates is $\frac{(4-3\xi)\psi^6}{M^4\xi^6}$and $|\nabla\psi|^2 = \frac{(4-3\xi)\psi^4}{M^2\xi^3}$.

The difficulty with this formulation thus far is that the partial derivatives in Equation 5.10 must be computed while keeping χ constant. In general this is a laborious task in the new co-ordinate system. Although this can be done to reach an O.D.E. for the potential, we can arrive at this same end in a more intuitive and less laborious manner by computing the current required to rotate the plasma. We do this in the following section after discussing the necessary assumptions. As for the partial derivatives, they can be done easily on the equatorial plane, however, where there is no χ dependence, and we also show the result of these calculations below.

Assumptions

Magnetic Field As mentioned in Section 3.1.3, the vacuum magnetic dipole field for CTX provides an excellent approximation to the point dipole field calculated from the standard Green's function for the poloidal flux. The vacuum field is used for calculating all quantities, such as ω_c, σ_p etc. This dramatically reduces computing time when performing bounce integrals.

Pedersen Conductivity The Pedersen conductivity must also be approximated. When the full form is kept, it requires prohibitive processing time to compute the necessary numerical integrals. However, in the applicable regime of low collisionality, $\kappa_j \gg 1$, it reduces to the following simplified form,

$$\sigma_p \approx nM_i\nu_{in}/B^2, \tag{5.10}$$

where $\nu_{in} = n_n\sigma_0 v_{thi}$, σ_0 is the neutral collision cross section, n_n is the neutral density, and v_{thi} is the ion thermal velocity. Here, we've taken ν_i to be only due to ion-neutral collisions, not including ion-ion collisions. This is a valid simplification for the low density plasmas investigated in CTX.

Density and Temperature Thus far we have ignored density and temperature profiles. To calculate the Pedersen conductivities - and the collision freqencies that they subsume - knowledge of temperature and density profiles is required. Temperature, in general, is an ill-known quantity in the highly non-Maxwellian CTX plasma. Thus, we simply impose a constant ion temperature profile. Equatorial density profiles can be roughly estimated from Figure 5.4. However, since I_{isat} is proportional to T_e as well as n it is difficult to know for certain the exact density profile, though it is certainly a power law steeper than $1/L^4$, the marginally stable profile. We will ultimately choose $n \propto L^{-6}$ for these calculations because it results in rigid $\mathbf{E} \times \mathbf{B}$ rotation in this model. This will be explained in the next section. As for the field line dependence, we adopt a model that has been used successfully in the nonlinear particle code[44, 42]. We simply give a sinusoidal profile along the field line peaked on the equator, giving, $n(\theta, r) \sim n_o \sin\theta (L_o/L)^n$, where $n \sim 6$.

A list of the CTX plasma and machine parameters used in making these calculations is given in Table 5.1.

5.3.2 Constant Current Calculation

In this section the equilibrium potential problem is calculated from the requirement of constant radial current. We return to Equation 5.5 and take the volume integral in flux coordinates:

$$\int\int\int \frac{d\varphi d\chi d\psi}{B^2} \nabla \cdot \mathbf{J} = -2\pi \int\int d\chi d\psi \frac{\partial}{\partial \psi} \left(\frac{\sigma_p |\nabla \psi|^2}{B^2} \frac{\partial \Phi}{\partial \psi} \right) = 0, \tag{5.11}$$

where we've plugged in for the electric field, carried out the axisymmetric φ integral, and used Equation 5.6. Carrying out the trivial integral in ψ gives us,

$$-2\pi \int d\chi \left\{ \frac{\sigma_p |\nabla \psi|^2}{B^2} \frac{\partial \Phi}{\partial \psi}|_{\psi_{max}} - \frac{\sigma_p |\nabla \psi|^2}{B^2} \frac{\partial \Phi}{\partial \psi}|_{\psi_{min}} \right\} = 0, \tag{5.12}$$

which is, in fact, the current, $I|_{\psi_{max}} - I|_{\psi_{min}} = 0$. Thus, the current is defined as,

$$I = -2\pi \frac{\partial \Phi}{\partial \psi} \int d\chi \frac{\sigma_p |\nabla \psi|^2}{B^2} = -2\pi \frac{\partial \Phi}{\partial \psi} \| \sigma_p |\nabla \psi|^2 \|. \tag{5.13}$$

It is convenient to introduce the field-line integrated Pedersen current,

$$\Sigma_p = \frac{\| \sigma_p |\nabla \psi|^2 \|}{\| |\nabla \psi|^2 \|} = \| \sigma_p |\nabla \psi|^2 \| / 4M, \tag{5.14}$$

Table 5.1: Key parameters used in the radial electric field calculation.

Dimension	Meaning	Typical Value
a	Bias Filament Location	26 cm
b	Chamber Wall Location	70 cm
L_0	Hot Electron Location	27 cm
B_a	Equatorial field strength	875 G
ψ_a	Magnetic flux, $B_a a^2$	6.4×10^5 Maxwells
M_a	Characteristic dipole magnetic moment, $B_a L_a^3$	1.7×10^7 G $\cdot$ cm^3
N_0	Plasma density	3.0×10^9 cm^{-3}
n_e	Electron density	5.0×10^9 cm^{-3}
T_e	Electron Temperature	50 eV
T_i	Ion Temperature	10 eV
v_{te}	Electron Thermal Velocity	3.0×10^8 cm/s
v_{ti}	Ion Thermal Velocity	2.2×10^6 cm/s
ν_{e0}	Electron Collision Frequency at L_0	4.4×10^3 Hz
ν_{i0}	Ion Collision Frequency at L_0	4.6×10^1 Hz
ω_{ce0}	Electron Cyclotron Frequency at L_0	1.54×10^{10} Hz
ω_{ci0}	Ion Cyclotron Frequency at L_0	8.4×10^6 Hz
σ_0	Neutral Cross Section	5×10^{-15} cm^2
σ_{e0}	Electron Conductivity at L_0	3.2×10^2 $\Omega \cdot$ cm^{-1}
σ_{i0}	Ion Conductivity at L_0	1.6×10^1 $\Omega \cdot$ cm^{-1}

so that Equation 5.13 becomes,

$$I = 8\pi M \Omega \Sigma_p, \tag{5.15}$$

where we've also noted that $\partial_\psi \Phi = -\Omega$, the $\mathbf{E} \times \mathbf{B}$ frequency. We use this equation to put constraints on the electrostatic potential, and thereby calculate the current, which can be compared to measured values to confirm our model of the transport that generates the electric field.

For completeness, we write down the form of Σ_p that we use for numerical calculations:

$$\begin{aligned} \Sigma_p &= \frac{1}{4M}\int_0^1 d\chi \frac{|\nabla\psi|^2}{B^2}\sigma_p = \frac{1}{4}\int_0^1 d\xi \left(\frac{3\xi - 4}{\sqrt{1-\xi}}\right)\sigma_p(\xi,\psi) \\ &= \frac{\nu_{in}\epsilon_0}{4}\int_0^1 d\xi \left(\frac{3\xi - 4}{\sqrt{1-\xi}}\right)\frac{\omega_{pi}^2}{\omega_{ci}^2}, \end{aligned} \tag{5.16}$$

since $\sigma_p = \nu_{in}\epsilon_0(\omega_{pi}^2/\omega_{ci}^2)$, where ω_{pi}^2 is the ion plasma frequency and ω_{ci}^2 is the ion cyclotron frequency.

Results

The observations, including the experimental floating potential scan, Figure 5.2, and the rigid rotation of the instability, are fit by a potential linear in ψ. With the boundary conditions, $\Phi(a) = -500$ V and $\Phi(b) = 0$ V we obtain the radial potentials and electric fields shown in Figures 5.17(a) and (b). With this induced radial field and the CTX magnetic dipole field, an azimuthal $\mathbf{E} \times \mathbf{B}$ flow will result. The rotation velocities and frequencies are shown in Figures 5.17(c) and (d). These calculated profiles are in blue. Also plotted in black are the profiles calculated from the experimental results shown in Figure 5.3.

The actual current calculated from Equation 5.15 is very close to the measured current from the bias power supply, ~ 2 mA. This is based on the observed (and calculated) $\mathbf{E} \times \mathbf{B}$ frequency of $\sim 20 - 25$ kHz and a density profile of $n(\psi) \propto \psi^6$. The latter can be obtained from Equation 5.15 by noting that both I and Ω are independent of ψ, so that Σ_p, and thus σ_p, must also be independent of ψ. Since $\sigma_p = n(\psi)M_i\nu_{in}/B^2$, where $\nu_{in} = n_n\sigma_0 v_{thi}$ is thought to be roughly independent of ψ in the CTX device, we must have $n(\psi)/B^2 \sim constant$, or $n(\psi) \sim \psi^6$ for σ_p (and therefore Ω) to be constant. This is a realistic density profile and is unstable to interchanges.

Using values from Table 5.1, we compute a current of $I \sim 0.8$ mA, about half the measured value. This calculation also serves as a check on density measurements through other methods, such as the Langmuir probe characteristic which is fraught with difficulty in a plasma with energetic electrons. By the same token, it gives us a better handle on the density profile than the profile of I_{isat} given in Figure 5.4, since I_{isat} is also proportional to T_e, not just n. In fact, it is valid to turn the question around and ask what density is required to obtain the observed emission current. This is, in effect, using the entire plasma as a probe.

To summarize, clearly the equilibrium model is close to what is seen experimentally, lending credibility to its underlying physical assumptions, including the argument that classical cross-field transport from ion-neutral collisions creates the radial current leading to the electric field. The fact that both the predicted (blue) and extrapolated (black) $\mathbf{E}\times\mathbf{B}$ frequencies are close to the observed frequency of the $m = 1$ rotational mode of $\sim 20-25$ kHz also gives confidence to the model.

5.4 Inclusion of Non-axisymmetric Effects

We now add the contributions due to non-axisymmetric terms that can arise in Ohm's law, Equation 5.1, due to either azimuthal dependencies of the fields or contributions from the Hall conductivity. Since the CTX biasing system is capable of inducing up to $m = 3$ potentials at the inner plasma boundary, this is a worthwhile problem to address, and introduces some interesting physics. These experiments have not been carried out to date, but the relevant theory to compare to experiment is a relatively simple extension of the results from the previous Section.

The field-aligned current is again ignored but we now allow the electrostatic potential to have azimuthal depencence, $\mathbf{E}_\perp(\psi,\varphi) = -\frac{\partial\Phi}{\partial\psi}\nabla\psi - \frac{\partial\Phi}{\partial\varphi}\nabla\varphi$, and we no longer omit the contribution from the Hall term. Thus we now have in analogy to Equation 5.5,

$$\nabla\cdot\mathbf{J} = (\nabla\sigma_p)\cdot\mathbf{E}_\perp + \sigma_p(\nabla\cdot\mathbf{E}_\perp) - (\nabla\sigma_H)\cdot(\mathbf{E}_\perp\times\hat{b}) - \sigma_H\nabla\cdot(\mathbf{E}_\perp\times\hat{b}) = 0. \qquad (5.17)$$

Since $\sigma_p = \sigma_p(\psi)$, the first term has no new azimuthal contribution. The second term

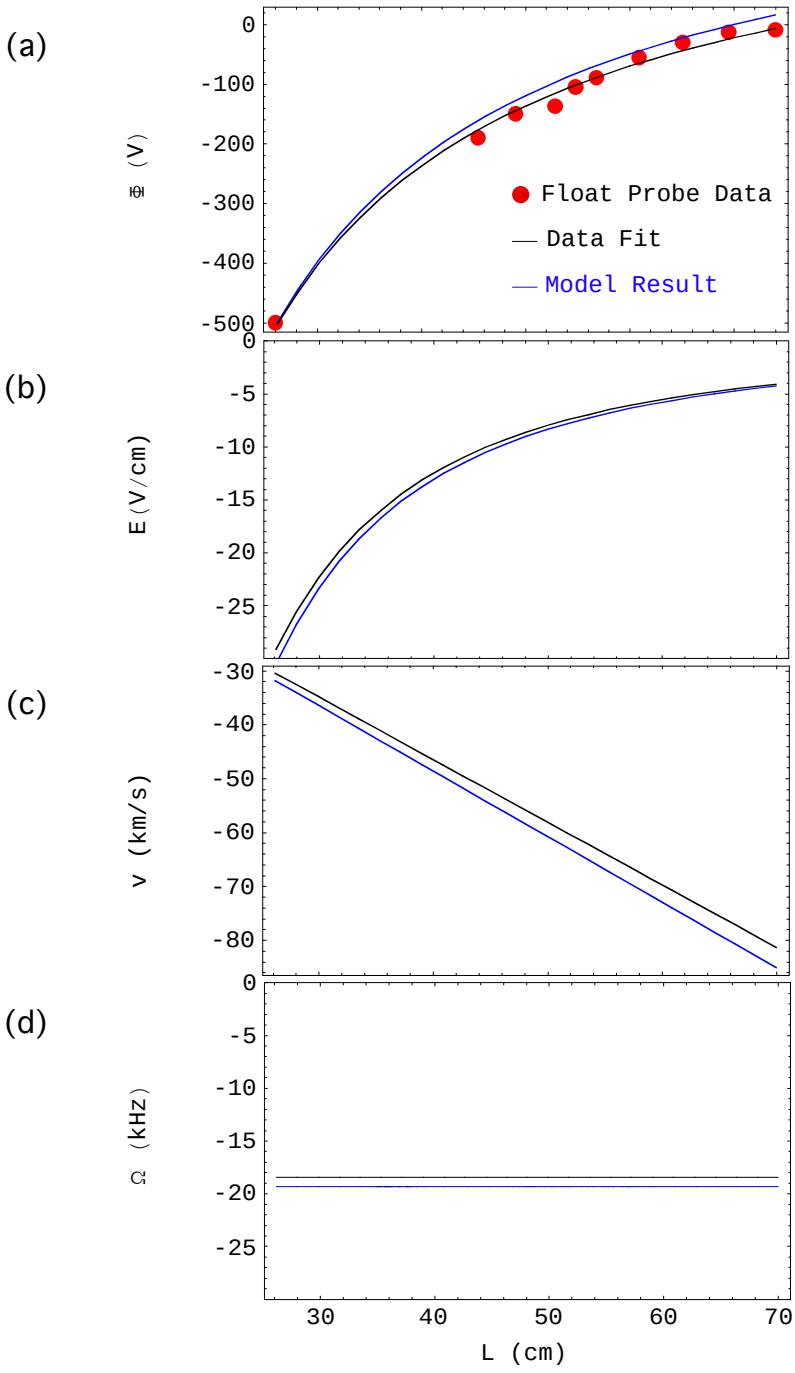

Figure 5.17: (a) The potential deduced from Equation 5.15 (in blue), (b) the resulting electric field, (c) the azimuthal $\mathbf{E} \times \mathbf{B}$ velocity, and (d) the frequency of rotation. The red dots are data points of floating potential, as shown in Figure 5.2, and the black lines are the fit to these points along with the electric field, flow velocity and rotation frequency calculated from this fit and the CTX dipole field.

does, however, and in analogy to Equation 5.7 we have for the electric field

$$\nabla \cdot \mathbf{E}_\perp = -B^2 \frac{\partial}{\partial \psi}\left(\frac{1}{B^2}|\nabla\psi|^2 \frac{\partial \Phi}{\partial \psi}\right) - B^2 \frac{\partial}{\partial \varphi}\left(\frac{1}{B^2}|\nabla\varphi|^2 \frac{\partial \Phi}{\partial \varphi}\right) \tag{5.18}$$

where the second term is the new term. After some algebra, we have from just the Pedersen contribution to Equation 5.17:

$$(\nabla\sigma_p)\cdot\mathbf{E}_\perp + \sigma_p(\nabla\cdot\mathbf{E}_\perp) = \frac{\partial^2\Phi}{\partial\psi^2}\sigma_p|\nabla\psi|^2 + \frac{\partial\Phi}{\partial\psi}\left[\frac{\partial\sigma_p}{\partial\psi}|\nabla\psi|^2 + \sigma_p B^2 \frac{\partial}{\partial\psi}\left(\frac{|\nabla\psi|^2}{B^2}\right)\right] + \frac{\partial^2\Phi}{\partial\varphi^2}\sigma_p\frac{B^2}{|\nabla\psi|^2}, \tag{5.19}$$

where the last term here is the new term with azimuthal dependence.

Now we must look at the Hall terms. To facilitate this task, we must calculate $\mathbf{E}_\perp \times \hat{b}$ and it's divergence. With $\mathbf{E}_\perp$ as given above in flux coordinates and $\hat{b} = (\nabla\varphi \times \nabla\psi)/B$, we get,

$$\mathbf{E}_\perp \times \hat{b} = -\frac{\partial\Phi}{\partial\psi}\frac{|\nabla\psi|^2}{B^2}\nabla\varphi + \frac{\partial\Phi}{\partial\varphi}\frac{|\nabla\varphi|^2}{B^2}\nabla\psi. \tag{5.20}$$

After some more work and finding a cancellation of two terms, we find for the divergence,

$$\nabla\cdot(\mathbf{E}_\perp \times \hat{b}) = \frac{\partial\Phi}{\partial\varphi}\left[|\nabla\varphi|^2 B\frac{\partial}{\partial\psi}\left(\frac{|\nabla\varphi|^2}{B^2}\right) - \frac{\partial B}{\partial\psi}\right]. \tag{5.21}$$

Finally, putting Equations 5.20 and 5.21 with Equation 5.19 into Equation 5.17, we get the following differential equation for the electric potential:

$$\begin{aligned}\frac{\partial^2\Phi}{\partial\psi^2}\sigma_p|\nabla\psi|^2 + \frac{\partial\Phi}{\partial\psi}\left[\frac{\partial\sigma_p}{\partial\psi}|\nabla\psi|^2 + \sigma_p B^2\frac{\partial}{\partial\psi}\left(\frac{|\nabla\psi|^2}{B^2}\right)\right] + \frac{\partial^2\Phi}{\partial\varphi^2}\sigma_p\frac{B^2}{|\nabla\psi|^2} \\ + \frac{\partial\Phi}{\partial\varphi}\left[\sigma_H\frac{B^3}{|\nabla\psi|^2}\frac{\partial}{\partial\psi}\left(\frac{|\nabla\varphi|^2}{B^2}\right) - \sigma_H\frac{\partial B}{\partial\psi} + \frac{\partial\sigma_H}{\partial\psi}B\right] = 0.\end{aligned} \tag{5.22}$$

This entire equation must now be bounce averaged as before.

Bounce Averaging

We simply write down the bounce integrals for completeness. There are four new terms to bounce average. They are,

$$\int_0^1 d\chi \frac{\sigma_p}{|\nabla\psi|^2} = c_4/\psi^4$$
$$\int_0^1 d\chi \frac{\sigma_H B}{|\nabla\psi|^2}\frac{\partial}{\partial\psi}\left(\frac{|\nabla\varphi|^2}{B^2}\right) = c_6/\psi^3$$
$$\int_0^1 d\chi \frac{\sigma_H}{B^2}\frac{\partial B}{\partial\psi} = c_7/\psi^3$$
$$\int_0^1 d\chi \frac{1}{B}\frac{\partial\sigma_H}{\partial\psi} = c_8/\psi^3,$$

where the c's are constants with subscripts refering (roughly) to their place in Equation 5.22.

Electrostatic Potential

As before we use the ideal magnetic dipole field for bounce averaging and in all definitions of physical quantities. Both Pedersen and Hall conductivities are approximated in their low collisional limit ($\kappa_j \gg 1$), dominated by ion-neutral events, which is an excellent approximation for the CTX parameters used. Once again the density is assumed to be of the form $n(\theta, r) \sim n_o \sin\theta (L_o/L)^n$ in spherical coordinates, and a constant temperature profile is taken.

Finally, we assume the potential to be of the form, $\Phi(\psi,\varphi) = \Re\{e^{im\varphi}\Phi^*(\psi)\}$, where $\Phi^*(\psi)$ is the potential which satisfies Equation 5.22, which now takes the simpler form,

$$c_1\frac{\partial^2\Phi^*}{\partial\psi^2} + \frac{c_2}{\psi}\frac{\partial\Phi^*}{\partial\psi} + \Phi^*\left[im\frac{c_3}{\psi} - m^2\frac{c_4}{\psi^2}\right] = 0, \tag{5.23}$$

where m is the azimuthal mode number and $c_3 = c_6 - c_7 + c_8$.

We see from Eqn 5.22 that the addition of the Hall conductivity has coupled the radial and azimuthal dynamics. We uncouple them with the above separation of variables at the cost of introducing complex terms to the eigenvalue equation for Φ^*. All terms containing σ_H are contained in the complex c_3 term, which we will variously turn on and off to gain insight into the Hall dynamics.

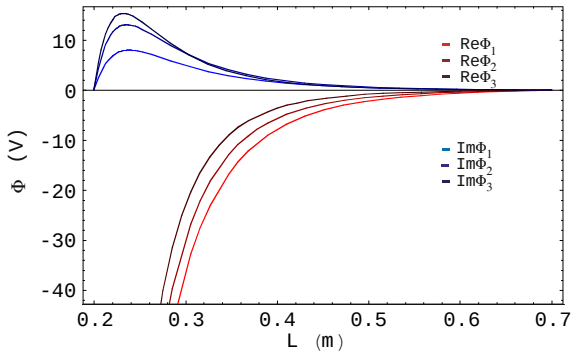

Figure 5.18: The real (reds) and imaginary (blues) solutions to Equation 5.23 for the electrostatic potential.

5.4.1 Results from Non-axisymmetric Terms

Electrostatic Potential

Once again, we compute the bounce integrals and Equation 5.23 with Mathematica. The latter is done with the three cases, $m = 1, 2$ and 3. These azimuthal mode numbers are examined since the biasing tungsten mesh system on CTX is segmented into 6 separate azimuthal regions, which is therefore capable of exciting up to $m = 3$ modes in the plasma by imposing an inner boundary condition on the potential like $\Phi(a)\cos(m\varphi)$. We impose $\Phi(a) = -300$ V and $\Phi(b) = 0$ V, similar to experimental conditions.

The electrostatic potential solved from the full form of Equation 5.23 is shown in Figure 5.18. (Note that after solving for the potential in flux co-ordinates, we transform back into cylindrical coordinates). Both imaginary (blues) and real (reds) parts of the potential are shown as a function of equatorial distance. The darker shades represent higher m numbers. The real parts are the solutions that are obtained when the complex σ_H terms are dropped from Equation 5.23 (ie. $c_3 = 0$). These solutions steepen with increasing m number. The $m = 1$ solution nearly overlaps that of the $m = 0$. The imaginary solutions are purely due to the Hall contribution and are strongly localized toward the core.

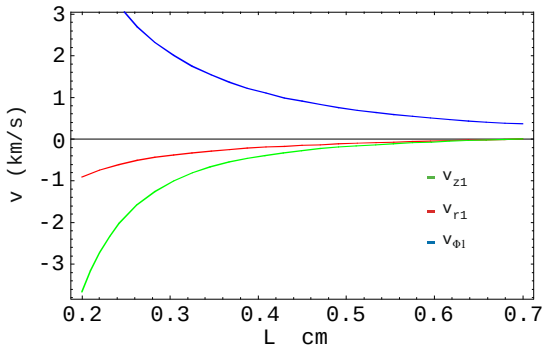

Figure 5.19: Radial (red), azimuthal (blue) and axial (green) $\mathbf{E} \times \mathbf{B}$ velocities for $m = 1$ as a function of equatorial distance.

$\mathbf{E} \times \mathbf{B}$ Flows, $\sigma_H = 0$.

Next, we solve for the $\mathbf{E} \times \mathbf{B}$ flows excited by the induced electrostatic potential. Previously we simply had azimuthal flows since our electric field was purely radial. Presently, we have both radial and azimuthal electric fields so that there will be $\mathbf{E} \times \mathbf{B}$ flows in all of the r, φ and z directions, setting up convection patterns.

A representative example of the three components of $\mathbf{u}_{E\times B}$ is shown for $m = 1$ in Figure 5.19. The Hall terms in this case are set to zero to begin with. The flows are plotted as a function of equatorial distance, arbitrarily choosing $z = 40$ cm and $\varphi = \pi/6$.

To see the dependence on m number of these flows, Figure 5.20 shows the components of $\mathbf{u}_{E\times B}$ for all three m numbers. Again, higher m numbers are displayed in darker shades. The effect on the azimuthal structure is marked: the velocity profiles increase and steepen dramatically with m number for the radial and axial flows, and somewhat less so in the azimuthal direction.

$\mathbf{E} \times \mathbf{B}$ Flows, $\sigma_H \neq 0$.

Now the effect of the Hall terms is added. In the next three plots we compare the flows for each m number with and without the Hall contribution. The lighter shades correspond to those including the Hall conductivity effects.

Clearly, the Hall terms cause a decrease in the velocties. This effect becomes more marked with increasing m number. This can be seen especially clearly in the azimuthal component

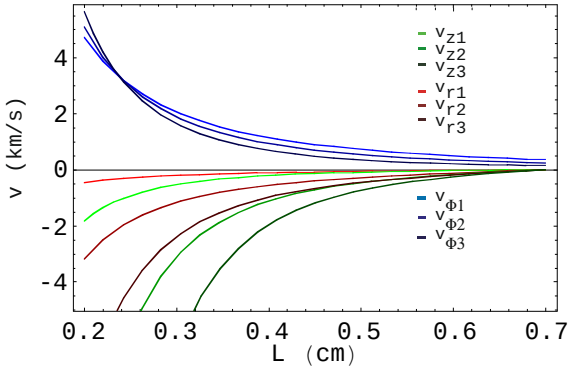

Figure 5.20: Radial (reds), azimuthal (blued) and axial (greend) $\mathbf{E}\times\mathbf{B}$ velocities for $m = 1, 2$ and 3 as a function of equatorial distance.

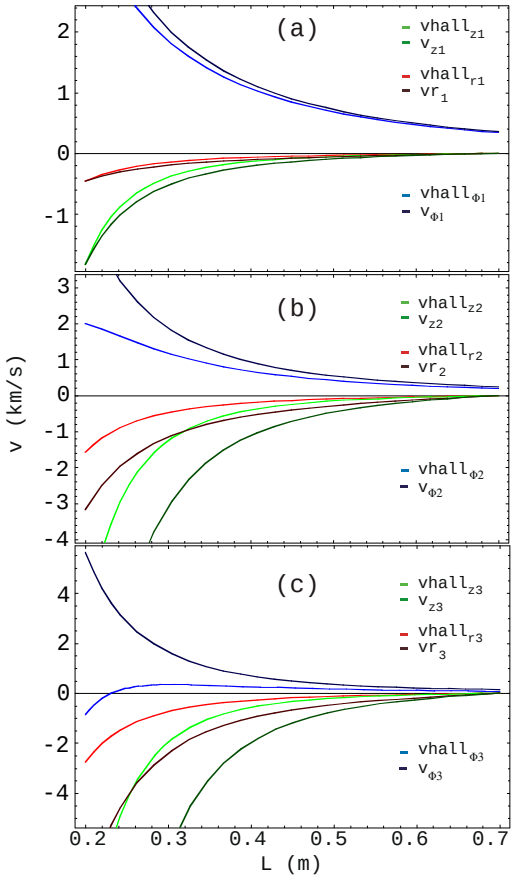

Figure 5.21: Radial (reds), azimuthal (blues) and axial (greens) $\mathbf{E}\times\mathbf{B}$ velocities as a function of equatorial distance with and without Hall contributions. The lighter shades correspond to those including the Hall terms. (a) $m = 1$; (b) $m = 2$; and (c) $m = 3$.

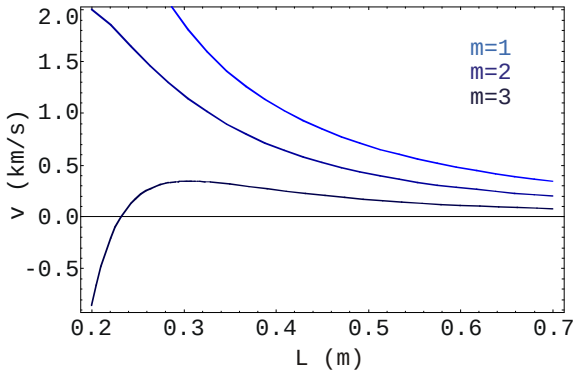

Figure 5.22: Azimuthal component of the $\mathbf{E} \times \mathbf{B}$ flow, u_φ, for $m = 1, 2$ and 3. Darker shades correspond to higher m numbers.

of the $\mathbf{E} \times \mathbf{B}$ flow, u_φ,which actually reverses direction near the inner boundary due to Hall term effects. This is displayed in Figure 5.22.

Finally, to get an idea of the actual physical flows in space, we examine vector plots of the direction of radial and azimuthal flows in the equatorial plane. The following plots compare flows with and without the Hall terms for $m = 1$ and 2. We also show a vectorplot for the $m = 3$ case in Figure 5.24, but only with the Hall terms since the comparisons at this point get rather complicated.

In both $m = 1$ and 2 cases, the effect of the Hall terms is to segment the azimuthal flow into convection zones. For the $\sigma_H = 0$ cases, the flows are still restricted to one azimuthal direction, despite regions of purely radial flow. However, in the $\sigma_H \neq 0$ cases, the direction of the azimuthal flow actually changes, as was seen in Figure 5.22; there are two zones in the $m = 1$ case, four in the $m = 2$ case and six in the $m = 3$ case. These changes in direction can be seen clearly along the outer boundary ($r \sim 0.7m$) where the flows are purely azimuthal.

Experimental study of these effects is possible in CTX using the 96 point gridded energy analyzer array discussed in Section 3.2.2.

5.5 Summary

In summary, a low frequency global flute mode is observed upon application of the external bias and rapid $\mathbf{E} \times \mathbf{B}$ rotation of the plasma. We identify this mode as the centrifugally driven

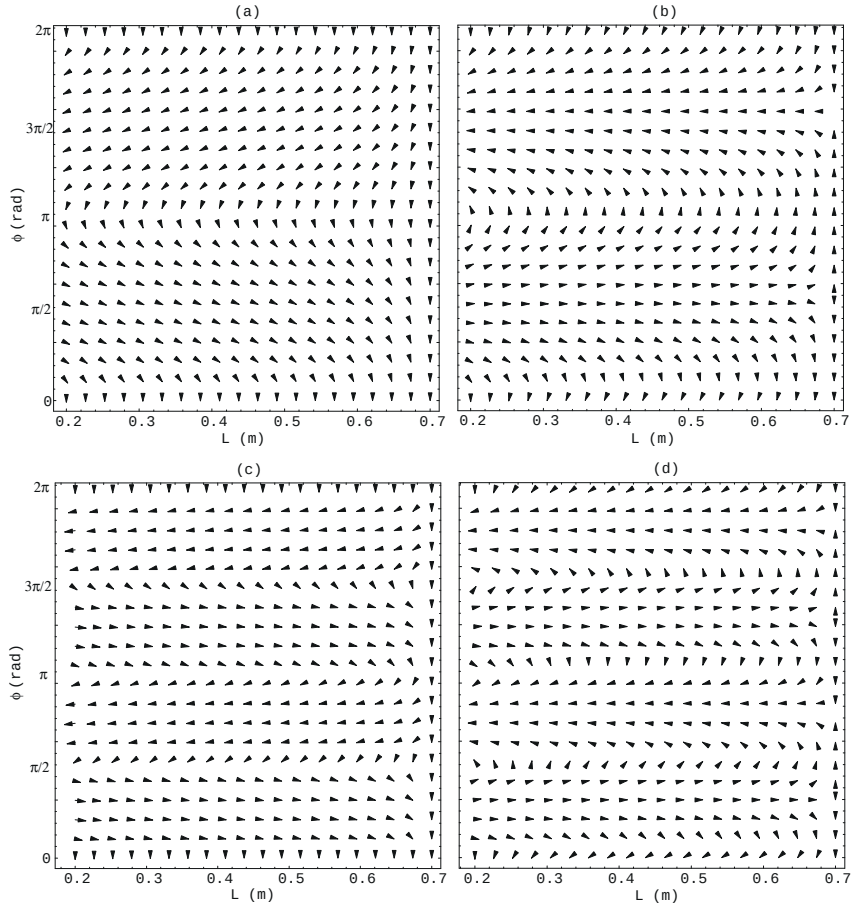

Figure 5.23: Vectorplot of radial and azimuthal flows in the equatorial plane for $m = 1$ and 2. (a) $m = 1$ without Hall terms; (b) $m = 1$ with Hall terms; (c) $m = 2$ without Hall terms; (d) $m = 2$ with Hall terms.

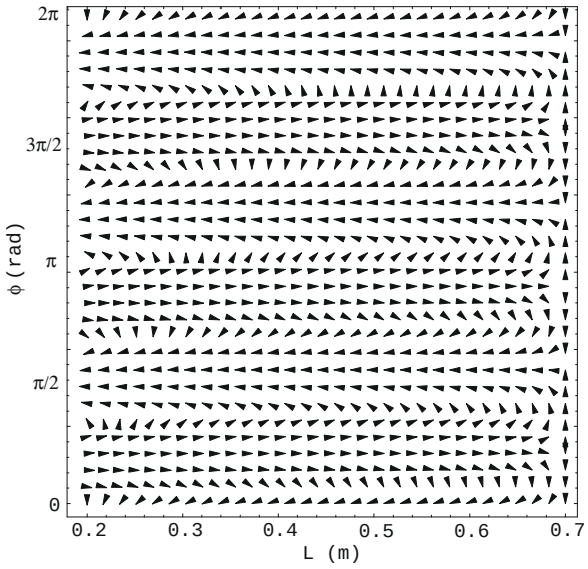

Figure 5.24: Vectorplot of radial and azimuthal flows in the equatorial plane for $m = 3$ with the Hall terms.

interchange instability. A multi-probe correlation analysis was performed on the mode, giving the global mode structure of the instability. The mode is dominated by low m numbers with a time independent mode structure, even as the frequency of the mode may be increasing due to the increasing bias. All these characteristics are reproduced by a self consistent nonlinear simulation with appropriate input values corresponding to plasma rotation frequency, ion density profile, hot electron fraction and electrostatic potential boundary conditions. In addition, some numerical damping of short wavelength modes is necessary.

The long-time nonlinearly saturated phase of the simulated instabilities tends to an $m = 1$ state which appears to be consistent with the experimentally observed modes, which are themselves in a saturated state. It is not clear that the linear state is ever experimentally observed.

Equilibrium calculations of the radial electric field are based on a model depending on ion neutral collisions characterized by the Pedersen conductivity, σ_p. The model calculates electric field values similar to what are seen experimentally and, accordingly, similar $\mathbf{E} \times \mathbf{B}$ rotation frequencies.

Non-axisymmetric effects are studied as well in Section 5.4 and show examples of driven

plasma convection. These results could be the topic of future experimental studies, since the tungsten mesh biasing array has the capability of application of up to an $m = 3$ potential on the inner boundary of the plasma. Furthermore, synchronous application of these potentials is possible.

Chapter 6

Interchange Instability Dispersion Relations

We use two methods for finding the dispersion relation for interchange instabilities driven by centrifugal forces. The first method is a MHD normal mode analysis, following Ferriere et al [14], while the second is a nonlinear two fluid method, after Mauel [44]. Both derivations are in dipole flux co-ordinates, (φ, ψ, χ). The same two-fluid analysis is then used to find the dispersion relation of the Hot Electron Interchange instability. Finally, the two drives are combined into a single dispersion relation for general interchanges caused by both curvature and rotational drives. Results from these calculations are used to interpret the experimental observations and simulation comparisons.

We find that the purely rotational mode has high m number modes being the most unstable, contrary to experimental observation. Addition of hot electron resonant effects, however, which add a real frequency to the modes, stabilizes higher m modes, and is a more realistic model of the experiment. This theory also explains the observation of a dominant $m = 2$ regime for the rotational mode when the magnetic field was dropped to 70% of its usual value, which results in a higher rotational instability drive and a lower HEI drive.

6.1 Rotational Mode - MHD Approach

We assume a one dimensional model where all background parameters are constant along fieldlines. That is,

$$\mathbf{c} = c_\psi \hat{e}_\psi \tag{6.1}$$

$$\mathbf{g}_{eff} = g_\psi \hat{e}_\psi \tag{6.2}$$

$$\mathbf{\Omega} \cdot \nabla\psi = 0 \tag{6.3}$$

where $\mathbf{c}$ is the magnetic curvature vector, $\mathbf{g}_{eff}$ is the effective gravity, which contains contributions due to normal gravity as well as the centrifugal force, $-\mathbf{\Omega} \times (\mathbf{\Omega} \times \mathbf{R})$, Ω is the rotation frequency, and $\hat{e}_\psi = \nabla\psi/|\nabla\psi|$. We will also assume zero pressure, so as to ignore pressure driven interchange drives. Finally, we look only for interchange modes, thus we force $k_\parallel = 0$.

6.1.1 Governing Equations

The basic MHD equations employed are the momentum equation,

$$\rho\frac{d\mathbf{v}}{dt} = -\nabla P_T + \frac{1}{4\pi}\mathbf{B}\cdot\nabla\mathbf{B} + \rho\mathbf{g}_{eff} - 2\rho\mathbf{\Omega}\times\mathbf{v}, \tag{6.4}$$

where the last two terms are due to effective gravity and the Coriolis force, and P_T refers to the total pressure, $P_T = P + P_M$; the continuity equation,

$$\frac{d\rho}{dt} = -\rho\nabla\cdot\mathbf{v}, \tag{6.5}$$

the frozen-field equation,

$$\frac{\partial\mathbf{B}}{\partial t} = \nabla\times(\mathbf{v})\times\mathbf{B}, \tag{6.6}$$

and the adiabatic equation of state,

$$\frac{d}{dt}\left(\frac{P}{\rho^\gamma}\right) = 0, \tag{6.7}$$

where $\gamma = 5/3$ is the adiabatic index, ρ is density, and $\mathbf{v}$ is the plasma velocity.

6.1.2 Dispersion Relation

After assuming wave-like solutions to these equations composed of time-independent equilibrium parts and time-dependent perturbations varying as $\exp(-\imath\omega t)$, a local dispersion relation can be found [14]. Spatial dependence of the perturbations are assumed to have the form $\exp \imath(m\varphi + k_\psi \psi + k_\parallel \chi)$. We just quote the result here and write down the $k_\parallel = 0$ root of the dispersion relation,

$$\omega^2 = \frac{m^2}{k_\perp^2}\omega_0^2 + \frac{(\mathbf{k}_\perp \cdot 2\mathbf{\Omega})^2}{k_\perp^2}, \tag{6.8}$$

where we've defined the magnetic Rayleigh-Taylor frequency, ω_0,

$$\begin{aligned} \omega_0^2 &= g_\psi \left[\frac{1}{\rho_0}\frac{\partial \rho_0}{\partial \psi}|\nabla\psi| - \frac{1}{P_{\gamma 0}}\frac{\partial P_{T0}}{\partial \psi}|\nabla\psi| - \frac{V_A^2}{c_s^2 + V_A^2}c_\psi \right] \\ &+ 2V_A^2 c_\psi \left[\frac{1}{B_0}\frac{\partial B_0}{\partial \psi}|\nabla\psi| - \frac{1}{P_{\gamma 0}}\frac{\partial P_{T0}}{\partial \psi}|\nabla\psi| + \frac{c_s^2}{c_s^2 + V_A^2}c_\psi \right], \end{aligned} \tag{6.9}$$

where $p_{\gamma 0} = \gamma P_0 + 2P_{M0}$, c_s is the ion sound speed, V_A is the Alfven speed, and the subscript 0 designates equilibrium quantities.

By using the equilibrium condition obtained from the momentum equation,

$$-\frac{1}{\rho_0}\frac{\partial P_{T0}}{\partial \psi}|\nabla\psi| + V_A^2 c_\psi = 0, \tag{6.10}$$

and enforcing $P_0 = 0$, the Rayleigh-Taylor frequency reduces to

$$\omega_0^2 = g_\psi \left[\frac{1}{\rho_0}\frac{\partial \rho_0}{\partial \psi}|\nabla\psi| - \frac{g_\psi}{V_A^2} \right] \tag{6.11}$$

and the interchange dispersion relation similarly simplifies to

$$\omega^2 = g_\psi \left(\frac{m^2}{k_\psi^2 + m^2} \right) \left[s^{-1}|\nabla\psi| - \frac{g_\psi}{V_A^2} \right], \tag{6.12}$$

where we've defined $s^{-1} = \frac{1}{\rho_0}\frac{\partial \rho_0}{\partial \psi}$ as the dimensionless background density scale-length.

6.1.3 Instability Criterion

For instability we must have $\omega^2 < 0$. Thus stability depends on the radial density profile and the sign of g_ψ. In other words $g_\psi s^{-1} < 0$ for instability. The second term in Equation 6.12

is usually small since V_A is usually large, and we will ignore it here. Recalling that $\mathbf{g}_\psi = \mathbf{g} - \mathbf{\Omega} \times (\mathbf{\Omega} \times \mathbf{R})$ and that gravity is negligible in any smallscale experiment, the stability criterion becomes

$$-\Omega^2 R \left(\frac{m^2}{k_\psi^2 + m^2} \right) s^{-1} |\nabla \psi| < 0, \tag{6.13}$$

or just

$$\frac{\partial \rho_0}{\partial \psi} > 0. \tag{6.14}$$

Since $\psi = M \sin^2 \theta / L$, a L dependence of $\rho \sim L^{-4}$ will give $\frac{\partial \rho_0}{\partial \psi} = 0$, the marginally unstable case. Thus a steeper radial profile than this is required for instability.

6.2 Rotational Mode - Two Fluid Approach

With this approach we model the cold electron and cold ion populations separately as fluids. As before, we ignore the thermalized electron population so as to drop contributions from pressure driven interchanges. Similarly, we continue to assume that the background parameters, such as density and potential, are functions of ψ only.

The electostatic potential is modeled as having an equilibrium time-independent part, $\Phi_0(\psi)$, corresponding to the external filament bias applied experimentally, as well as flute-like electrostatic modes with $k_\parallel \sim 0$,

$$\Phi(\psi, \varphi, t) = \Phi_0(\psi) + \tilde{\Phi}(\psi) \exp \imath (m\varphi - \omega t). \tag{6.15}$$

The perturbed potential also has radial dependence corresponding to the experimentally observed global mode structure. The resulting electric field is

$$\tilde{\mathbf{E}} = -\nabla \Phi = -\frac{\partial \Phi_0}{\partial \psi} \nabla \psi - \frac{\partial \tilde{\Phi}}{\partial \psi} \nabla \psi - \frac{\partial \tilde{\Phi}}{\partial \varphi} \nabla \varphi. \tag{6.16}$$

6.2.1 Cold Electron Response

We model the cold electrons as being advected by the $\mathbf{E}\times\mathbf{B}$ drift, which consists of contributions from the externally applied DC electric field as well as a perturbative term,

$$\mathbf{u}_E = \frac{\mathbf{E}\times\mathbf{B}}{B^2} = -\partial_\psi(\Phi_0+\tilde{\Phi})\frac{\nabla\varphi}{|\nabla\varphi|^2} + \partial_\varphi\tilde{\Phi}\frac{\nabla\psi}{|\nabla\psi|^2}. \tag{6.17}$$

The perturbed electron density is obtained from the continuity Equation

$$\dot{n}_e + \nabla\cdot(n_e\mathbf{u}_E) = 0. \tag{6.18}$$

Field-line averaging Equation 6.18 gives

$$\dot{N}_e + \frac{\partial}{\partial\varphi}(N_e\|\nabla\varphi\cdot\mathbf{u}_E\|) + \frac{\partial}{\partial\psi}(N_e\|\nabla\psi\cdot\mathbf{u}_E\|) = 0, \tag{6.19}$$

where $N_e = \int d\chi\frac{n_e}{B^2}$. Now substituting in Equation 6.17, we have

$$\dot{N}_e + \frac{\partial}{\partial\varphi}\left(N_e\left\|-\frac{\partial\Phi_0}{\partial\psi}-\frac{\partial\tilde{\Phi}}{\partial\psi}\right\|\right) + \frac{\partial}{\partial\psi}\left(N_e\left\|\frac{\partial\tilde{\Phi}}{\partial\varphi}\right\|\right) = 0. \tag{6.20}$$

We identify the gradient of the background potential with the induced $\mathbf{E}\times\mathbf{B}$ frequency, $\partial_\psi\Phi_0 \equiv -\Omega$. In addition, since both Φ_0 and $\tilde{\Phi}$ don't have any field line dependence, they come out of the integrals, which simply give unity, leaving,

$$\dot{N}_e + \frac{\partial}{\partial\varphi}\left(N_e\left(\Omega-\frac{\partial\tilde{\Phi}}{\partial\psi}\right)\right) + \frac{\partial}{\partial\psi}\left(N_e\frac{\partial\tilde{\Phi}}{\partial\varphi}\right) = 0. \tag{6.21}$$

6.2.2 Cold Ion Response

The ion response is complicated by the larger ion mass which demands that we allow the ions to be advected by the $\mathbf{E}\times\mathbf{B}$ drift as well as the ion polarization drift, which is given by,

$$\begin{aligned}\mathbf{u}_{di} &= \frac{1}{\omega_{ci}B}\frac{d\tilde{\mathbf{E}}}{dt} = -\frac{1}{\omega_{ci}B}\frac{d}{dt}\nabla\tilde{\Phi}\\ &= -\frac{1}{\omega_{ci}B}\frac{d}{dt}\left(\frac{\partial\tilde{\Phi}}{\partial\psi}\nabla\psi+\frac{\partial\tilde{\Phi}}{\partial\varphi}\nabla\varphi\right),\end{aligned}$$

where

$$\begin{aligned}\frac{d}{dt} &= \frac{\partial}{\partial t} + \mathbf{u}_E \cdot \nabla \\ &= \frac{\partial}{\partial t} - \frac{\partial \Phi_0}{\partial \psi}\frac{\partial}{\partial \varphi} \\ &= \frac{\partial}{\partial t} + \Omega \frac{\partial}{\partial \varphi},\end{aligned}$$

where ω_{ci} is the ion cyclotron frequency. Since $|\Phi_0| \gg |\tilde{\Phi}|$ in the other $\mathbf{E} \times \mathbf{B}$ terms (see Equation 6.17), they don't contribute to the advection term.

However, in addition we must also allow the ions to be advected by the centrifugal drift induced by the externally imposed bulk $\mathbf{E} \times \mathbf{B}$ rotation of the plasma. The centifugal force is given in cylindrical co-ordinates by

$$\mathbf{F}_c(R, \varphi, z) = M_i \Omega^2 \mathbf{R}, \tag{6.22}$$

where M_i is the ion mass.

We can calculate the centrifugal drift, $\mathbf{u}_c$, in spherical co-ordinates easily and then transform it into flux co-ordinates. Using the dipole magnetic field in spherical co-ordinates,

$$\mathbf{B}(\mathbf{r}, \theta, \varphi) = M(-2\cos\theta/r^3, -\sin\theta/r^3, 0), \tag{6.23}$$

where M is the dipole magnetic moment, and rewriting the centrifugal force in spherical co-ordinates,

$$\mathbf{F}_c(r, \theta, \varphi) = M_i \Omega^2 r \sin\theta \{\sin\theta, \cos\theta, 0\}, \tag{6.24}$$

we then calculate the drift as,

$$\mathbf{u}_c = \frac{1}{q}\frac{\mathbf{F}_c \times \mathbf{B}}{B^2} = \frac{M_i M}{qB^2}\frac{\sin\theta}{r^2}(2 - 3\sin^2\theta)\Omega^2 \hat{\varphi}. \tag{6.25}$$

We also write down the expression for the centrifugal drift in flux co-ordinates:

$$\mathbf{u}_c(\psi, \xi) = \frac{M_i}{qB^2 M}\frac{\psi^2(2-3\xi)}{\xi^{1/2}}\Omega^2 \ell_\varphi \nabla\varphi = \frac{\Omega^2}{\omega_{ci}B}\psi(2-3\xi)\xi\nabla\varphi = u_c \nabla\varphi, \tag{6.26}$$

where we use $\xi = \sin^2\theta$ instead of χ in anticipation of the bounce integrations that will be necessary, and where $\ell_\varphi = r = M\xi^{3/2}\psi$ is scale factor in transforming $\hat{\varphi}$ to $\nabla\varphi$.

Finally, it is also of interest to include drifts due to the gravitational force in magnetospheric environments. Of course, it is less important in the laboratory setting, but we calculate it and include it nonetheless:

$$\mathbf{F}_g(R,\theta,\varphi) = -G\frac{M_i m\mathbf{r}}{r^3} = -gM_i\left(\frac{r_0}{r}\right)^2\hat{r}, \tag{6.27}$$

where m is presumably a planetary mass, G is the universal gravitational constant and g is local magnitude of gravity. The drift is

$$\mathbf{u}_g = \frac{1}{q}\frac{\mathbf{F}_g\times\mathbf{B}}{B^2} = \frac{gM_iM}{qB^2}\left(\frac{r_0}{r}\right)^2\frac{\sin\theta}{r^3}\hat{\varphi}. \tag{6.28}$$

In flux co-ordinates we have

$$\mathbf{u}_g(\psi,\xi) = \frac{g}{\omega_{ci}BM}\frac{\psi^4}{\xi\psi_0^2}\nabla\varphi = u_g\nabla\varphi. \tag{6.29}$$

We can now solve the field-line averaged ion continuity equation for N_i:

$$\dot{N}_i + \frac{\partial}{\partial\varphi}(N_i\|\nabla\varphi\cdot\mathbf{v}_i\|) + \frac{\partial}{\partial\psi}(N_i\|\nabla\psi\cdot\mathbf{v}_i\|) = 0, \tag{6.30}$$

with the ion velocity given by

$$\mathbf{v}_i = \mathbf{u}_E + \mathbf{u}_{di} + \mathbf{u}_c + \mathbf{u}_g, \tag{6.31}$$

where the first term is the $\mathbf{E}\times\mathbf{B}$ drift, the second is the ion polarization drift, third is the ion centrifugal drift and last is the gravity drift. To write down the analogy with Equation 6.20 we first calculate the following terms,

$$\nabla\varphi\cdot\mathbf{u}_i = -\frac{\partial\Phi_0}{\partial\psi} - \frac{\partial\tilde{\Phi}}{\partial\psi} - \frac{1}{\omega_{ci}B}\frac{d}{dt}\left(\frac{\partial\tilde{\Phi}}{\partial\varphi}\right)|\nabla\varphi|^2 + (u_c+u_g)|\nabla\varphi|^2 \tag{6.32}$$

$$\nabla\psi\cdot\mathbf{u}_i = \frac{\partial\tilde{\Phi}}{\partial\varphi} - \frac{1}{\omega_{ci}B}\frac{d}{dt}\left(\frac{\partial\tilde{\Phi}}{\partial\psi}\right)|\nabla\psi|^2, \tag{6.33}$$

where, for the $\nabla\varphi$ component, the first two terms are the background and perturbed $\mathbf{E}\times\mathbf{B}$ drifts respectively, the third is the ion polarization drift and the fourth is the centrifugal and gravity drifts; for the $\nabla\psi$ component, we have just the perturbed $\mathbf{E}\times\mathbf{B}$ drift and the ion polarization drift. Equation 6.30 now becomes,

$$\begin{aligned}\dot{N}_i &+ \frac{\partial}{\partial\varphi}\left[N_i\left(-\frac{\partial\Phi_0}{\partial\psi} - \frac{\partial\tilde{\Phi}}{\partial\psi} - \left\|\frac{|\nabla\varphi|^2}{\omega_{ci}B}\right\|\frac{d}{dt}\left(\frac{\partial\tilde{\Phi}}{\partial\varphi}\right) + \left\|(u_c+u_g)|\nabla\varphi|^2\right\|\right)\right] \\ &+ \frac{\partial}{\partial\psi}\left[N_i\left(\frac{\partial\tilde{\Phi}}{\partial\varphi} - \left\|\frac{|\nabla\psi|^2}{\omega_{ci}B}\right\|\frac{d}{dt}\left(\frac{\partial\tilde{\Phi}}{\partial\psi}\right)\right)\right] = 0.\end{aligned} \tag{6.34}$$

Each of these terms must now be field-line averaged. These integrations are performed numerically. The three $\mathbf{E}\times\mathbf{B}$ terms have no χ dependence and therefore come out of the integrals. Since these averages are density weighted, some assumption regarding the density profile must be taken. Here we assume a broad field line profile, $n\sim\sqrt{\xi}=\sin\theta$, as in the equilibrium calculations in the previous Chapter. The remaining terms are included here:

$$\|\nabla\varphi\cdot\mathbf{u}_{di}\| = -\left\|\frac{|\nabla\varphi|^2}{\omega_{ci}B}\right\|\frac{d}{dt}\left(\frac{\partial\tilde{\Phi}}{\partial\varphi}\right) = -0.66\frac{M^2B_0}{\omega_{ci0}\psi^4}\frac{d}{dt}\left(\frac{\partial\tilde{\Phi}}{\partial\varphi}\right) \tag{6.35}$$

$$\|\nabla\psi\cdot\mathbf{u}_{di}\| = -\left\|\frac{|\nabla\psi|^2}{\omega_{ci}B}\right\|\frac{d}{dt}\left(\frac{\partial\tilde{\Phi}}{\partial\psi}\right) = -0.77\frac{M^2B_0}{\omega_{ci0}\psi^2}\frac{d}{dt}\left(\frac{\partial\tilde{\Phi}}{\partial\psi}\right) \tag{6.36}$$

$$\|\nabla\varphi\cdot\mathbf{u}_{c}\| = \frac{B_0}{\omega_{ci0}}\left\|\frac{(2-3\xi)\xi|\nabla\varphi|^2}{B^2}\right\|\Omega^2\psi = -0.54\frac{\Omega^2}{\omega_{ci0}}\left(\frac{\psi_0}{\psi}\right)^3 \tag{6.37}$$

$$\|\nabla\varphi\cdot\mathbf{u}_{g}\| = \frac{gB_0}{\omega_{ci0}M}\left\|\frac{|\nabla\varphi|^2}{\xi B^2}\right\|\left(\frac{\psi^4}{\psi_0^2}\right) = 0.71\frac{gL_0^2B_0}{\omega_{ci0}M_0} = 0.71\frac{\Omega_g^2}{\omega_{cio}}, \tag{6.38}$$

where ω_{ci0} is the ion cyclotron frequency at B_0, and we've defined the gravitational frequency, $\Omega_g^2 = gL_0^2B_0/M_0 = g/L_0$.

The entire ion continuity equation can now be written down:

$$\begin{aligned}\dot{N}_i &+ \frac{\partial}{\partial\varphi}\left[N_i\left(\Omega-\frac{\partial\tilde{\Phi}}{\partial\psi}-0.66\frac{M^2B_0}{\omega_{ci0}\psi^4}\frac{d}{dt}\left(\frac{\partial\tilde{\Phi}}{\partial\varphi}\right)-0.54\frac{\Omega^2}{\omega_{ci0}}\left(\frac{\psi_0}{\psi}\right)^3+0.71\frac{\Omega_g^2}{\omega_{ci0}}\right)\right] \\ &+ \frac{\partial}{\partial\psi}\left[N_i\left(\frac{\partial\tilde{\Phi}}{\partial\varphi}-0.77\frac{M^2B_0}{\omega_{ci0}\psi^2}\frac{d}{dt}\left(\frac{\partial\tilde{\Phi}}{\partial\psi}\right)\right)\right]=0.\end{aligned} \tag{6.39}$$

6.2.3 Linear Dispersion Relation

The linear dispersion relation for low-frequency flute-like modes driven by rotation in a dipole plasma can be derived from Equations 6.21 and 6.39 and the Poisson equation or the quasineutrality approximation. To solve for the perturbed ion and electron densities we linearize the electostatic potential fluctuations as follows [44]:

$$\tilde{\Phi}(\psi,\varphi,t)\approx\Phi_m(\psi^*)\exp(m\varphi-\omega t)\left[1-\left(\frac{\psi-\psi^*}{\Delta\psi}\right)^2+\cdots\right], \tag{6.40}$$

where m is the azimuthal mode number and $\psi^*=B^*L^2$ is the flux surface of peak mode amplitude. That is, we take $\partial\Phi/\partial\psi|_{\psi^*}=0$. $\Delta\psi$ is the radial mode width, defined as $\Delta\psi\equiv 2\psi^*/k_LL$.

Beginning with the electron density, we return to Equation 6.21 and linearize:

$$\dot{\tilde{N}}_e = \frac{\partial \tilde{N}_e}{\partial \varphi}\left(\frac{\partial \tilde{\Phi}}{\partial \psi} - \Omega\right) + N_{e0}\frac{\partial}{\partial \varphi}\left(\frac{\partial \tilde{\Phi}}{\partial \psi} - \Omega\right) - \frac{\partial N_{e0}}{\partial \psi}\frac{\partial \tilde{\Phi}}{\partial \varphi} - N_{e0}\frac{\partial^2 \tilde{\Phi}}{\partial \varphi \partial \psi}. \tag{6.41}$$

Any term involving $\partial\tilde{\Phi}/\partial\psi$ is set to zero, and we are left with

$$-\imath\omega\tilde{N}_e = -\imath m\tilde{N}_e\Omega - \imath m\Phi_m\frac{\partial N_{e0}}{\partial \psi}. \tag{6.42}$$

Solving for the electron density, we have

$$\tilde{N}_e = \frac{1}{\omega - m\Omega} m\Phi_m \frac{\partial N_{e0}}{\partial \psi}. \tag{6.43}$$

Similarly, we now solve for the perturbed ion density from Equation 6.39. The linearized ion continuity equation is then

$$\begin{aligned} -\imath\omega\tilde{N}_i + \imath m\tilde{N}_i\Omega \qquad & -0.66\imath m^2(\omega - m\Omega)N_{i0}\frac{M^2B_0}{\omega_{ci0}\psi^4}\Phi_m - \imath m\tilde{N}_i\left[0.54\frac{\Omega^2}{\omega_{ci0}}\left(\frac{\psi_0}{\psi}\right)^3 - 0.71\frac{\Omega_g^2}{\omega_{ci0}}\right] \\ & + \imath m\Phi_m\frac{\partial N_{e0}}{\partial \psi} + 0.77\imath(\omega - m\Omega)N_{i0}\frac{M^2B_0}{\omega_{ci0}\psi^2}\frac{\partial^2\tilde{\Phi}}{\partial\psi^2} = 0. \end{aligned} \tag{6.44}$$

We define some shorthand for the gravity and centrifugal terms in Equation 6.44:

$$\omega_{cf} = 0.54\frac{\Omega^2}{\omega_{ci0}}\left(\frac{\psi_0}{\psi}\right)^3 \tag{6.45}$$

$$\omega_g = 0.71\frac{\Omega_g^2}{\omega_{ci0}}. \tag{6.46}$$

Gathering terms, we find

$$\tilde{N}_i = \frac{1}{\omega - m\Omega + m(\omega_{cf} - \omega_g)}\left[m\Phi_m\frac{\partial N_{i0}}{\partial\psi} + (\omega - m\Omega)N_{i0}\frac{M^2B_0}{\omega_{ci0}\psi^2}\left(0.77\frac{\partial^2\tilde{\Phi}}{\partial\psi^2} - 0.66\frac{m^2}{\psi^2}\Phi_m\right)\right]. \tag{6.47}$$

From Equation 6.40 we have $\partial^2\tilde{\Phi}/\partial_t\partial\psi = -2(k_LL/2\psi^*)^2\Phi_m$. Again, to facilitate algebra we introduce two more definitions for terms in Equation 6.47:

$$\begin{aligned} \mathcal{N} &= m\frac{\partial N_{i0}}{\partial\psi} \\ \mathcal{P} &= \frac{M^2B_0}{\omega_{ci0}\psi^{*2}}N_{i0}\left[1.54\left(\frac{k_LL}{2\psi^*}\right)^2 + 0.66\frac{m^2}{\psi^{*2}}\right]. \end{aligned}$$

These terms represent density gradient and ion polarization forces. The perturbed ion density is now

$$\tilde{N}_i = \frac{1}{\omega - m\Omega + m(\omega_{cf} - \omega_g)} \left[\mathcal{N} - (\omega - m\Omega)\mathcal{P}\right] \Phi_m. \tag{6.48}$$

Similarly, we can also write the perturbed electron density in this notation,

$$\tilde{N}_e = \frac{1}{\omega - m\Omega}\mathcal{N}\Phi_m. \tag{6.49}$$

6.2.4 Quasi-Neutrality

To a first approximation, we can set $\tilde{N}_i \sim \tilde{N}_e$, which gives us,

$$\frac{1}{\omega - m\Omega + m(\omega_{cf} - \omega_g)} \left[\mathcal{N} - (\omega - m\Omega)\mathcal{P}\right] = \frac{1}{\omega - m\Omega}\mathcal{N}, \tag{6.50}$$

and

$$-(\omega - m\Omega)(\omega - m\Omega)\mathcal{P} = m(\omega_{cf} - \omega_g)\mathcal{N}. \tag{6.51}$$

Moving into the $\mathbf{E} \times \mathbf{B}$ frame, $\omega' = \omega - m\Omega$, Equation 6.51 becomes

$$-\omega'^2\mathcal{P} = m(\omega_{cf} - \omega_g)\mathcal{N}. \tag{6.52}$$

For instability, we require $\omega'^2 < 0$, or,

$$\frac{m(\omega_{cf} - \omega_g)\mathcal{N}}{\mathcal{P}} > 0, \tag{6.53}$$

or just $\mathcal{N} > 0$ when the centrifugal drive is greater than the gravitational drive, which is equivalent to $\partial N_0/\partial\psi > 0$, the expected MHD result. The condition $\omega_{cf} = \omega_g$ defines a stable flux surface, $\psi_s^3 \equiv 0.68\Omega^2 M^2/gr_0^2$, which separates the spatial instability regions of the rotational and gravitational interchange modes.

6.2.5 Poisson Equation

We can also plug in the perturbed densities into the Poisson equation and solve for ω, thereby giving a dispersion relation. The field-line averaged Poisson equation in flux co-ordinates is

$$\nabla^2\Phi = \frac{\partial}{\partial\varphi}\left(h_\varphi\frac{\partial\Phi}{\partial\varphi}\right) + \frac{\partial}{\partial\psi}\left(h_\psi\frac{\partial\Phi}{\partial\psi}\right) = -4\pi e(\tilde{N}_i - \tilde{N}_e), \tag{6.54}$$

where two geometrical terms define the transformation of the Laplacian operator intro field-line averaged flux co-ordinates:

$$h_\varphi \equiv \int \frac{d\chi}{|\nabla\psi|^2} = 2\frac{M}{\psi^2} \tag{6.55}$$

$$h_\psi = \int \frac{d\chi}{|\nabla\varphi|^2} = 2M. \tag{6.56}$$

Having assumed that $\partial_\psi \Phi_0 = constant$, Φ_0 does not appear again on the left hand side of the Poisson equation. Using Equations 6.48 and 6.49, we have

$$-2M\left[\frac{m^2}{\psi^{*2}} + 4\left(\frac{k_L L}{2\psi^*}\right)^2\right]\Phi_m = -4\pi e\left[\frac{1}{\omega - m\Omega + m(\omega_{cf} - \omega_g)}\left[\mathcal{N} - (\omega - m\Omega)\mathcal{P}\right] - \frac{1}{\omega - m\Omega}\mathcal{N}\right]\Phi_m. \tag{6.57}$$

Canceling Φ_m's, moving into the ω' frame again, and rearranging,

$$\left(m^2 + (k_L L)^2\right) = -\frac{4\pi e\psi^{*2}}{2M}\left[\frac{\omega'^2\mathcal{P} + m(\omega_{cf} - \omega_g)\mathcal{N}}{\omega'(\omega' + m(\omega_{cf} - \omega_g))}\right]. \tag{6.58}$$

To procede and get a more physical understanding of what each term represents, we look at the first term on the right hand side of Equation 6.58 separately and plug back in for $\mathcal{P}$:

$$\begin{aligned}
\frac{4\pi e\psi^{*2}}{2M}\mathcal{P} &= \frac{4\pi e\psi^{*2}}{2M}\cdot\frac{M^2 B_0}{\omega_{ci0}\psi^2}N_{i0}\left[0.77\left(2\frac{k_L L}{2\psi^*}^2\right) + 0.66\frac{m^2}{\psi^{*2}}\right] \\
&= \frac{\omega_{pi}^2}{2\omega_{ci0}^2}\left(\frac{MB_0^2}{\psi^2}\right)(0.39(k_L L)^2 + 0.66m^2) \\
&\approx 0.91\frac{\langle\omega_{pi}^2\rangle}{2\omega_{ci0}^2}(0.39(k_L L)^2 + 0.66m^2) \\
&= 0.30m_\perp^2\frac{\langle\omega_{pi}^2\rangle}{\omega_{ci0}^2},
\end{aligned}$$

where $\omega_{pi}^2 = 4\pi e^2 N_0/M_i$ is the ion plasma frequency, and recalling $\langle\omega_{pi}\rangle = \omega_{pi}\delta V^{-1}(\psi) \approx \omega_{pi}/(0.91M^3/\psi^4)$, and $m_\perp^2 = (0.60(k_L L)^2 + m^2)$.

In most laboratory plasmas, the term $\langle\omega_{pi}^2\rangle/\omega_{ci0}^2 \gg 1$, which is a high density limit. In CTX, $\langle\omega_{pi}^2\rangle/\omega_{ci0}^2 \simeq 10^3$ in fact, so that the polarization term is quite large. Physically, this just means that the plasma responds rapidly to changing electric fields. Polarization drifts are then stabilizing since they serve to eliminate the build-up of large electric fields which cause charge separation, currents and growing modes.

Now we look at the second term on the right hand side of Equation 6.58:

$$\begin{aligned}\frac{4\pi e\psi^{*2}}{2M}(\omega_{cf}-\omega_g)\mathcal{N} &= \frac{4\pi e\psi^{*2}}{2M}\cdot\left(0.54\frac{\Omega^2}{\omega_{ci0}}\left(\frac{\psi_0}{\psi}\right)^3-0.71\frac{\Omega_g^2}{\omega_{ci0}}\right)\cdot m\frac{\partial N_0}{\partial\psi}\\ &\approx m\frac{\langle\omega_{pi}^2\rangle}{\omega_{ci0}^2}\left(0.49\Omega^2\left(\frac{\psi_0}{\psi}\right)^3-0.64\Omega_g^2\right)\left(\frac{\psi}{N_0}\frac{\partial N_0}{\partial\psi}\right)\\ &= m\frac{\langle\omega_{pi}^2\rangle}{\omega_{ci0}^2}\Gamma_r^2,\end{aligned}$$

where we've defined the rotational interchange instability drive,

$$\begin{aligned}\Gamma_r^2 &\equiv \left(0.49\Omega^2\left(\frac{\psi_0}{\psi}\right)^3-0.64\Omega_g^2\right)\left(\frac{\psi}{N_0}\frac{\partial N_0}{\partial\psi}\right) \qquad (6.59)\\ &= \left(0.49\Omega^2\left(\frac{\psi_0}{\psi}\right)^3-0.64\Omega_g^2\right)s^{-1},\end{aligned}$$

where s^{-1} is the dimensionless background density scale length.

We reintroduce these terms into Poisson's equation, Equation 6.58, and solve for a stability criterion,

$$\left(m^2+(k_LL)^2\right)=\frac{-1}{\omega'(\omega'+m(\omega_{cf}-\omega_g))}\left[m_\perp^2\omega'^2\frac{\langle\omega_{pi}^2\rangle}{\omega_{ci0}^2}+m^2\frac{\langle\omega_{pi}^2\rangle}{\omega_{ci0}^2}\Gamma_r^2\right]. \qquad (6.60)$$

Rearranging,

$$\omega'^2\left[m_\perp^2\frac{\langle\omega_{pi}^2\rangle}{\omega_{ci0}^2}+\left(m^2+(k_LL)^2\right)\right]+m\left(m^2+(k_LL)^2\right)(\omega_{cf}-\omega_g)\omega'+m^2\frac{\langle\omega_{pi}^2\rangle}{\omega_{ci0}^2}\Gamma_r^2=0, \qquad (6.61)$$

In the first term, $(m^2+(k_LL)^2)$ can be dropped, since $(m^2+(k_LL)^2)\approx 1$ and $\langle\omega_{pi}^2\rangle/\omega_{ci0}^2\gg 1$. For the same reason, the ω' term is dropped, so that we have

$$\omega'^2+\frac{m^2}{m_\perp^2}\Gamma_r^2=0, \qquad (6.62)$$

which again recovers the MHD limit, $s^{-1}\propto\partial N_0/\partial\psi>0$ for centrifugal drives and $\partial N_0/\partial\psi<0$ for gravitational drives.

Furthermore, the rotational interchange mode has frequency $\omega=m\Omega+\imath\gamma$, where the growth rate is,

$$\gamma=\pm\sqrt{\frac{m^2}{m_\perp^2}\Gamma_r^2}, \qquad (6.63)$$

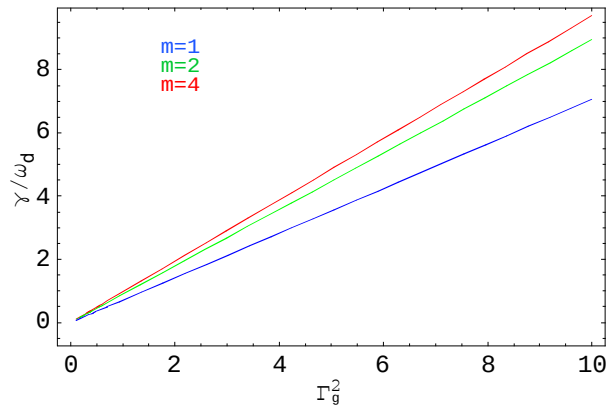

Figure 6.1: The growth rate of the rotationally driven interchange mode versus the rotational drive.

ie., it is proportional to the background density scale length - as in the classical Rayleigh Taylor instability - as well as the rotation frequency, as expected. Furthermore, we see that high m modes as well as longest wavelength modes are most unstable. This can be seen explicitly in Figure 6.1 In the $\mathbf{E} \times \mathbf{B}$ frame of reference, the modes are stationary, purely exponentially growing modes, which is consistent with the observations that the modes propagate in the $\mathbf{E} \times \mathbf{B}$ frame.

The fact that high m modes are most unstable is at odds with experiment. To more closely approximate the experiment we add the dispersive effects of the drift-resonant hot electrons, which add a small real frequency to the solutions.

6.3 Hot Electron Interchange Dispersion Relation

We may employ the same nonlinear two fluid approach to derive the dispersion relation for the HEI instability. The method is identical concerning the fluid description of the cold ions and electrons, however, for the hot electron population necessary to drive the pressure driven HEI mode, a kinetic approach is required [44].

6.3.1 Hot Electron Dynamics

The hot electrons are modeled as an anisotropic ($p_\perp \gg p_\parallel$) equatorially trapped population localized at the microwave cyclotron resonance location. The cold electrons, in contrast, are more uniformly distributed. Thus the hot electrons form a disk within the colder background plasma. The guiding center Hamiltonian describes nonrelativistic energetic electrons interacting with drift-resonant electrostatic waves:

$$H = \frac{\mu}{e}B - \Phi. \tag{6.64}$$

Since the hot electrons are deeply trapped, we look only at dynamics in the equatorial plane, setting $J = 0$. Thus the equations of motion are only two-dimensional, in the (ψ, φ) plane, and are quite simple:

$$\dot{\varphi} = \frac{\partial H}{\partial \psi} = \frac{\mu}{e}\frac{\partial B}{\partial \psi} - \frac{\partial \Phi}{\partial \psi} = \omega_d(\mu) - \frac{\partial \Phi}{\partial \psi} \tag{6.65}$$

$$\dot{\psi} = -\frac{\partial H}{\partial \varphi} = \frac{\partial \Phi}{\partial \varphi}, \tag{6.66}$$

where we've defined the magnetic precessional drift frequency for the hot electrons, $\omega_d = 3\mu B/e\psi$.

To describe a distribution of electron energies confined to the equatorial plane, the Vlasov equation is employed, with a distribution function, $F(\mu, \psi, \varphi, t)$,

$$\frac{dF}{dt} + \frac{\partial}{\partial \varphi}(\dot{\varphi}F) + \frac{\partial}{\partial \psi}(\dot{\psi}F) = 0. \tag{6.67}$$

The flux tube integrated electron number is just $N_e = \int d\mu dJ F$. To make further progress we assume that F is separable, defining $\alpha(\psi)$ to be the energetic electron fractional density. Thus, the background distribution function is simply,

$$F_0 = N_{i0}(\psi)[1 - \alpha(\psi)]\delta(\mu)\delta(J) + N_{i0}(\psi)\alpha(\psi)G(\mu)\delta(J), \tag{6.68}$$

where $G(\mu)$ is the distribution of electron energies, given as

$$G(\mu) = \frac{\mu^{l-1}l^l}{\mu_0^l \Gamma(l)} \exp(-\mu l/\mu_0), \tag{6.69}$$

where l is a positive integer. $G(\mu)$ becomes a delta function for $l \to \infty$ and a gaussian at $l = 0$. For any integer value of l, $\int d\mu \mu G = \mu_0$.

Using the same linearization scheme as before, Equation 6.40, and noting that

$$\tilde{F} = \frac{m}{\omega - m\omega_d}\Phi_m F_0, \tag{6.70}$$

we find the perturbed electron number density,

$$\tilde{N}_e = \int d\mu dJ \tilde{F} = \frac{m}{\omega}\Phi_m \frac{\partial N_{i0}}{\partial \psi} + m^2 \Phi_m \frac{\partial (N_{i0}\alpha)}{\partial \psi} \int d\mu \frac{\omega_d G(\mu)}{\omega(\omega - m\omega_d)}. \tag{6.71}$$

The first term on the right hand side is the same background density gradient term we found for the cold electrons in Equation 6.43, except that it is in the ω' frame. The second term is the hot electron interchange drive term, exhibiting the drift-wave resonance in the denominator.

6.3.2 Dispersion Relation

Again we solve Poisson's equation, Equation 6.54, with the electron density number given by Equation 6.71 and the ions given by

$$\tilde{N}_i = \frac{m}{\omega}\Phi_m \frac{\partial N_{i0}}{\partial \psi} + \omega N_{i0} \frac{M^2 B_0}{\omega_{ci0}\psi^2}\left(0.77\frac{\partial^2 \tilde{\Phi}}{\partial \psi^2} - 0.66\frac{m^2}{\psi^2}\Phi_m\right), \tag{6.72}$$

which is identical to Equation 6.47 save the centrifugal and gravitational terms and is also in the ω' reference frame.

Solving Poisson's equation, we find the following dispersion relation in the high density limit $\langle \omega_{pi}^2 \rangle / \omega_{ci0}^2 \gg 1$:

$$D(\omega, m, m_\perp) \approx 1 + 1.5\frac{m^2}{m_\perp^2}\frac{\psi}{N}\frac{\partial (N_{i0}\alpha)}{\partial \psi} \int d\mu \frac{\omega_{ci}\omega_d G(\mu)}{\omega(\omega - m\omega_d)}. \tag{6.73}$$

To find the roots of this singular dispersion function, the usual Landau prescription for wave-particle resonant interactions is employed. It is convenient to express D in terms of exponential integrals. The dispersion relation for a mono-energetic electron distribution, $G(\mu) = \delta(\mu - \mu_0)$, becomes,

$$D_0(\omega, m, m_\perp) \approx 1 + \frac{m^2}{m_\perp^2}\frac{\Gamma_h^2}{\omega(\omega - m\omega_{d0})}, \tag{6.74}$$

where the hot electron interchange drive is defined as,

$$\Gamma_h^2 = 1.5\omega_{ci}^* \omega_{d0}\frac{\psi^*}{N_0}\frac{\partial (N_{i0}\alpha)}{\partial \psi}, \tag{6.75}$$

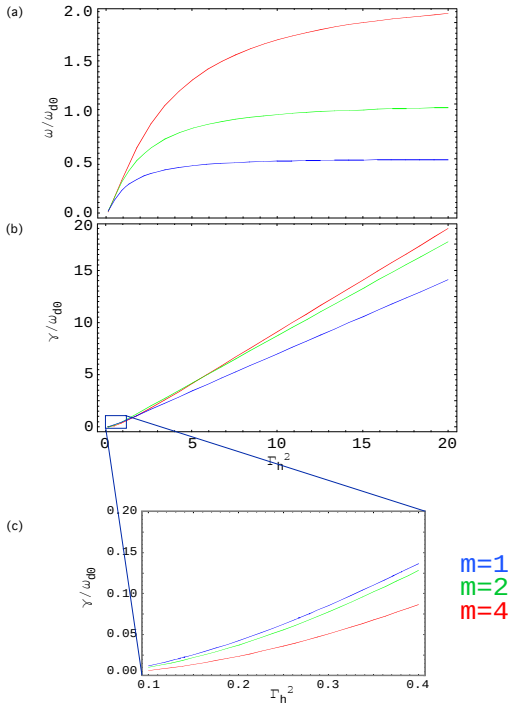

Figure 6.2: a) HEI frequency, b) HEI growth rate, and c) HEI growth rate in low drive regime, where low m modes are seen to be more unstable.

and ω_{d0} is the drift frequency at B_0. For the mono-energetic dispersion relation, instability results when $\Gamma_h^2 > m_\perp^2 \omega_{d0}^2$ with a real frequency given by $m\omega_{d0}/2$. Low m number modes are most unstable as well as broad radial modes, $m_\perp^2 \ll 1$.

A distribution in electron energy extends the instability regime below the mono-energetic stability limit. Plots of HEI instability real frequency and growth rate versus the HEI drive are shown in Figure 6.2. In Figure 6.2(a) the real frequencies are plotted and it can be seen that as $\Gamma_h \to \infty$, $\omega \to m\omega_{d0}/2$, the classical value. In (b) and (c) it is shown that for high values of HEI drive, higher m modes become more unstable, while at lower drive it is lower m numbers that are more unstable. It is this low drive regime, $\Gamma_h^2 \leq 1$, in which the CTX experiment operates, where low m modes are usually observed to be more unstable than higher ones. However, in extremely energetic HEI bursts, higher m modes have been observed to be most unstable.

6.4 Combined Interchange Dispersion Relation

Having derived the dispersion properties of both the rotationally driven and the pressure driven (HEI) interchange instabilities, it is a straight forward matter to combine the two into a complete interchange description. The full interchange dispersion relationship, from Equations 6.62 and 6.73, is given by,

$$D_{tot}(\omega, m, m_\perp) \approx 1 + \frac{m^2}{m_\perp^2}\left[\frac{\Gamma_r^2}{\omega^2} + \frac{\Gamma_h^2}{\omega}\int d\mu \frac{G(\mu)\mu/\mu_0}{(\omega - m\omega_d)}\right]. \tag{6.76}$$

This equation has three roots in genenal; a stable oscillatory root, an unstable root and a decaying root.

In the case where both drives are present there must be some modification of the mode structure since HEI modes have low m modes be unstable (when the drive is low, as in the experiment) while rotational modes of higher m's be more unstable at all values of Γ_r^2. It is natural to expect that for the properly chosen values of Γ_h and Γ_r, a low frequency mode with nonzero rotational drive will result with low m numbers being most unstable. Indeed, such is the case in the following plot, Figure 6.3, where the combined interchange growth rate is shown versus HEI drive while the rotational drive is held constant at $\Gamma_r^2 = 0.2$. In the low HEI drive regime that is plotted, low m modes do indeed become more unstable. However, since as $\Gamma_h \to 0$ higher m's must become more unstable, in accordance with the rotational dispersion relation, we see at even lower values of Γ_h that the growth rates for higher m's do again become more unstable. The $m = 4$ mode due to just HEI drive is also plotted and shows that for low Γ_h where the HEI growth goes to zero, there is a finite growth rate for the combined modes; this is the purely growing rotational mode. Thus, we can conclude that the experimental observations exist within this range where neither the rotational nor HEI drives are robustly dominant.

Of course, the observations are of a dynamical system near marginal stability in a non-linearly saturated state, while this is simply a linear theory. The nonlinear simulation, for example, exhibits a linear growth phase initially but always appears to nonlinearly saturate to an $m = 1$ mode. So various dissipative effects not included in Equation 6.76 that can also stabilize higher m modes may be important here.

Having said that, this theory offers a possible explanation for the two observed regimes

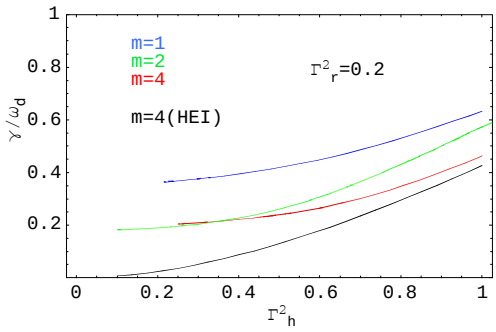

Figure 6.3: The growth rate of the combined interchange mode versus the HEI drive, for $m = 1, 2, 4$. $m = 1$ has the largest growth rate, but as $\Gamma_h \to 0$ higher modes become more unstable again. The solutions begin to break down in this singular limit. The black line is just the HEI solution for $m = 4$ for the sake of comparison.

of the rotational mode. When the HEI drive is stronger relatively to the rotational drive, dominant $m = 1$ potential structures are measured. If the HEI drive is reduced and rotational drive increased by lowering the magnetic field which simultaneously reduces the population of hot electrons and increases the $\mathbf{E} \times \mathbf{B}$ frequency, a dominant $m = 2$ structure is measured.

6.5 Summary

In this Chapter the linear dispersion relations for both rotationally driven and pressure driven interchanges was derived using a two fluid method. It is found that finite temperature effects are necessary to reproduce the experimental observations and numerical simulation results of the rotationally driven instability, specifically the fact that low m number modes are most unstable. The real frequency imparted to the solutions by the HEI drive allows polarization effects to stabilize higher m modes preferentially. This offers an explanation for the key observation of a dominant $m = 2$ mode when the rotational drive is increased by lowering the magnetic field.

The agreement between experimental observation, numerical simulation and the linear stability analysis leads us to identify the observed fluctuations as the rotationally driven interchange instability.

Chapter 7

Conclusions

This thesis reports the first study of the global mode structures of interchange instabilities observed in a laboratory magnetic dipole. Instabilities driven by pressure forces due to an energetic, drift-resonant hot electron population as well as rotation driven interchanges induced by $\mathbf{E} \times \mathbf{B}$ rotation are observed.

Low frequency, drift-resonant, electrostatic interchange instabilities are driven by a hot electron population in the CTX device. The mode structure is measured using a multi-probe cross-correlation analysis. These modes have a a complex time-varying frequency spectrum, but are characterized by a relatively simple mode structure which is characterized by low m numbers and broad radial structure. There is no structure along a field-line, consistent with interchange physics. The form of the mode structure does not evolve significantly in time. A self-consistent nonlinear numerical simulation reproduces many key aspects of the global mode structure, including the broad radial mode structure of the lowest m number modes.

An external biasing array was constructed and mounted on the terrella of CTX in order to induce radial electric fields to azimuthally $\mathbf{E} \times \mathbf{B}$ spin the plasma. Upon application of the external bias, large electric fields, rapid plasma rotation and a flattening of the inner plasma density are measured. We observe low frequency global flute modes and identify them as the rotationally driven interchange instability. The mode is observed to propagate in the $\mathbf{E} \times \mathbf{B}$ frame of reference. Global mode analyses indicate broad radial mode structures and low order azimuthal modes, similar to those of the HEI, though there is a large nonzero radial phase, $k_r \neq 0$, distinct from HEI.

The nonlinear simulation was adapted to observe the rotational mode by adding bulk rigid rotation. It reproduces the observed instability after appropriate selection of ion and electron profiles, as well as rotation frequencies. Since the nonlinear simulation evolves the instability from an initial value, the time-evolution of the rotational mode could not be easily compared to experiment. Nevertheless, when sufficient dissipation was added that damped short wavelengths, the longer-wavelength $m = 1$ mode was dominant during both the linear and the nonlinear stages of the simulated interchange event. We find the nonlinear mode structure computed with the simulation to be comparable to the mode structure observed in the experiment. For high rotation frequencies and steep density gradients, higher m modes are seen to be more unstable, which is corroborated experimentally: when the magnetic field is lowered so as to increase the $\mathbf{E} \times \mathbf{B}$ frequency an $m = 2$ potential structure becomes dominant over the $m = 1$ structure. However, in the simulation higher m structures are seen in the linear growth phase but usually relax back to an $m = 1$ mode as the instability nonlinearly saturates. In contrast, the appearance of the $m = 2$ mode experimentally is already in the saturated phase. This behavior has not yet been reproduced computationally, and it suggests that the dissipative processes at work in the experiment may not be fully understood or modeled correctly. With this exception, the numerical simulation is successful at recovering many of the global characteristics of both the HEI and rotational instabilities. The comparison of the linear and saturated states in the simulation and the experiment is an area which merits further investigation. To that end, the observation of the linear stage of the rotational mode would be critical.

The local linear dispersion analysis for interchange instabilities driven by both pressure and rotation drives has also been solved. Short wavelengths are driven unstable by the purely rotational drive, while the HEI drive can excite different wavelength modes depending on the magnitude of the drive: for low drives, long wavelength modes are unstable. This is the regime that is observed in all of the HEI and rotational mode studies. It is shown that finite temperature effects add a real frequency to the modes which induce stabilizing polarization currents which tend to stabilize high m modes. Thus, the full interchange dispersion relation with both pressure and rotational drives captures important elements of how the observed mode structure depends on the relative magnitude of the instability drives.

The work described in this thesis raises interesting questions for plasma science in two

particular areas. First, the understanding of pressure driven interchanges is critical for the prospect of achieving controlled fusion in a dipole confined plasma. It is clear that having the capability of controlling the pressure profile is necessary to ensure interchange stability.

Secondly, do these experiments have any bearing on the magnetospheric interchange instability? Many theories of these modes, as well as the data collected during the Galilean encounter with the Io torus suggest that magnetospheric interchange instabilities might have small wavelengths. Some estimates put the azimuthal extent of a magnetospheric interchange perturbation at 15°. However, the rotationally driven modes described here have longer wavelength. In the Io torus the cold plasma density gradient is unstable while the energetic pressure gradient is stable. In CTX both are unstable, so that both pressure and rotationally driven modes are observed simultaneously. However, energetic particles do play important roles in both situations, and it is possible that low m modes could exist in rapidly rotating magnetospheres. If such large wavelength modes did exist, Galileo might not have observed them, since the rotation speed of such a large structure would be much slower than the transit time of the space-craft through it. It is also possible that the interchange of dense plasma would be a much slower diffusive process if the mode structure were global, instead of the rapid interchange of plasma confined by small flux-tubes. Other space-craft, including the upcoming Cassini-Huygens mission to the Saturnian magnetosphere, may observe further evidence of rotational interchange phenomena which may shed some light on some of these issues.

Interesting opportunities remain for experimental research relating to the newly discovered instability. The biasing array has capability of application of up to $m = 3$ potentials on the inner boundary of the plasma. Driven plasma convection, non-axisymmertic circulation, and (possibly) interchange stabilization by synchronous application of rotating biased potentials can be studied in a controlled way in the laboratory with this new instrument. Much of the theory for these experiments has already been presented in this thesis. Furthermore the polar imaging diagnostic has not been used to its full potential. The diagnostic enables spatial and temporal imaging of the entire plasma (bounce-averaged) phase-space. Time-dependent and global pictures of plasma and phase-space can be measured. Data from the array can be used to generate high-speed, image-maps of field-line integrated particle density during strong flows induced by intense low-frequency instabilities, and would add

immensely to the detailed understanding of the complex instabilities discussed here.

Bibliography

[1] J. M. Albert, *J. Geophys. Res*, **105**, 21191 (2000).

[2] W. B. Ard, R. A. Dandl, and R. F. Stetson, *Phys. Fluids* **8**, 1498 (1966).

[3] H. L. Berk, *Phys. Fluids*, **19**, 1255 (1976).

[4] H. L. Berk, B. N. Breizman, J. Candy, M. Pekker, and N. V. Petviashvili, *Phys. Plasmas* **6**, 3102 (1999).

[5] I. B. Bernstein, E. A. Frieman, M. D. Kruskal, and R. M. Kulsrud, *Proc. Roy. Soc. A* **244**, 17 (1958).

[6] S. Chandrasekar, *Plasma Physics* (University of Chicago Press, Chicago, IL, 1960), pp. 80-96.

[7] A. F. Cheng, *J. Geophys. Res*, **90**, 9900 (1985).

[8] R. N. Czerwinski, *Adaptive time-frequency analysis using a cone-shaped kernel*, Master's thesis, University of Illinois Urbana-Champaign (1993).

[9] L. Cohen, *Time-Frequency Analysis* (Prentice Hall, 1995).

[10] A. J. Dragt, *Rev. Geophys.*, **3**, 255, (1965).

[11] T. H. Dupree, *Phys. Fluids*, **15**, 334 (1972).

[12] C.-G. Fälthammar, *J. Geophys. Res.* **70**, 2503 (1965).

[13] K. M. Ferriere and M. Blanc, *J. Geophys. Res*, **101**, 19,871 (1996).

[14] K. M. Ferriere, C. Zimmer and M. Blanc, *J. Geophys. Res*, **104**, 17,335 (1999).

[15] K. M. Ferriere, C. Zimmer and M. Blanc, *J. Geophys. Res*, **106**, 327 (2001).

[16] J. R. Ferron, A. Y. Wong, G. Dimonte, and B. J. Leikind, *Phys. Fluids* **26**, 2227 (1983).

[17] L. A. Frank and W. R. Paterson, *J. Geophys. Res.* **106**, 6131 (2001).

[18] R. Freeman, M. Okabayashi, G. Pacher, *et al.*, "Confinement of plasmas in the spherator," in *Plasma Phys. and Contrl. Nuc. Fusion*, Vol. 1, pp. 27-57, IAEA, Vienna (1971).

[19] M. J. Gerver and B. G. Lane, *Phys. Fluids*, **29** (7), 2214 (1986).

[20] T. Gold, *J. Geophys. Res*, **64**, 1219 (1959).

[21] R. J. Goldston and P. H. Rutherford, *Plasma Physics* (Institute of Physics Publishing, Philadelphia, PA, 1995).

[22] J. P. Gunn, *et al.*, *Phys. Plasmas* **8**, 5, 1995 (2001).

[23] P. N. Guzdar, J. F. Drake, D. McCarthy, *et al.*, *Phys. Fluids B* **5**, 3712 (1993).

[24] C. W. Hartman, *Phys. Fluids* **9**, 821 (1966).

[25] S. Hiroe, J. B. Wilgen, F. W. Baity, *et al.*, *Phys. Fluids* **27**, 1019 (1984).

[26] I. H. Hutchinson, *Principles of Plasma Diagnostics*, (Cambridge University Press, 2000).

[27] I. H. Hutchinson, *Phys. Fluids*, **30**, 3777 (1987).

[28] Yu V. Gott, M. S. Ioffe, V. G. Tel'kovskii, *Nuc. Fusion*, 1962 Suppl., Part 3, p. 1045 (1962). See also M. S. Ioffe, "Mirror Traps", pp. 421-448, in *Plasma Physics*, IAEA, Vienna (1965).

[29] J. D. Jackson, *Classical Electrodynamics* (John Wiley & Sons, third edition, 1999).

[30] M. C. Kelly, *The Earth's Ionosphere* (Academic Press, San Diego, CA, 1989), pp. 113-185.

[31] J. Kesner, *Phys. Plasmas*, **4**, 419 (1998).

[32] M.G. Kivelson, K. K. Khurana, R. J. Walker, J. Warnecke, C. T. Russell, J. A. Linker, D. J. Southwood, and C. Polanskey, *Science*, **274**, 396 (1996).

[33] M. G. Kivelson, K. K. Khurana, C. T. Russell, and R. J. Walker, *Geophys. Res. Lett.* **24**, 389 (1997).

[34] N. A. Krall, *Phys. Fluids* **9**, 820 (1966).

[35] D. E. Lencioni, J. W. Poukey, J. A. Schmidt, J. C. Sprott, and C. W. Erickson, *Phys. Fluids* **11**, 1115 (1968).

[36] B. Levitt, D. Maslovsky, M. Mauel, *Phys. Plasmas*, **9**, (2002).

[37] A. J. Lichtenberg, and H. Meuth, *Phys. Fluids*, **29**, 3511 (1986).

[38] W. W. Liu *J. Geophys. Res*, **101**, 27,443 (1996).

[39] C. L. Longmire and M. N. Rosenbluth, *Annals of Physics* **1**, 120 (1957).

[40] D. Maslovsky, B. Levitt, and M. E. Mauel, *Phys. Rev. Lett.*, **10**, (2003).

[41] D. Maslovsky, B. Levitt, and M. E. Mauel, *Phys. Plasmas*, **10**, (2003).

[42] D. Maslovsky, M. Mauel, and B. Levitt, *IEEE Trans. Plasma Sci.*, **30**, (2002).

[43] D. A. Maslovsky, *Suppression of Nonlinear Frequency Sweeping of Resonant Interchange Modes in a Magnetic Dipole with Applied Radio Frequency Fields*, Ph. D. thesis, Columbia University (2003).

[44] M. E. Mauel, *J. Phys. IV France*, **7** 307 (1997).

[45] M. E. Mauel, *Phys. Fluids*, **27**, (1984).

[46] B.H. Mauk, D. J. Williams, and R. W. McEntire, *Geo. Phys. Lett.*, **24**, 2949 (1997).

[47] C. E. McIlwain, *J. Geophys. Res.*, **66**, 3681 (1961).

[48] S. Murakami, T. Sato, and A. Hasegawa, *Phys. Fluids B*, **2**, 715 (1990).

[49] G. A. Navratil, R. S. Post, and A. Butcher Ehrhardt, *Phys. Fluids* **20**, 156 (1977).

[50] W. A. Newcomb, *Phys. Fluids*, **4**, 391 (1961).

[51] T. G. Northrop and E. Teller, *Phys. Rev.*, **117**, 215 (1960).

[52] F. J. Øynes, H. L. Pécseli, and K. Rypdal, *Phys. Rev. Lett.* **75**, 81 (1995).

[53] G. K. Parks, *Physics of Space Plasmas* (Addison-Wesley, Redwood City, CA, 1991).

[54] C. Riccardi and A. Fredriksen, *Phys. Plasmas* **8**, 199 (2001).

[55] B. Rogers and B.U.O. Sonnerup, *J. Geophys. Res*, **91**, 8837 (1986).

[56] B. Rogers and B.U.O. Sonnerup, *J. Geophys. Res*, **68**, 131 (1963).

[57] C.T. Russell, M. G. Kivelson, K. K. Khurana, and D. E. Huddleston, *Planet. Space Sci.*, **47**, 644 (1999).

[58] K. Rypdal, O. E. Garcia, and J.-V. Paulsen, *Phys. Rev. Lett.* **79** 1857 (1997).

[59] M. Schulz and L.J.Lanzerotti, *Particle Diffusion in the Radiation Belts* (Springer-Verlag, New York, NY, 1974).

[60] V. D. Shafranov, *Nuc. Fusion* **28**, 253 (1968).

[61] G. L. Siscoe, A. Eviatar, R. M. Thorne, and J. D. Richardson, *J. Geophys. Res.* **86**, 8480 (1981).

[62] D. J. Southwood and M. G. Kivelson, *J. Geophys. Res.*, **92**, 109 (1987).

[63] D. J. Southwood and M. G. Kivelson, *J. Geophys. Res.* **94**, 299 (1989).

[64] D. A. Spong, H. L. Berk, and J. W. Van Dam, *Phys. Fluids* **27**, 2292 (1984).

[65] R. M. Thorne, T. P. Armstrong, S. Stone, *et al.*, *Geophys. Res. Lett.* **24**, 2131 (1997).

[66] J. A. Van Allen, G. H. Ludwig, E. C. Ray, C. E. McIlwain, *Jet Propulsion*, **28**, 588 (1958).

[67] H. Vernon Wong, H. L. Berk *Phys. Lett. A*, **251**, 126 (1999).

[68] H. P. Warren and M. E. Mauel, *Phys. Rev. Lett.*, **74**, 1351 (1995).

[69] H. P. Warren and M. E. Mauel, *Phys. Plasmas*, **2**, 4185 (1995).

[70] H. P. Warren, M. E. Mauel, D. Brennan, and S. Taromina, *Phys. Plasmas*, **3**, 2143 (1996).

[71] H. P. Warren, *Observation of Chaotic Particle Transport Driven by Drift-Resonant Fluctuations in the Collisionless Terrella Experiment*, Ph. D. thesis, Columbia University (1994).

[72] H. P. Warren, A. Bhattachargee, and M. E. Mauel, *Geophys. Res. Lett.*, **19**, 941 (1992).

[73] J. C. Yang, S. H. Seo, G. C. Kwon, et al., *Phys. Letters A*, **185**, 428 (1994).

[74] S. T. Zalesak and S. L. Ossakow, *J. Geophys. Res.* **85**, 2131 (1980).

[75] S. T. Zalesak, *J. Comput. Physics* **31**, 335 (1979).

[76] S. T. Zalesak, *J. Comput. Physics* **40**, 497 (1981).